ORNL/TM-2015/366

Crash Models for Advanced Automotive Batteries

A Review of the Current State of the Art and Report on Department of Energy Project 2088-V805-14 for the National Highway Traffic Safety Administration (NHTSA), an Office of the U.S. Dept. of Transportation

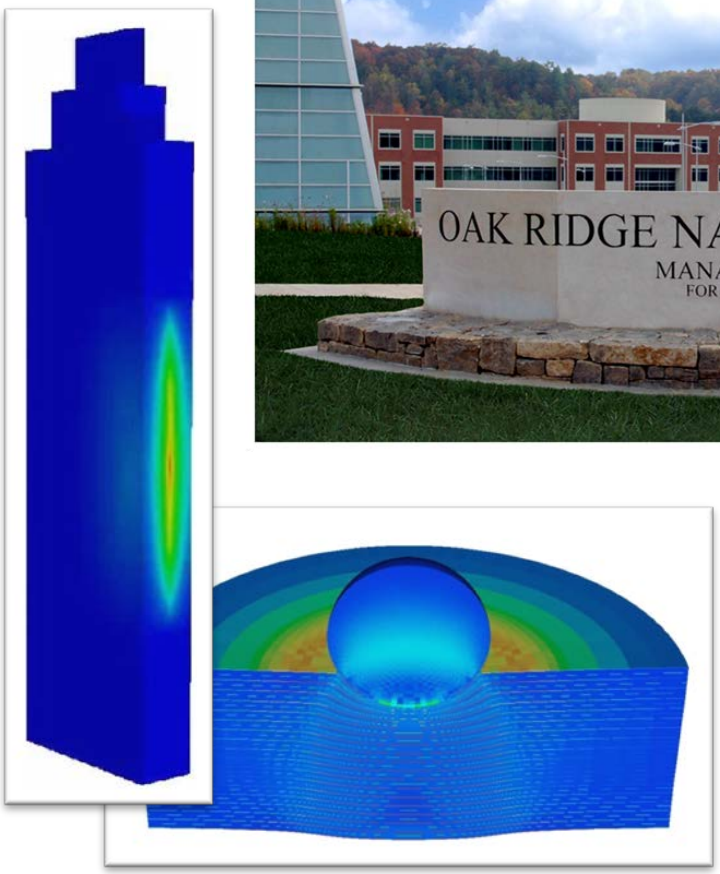

John A. Turner (PI)
Srikanth Allu
Sarma Gorti
Sergiy Kalnaus
Abhishek Kumar
Damien Lebrun-Grandie
Sreekanth Pannala
Srdjan Simunovic
Stuart Slattery
Hsin Wang

Feb. 2015

OAK RIDGE NATIONAL LABORATORY
MANAGED BY UT-BATTELLE FOR THE US DEPARTMENT OF ENERGY

ORNL/TM-2015/366

Computer Science and Mathematics Division (CSMD)
Materials Science and Technology Division (MSTD)

Crash Models for Advanced Automotive Batteries

A Review of the Current State of the Art

and

Report on Dept. of Energy Proposal 2088-V805-14

for the

National Highway Traffic Safety Administration (NHTSA)

an Office of the

U.S. Department of Transportation (DOT)

John A. Turner (PI)
Srikanth Allu
Sarma Gorti
Sergiy Kalnaus
Abhishek Kumar
Damien Lebrun-Grandie
Sreekanth Pannala
Srdjan Simunovic
Stuart Slattery
Hsin Wang

Date Published:
February 2015

Prepared by
OAK RIDGE NATIONAL LABORATORY
Oak Ridge, TN 37831-6283
managed by
UT-BATTELLE, LLC
for the
US DEPARTMENT OF ENERGY
under contract DE-AC05-00OR22725

CRASH MODELS FOR ADVANCED AUTOMOTIVE BATTERIES

A REVIEW OF THE CURRENT STATE OF THE ART AND REPORT ON DEPARTMENT OF ENERGY (DOE) PROPOSAL NUMBER 2088-V805-14 FOR THE NATIONAL HIGHWAY TRAFFIC SAFETY ADMINISTRATION (NHTSA), AN OFFICE OF THE U.S. DEPARTMENT OF TRANSPORTATION (DOT).

EXECUTIVE SUMMARY

Safety is a critical aspect of lithium-ion (Li-ion) battery design. Impact/crash conditions can trigger a complex interplay of mechanical contact, heat generation and electrical discharge, which can result in adverse thermal events. The cause of these thermal events has been linked to internal contact between the opposite electrodes, i.e. internal short circuit. The severity of the outcome is influenced by the configuration of the internal short circuit and the battery state. Different loading conditions and battery states may lead to micro (soft) shorts where material burnout due to generated heat eliminates contact between the electrodes, or persistent (hard) shorts which can lead to more significant thermal events and potentially damage the entire battery system and beyond. Experimental characterization of individual battery components for the onset of internal shorts is limited, since it is impractical to canvas all possible variations in battery state of charge, operating conditions, and impact loading in a timely manner.

This report provides a survey of modeling and simulation approaches and documents a project initiated and funded by DOT/NHTSA to improve modeling and simulation capabilities in order to design tests that provide leading indicators of failure in batteries.

In this project, ORNL has demonstrated a computational infrastructure to conduct impact simulations of Li-ion batteries using models that resolve internal structures and electro-thermo-chemical and mechanical conditions. Initial comparisons to abuse experiments on cells and cell strings conducted at ORNL and Naval Surface Warfare Center (NSWC) at Carderock MD for parameter estimation and model validation have been performed. This research has provided insight into the mechanisms of deformation in batteries (both at cell and electrode level) and their relationship to the safety of batteries.

CONTENTS

FIGURES

TABLES

1. INTRODUCTION

Background: Lithium-ion batteries are currently used for the new generation of electric vehicles (EVs) due to their high cell voltage and energy density, wide operating temperature range, fast charging rate, and absence of memory-effect [1]. In the historical design process of EVs, the toughest technological challenges are to provide sufficient energy and power [2], [3]. Crash performance of EVs has recently begun to attract the attention of the media and public. The full-scale tests of electrified vehicles [3], [4] have yielded a wide range of accelerations and impulses based on the test conditions. In order to maximize the operating range of EVs, designers must also utilize new lightweight materials as much as possible. These materials are less forgiving in crash situations compared to conventional carbon steels, thereby compounding the design challenge. Industry standards [5], [6] and federal safety regulations [7] have been developed to address some EV-specific safety issues (electrolyte spillage, battery retention, and electrical isolation of the chassis from the high voltage system). The objective of the research described in this report is to develop testing configurations and simulation methods for assessment of battery response under different mechanical loading conditions, with emphasis on impact/crash conditions. The expected outcomes of the proposed research are formulations for coupled physics simulation, along with suitable material and structural models for typical battery cells that would eventually be transferable to vehicle crash simulations.

Current State-of-the-Art: Aside from generally central location in vehicles, the primary protection to the EV's battery integrity is its casing. Current battery crash models approximate the battery interior with an equivalent isothermal homogenized medium that is loaded by the casing [8]. This approach is a useful approximation for investigation of casing's integrity, but ignores the battery's interior state, and thus is incapable of accurately modeling the likelihood and severity of battery thermal events. Recently, detailed dry cell loading simulations of Li-ion cells with a focus on development of mechanically representative volume elements and their correlations to the experimental data have been conducted [9], [10]. However, neither steady-state nor time-dependent simulations of mechanical impact coupled with thermo-electro-chemistry have yet been reported. Additionally, the strain rate of an automotive crash is orders of magnitude higher than the mechanical experiments that have been reported in the public domain, which may require modifications to material models or physics coupling methodology. A detailed, coupled mechanics-electrochemical-thermal model of Li-ion battery systems is needed to complement the experiments, compensate for practical testing limitations, and help to develop tests for assessment of EV battery safety.

Impact of the Current Research: This computational and experimental research study simulates battery's electrochemical, thermal, and structural responses under mechanical impact conditions. Capturing the failure characteristic features required micrometer resolution for typical cell components, which span centimeters. Under the DOE/EERE Computer Aided Engineering for Batteries (CAEBAT) project [11], [12], ORNL has developed the Virtual Integrated Battery Environment (VIBE), a software environment for time-dependent coupled physics simulation of batteries, with emphasis on Li-ion. VIBE was extended to couple impact mechanics and its interaction with other physics components. The models were used to analyze and to correlate with the existing mechanical test data from ORNL [13] with the input of Ford Motor Company. New cell or cell-stack level tests were conducted by ORNL to support model development and validation.

As part of this project, ORNL has developed models for representative pouch automotive batteries that combine mechanical, electrical, electrochemical, and thermal responses under deformation due to mechanical abuse. The models are based on finite element method (FEM) formulations of the underlying transport and on conservation equations. To accurately model the critical area of a short

circuit, a parallel, domain decomposition solution methodology has been applied to solve these systems by exploiting the hierarchical nature of battery systems.

The electrochemical-electrical-thermal simulations have been compared to ongoing experiments under this project, the CAEBAT program as well as DOE Advanced Research Projects Agency-Energy (ARPA-E) projects at ORNL. In addition, this project leverages ongoing efforts at ORNL developing the necessary electrochemical models including side reactions to predict the voltage/current profile of a short-circuit without any external inputs such as short resistance. With these developments and further validation through both the static and dynamic versions of the pinch test, we are developing fully validated and coupled simulations that model the electrochemical-electrical-thermomechanics response of a pouch cell under mechanical abuse. These models themselves are extensible to other configurations such as prismatic as well as cylindrical cells.

In addition to correlating the developed models with previous ORNL cell level testing, new high impact cell or cell-stack level testing has been performed. Design and setup of these experiments has been guided by the likely vehicle conditions cells would encounter.

In the following sections, we provide a review of the state-of-the-art in modeling the performance of LIBs, under both normal conditions as well as under abuse scenarios. Subsequent to that we summarize the progress made towards developing predictive models for simulating batteries under crash conditions along with a description of experiments to validate the results. Finally, we provide next steps to further improve the understanding of the fundamental processes governing thermal runaway and how to efficiently scale the simulations to full pack without loss of predictability.

2. MODELING OF NORMAL CHARGE/DISCHARGE CYCLES

This section is devoted to a review of mathematical models available for description of different physics involved in normal operation of redox systems. The normal operation implies absence of external mechanical loads leading to dimensional changes within the cell, severe concentration gradients accompanied by irreversible phase transformations (i.e. overcharge and overdischarge), and absence of thermal extremes that may occur under thermal abuse or short circuit. Under the normal galvanostatic charge and discharge cycling within the safe predefined state of charge (SOC) window, the electrochemical cell experiences insertion/extraction of Li ions into/from the host electrode structure - the rate of this process is dictated by local electrochemical overpotentials and electronic and ionic diffusivities. Structural changes (strains) associated with this process are typically ignored on the macroscopic cell level, while local crystal lattice distortions can be quite severe. Any departure from the equilibrium, which in electrochemical systems is characterized by the open circuit potential (OCP), drives the reaction in one preferential direction (oxidation or reduction) and thus involves heat generation. Therefore the electrochemical models have to be coupled to thermal transport. Three physics processes can generally describe the normal near-equilibrium operation of an electrochemical cell:

- Diffusion and electrochemical reactions at the interface
- Conservation of charge
- Thermal energy transport

In what follows we discuss available models for the above physics.

2.1 ELECTROCHEMICAL MODELS

Generally, the processes responsible for conversion of chemical energy to electrical current and vice versa can be described by a set of four differential equations covering mass and charge conservation [14], [15], [16]:

$$\begin{cases} \dfrac{\partial(\varepsilon_e c_e)}{\partial t} = \nabla\cdot\left(D_e^{eff}\nabla c_e\right) + \dfrac{1-t_+^0}{F} j^{Li} \\ \dfrac{\partial(\varepsilon_s c_s)}{\partial t} = \nabla\cdot\left(D_s^{eff}\nabla c_s\right) - \dfrac{j^{Li}}{F} \end{cases} \quad \text{..... (1)}$$

$$\begin{cases} \nabla\cdot\left(\kappa^{eff}\nabla\varphi_e\right) + \nabla\cdot\left(\kappa_D^{eff}\nabla\ln(c_e)\right) = -j^{Li} \\ \nabla\cdot\left(\sigma^{eff}\nabla\varphi_s\right) = j^{Li} \end{cases} \quad \text{..... (2)}$$

where c_s, c_e, and φ_s, φ_e are the concentrations and potentials in the solid and electrolyte phases (subscripts *s* and *e* respectively), t_+^0 is the transference number of cations in electrolyte and *F* is the Faraday constant. The source terms in Eq (1) are represented by the flux of Li ions that is ultimately responsible for balance between ionic and electronic currents. The flux of ionic charge carriers, j^{Li}, occurs in the preferential direction and is driven by prevalence of cathodic or anodic reaction at the interface. This process is described by the Butler-Volmer equation.

$$j^{Li} = \frac{i_0}{F}\left[exp\left(\frac{\alpha_a F}{RT}\eta\right) - exp\left(-\frac{\alpha_c F}{RT}\eta\right)\right] \quad \text{..... (3)}$$

in which the half-cell overpotential is $\eta = \varphi_s - \varphi_e - U$ and *U* is the corresponding open circuit potential. The exchange current density is driven by changes in lithium concentration

$$i_0 = k{c_e}^{\alpha_a}\left(c_{s,\max} - c_s\right)^{\alpha_a}{c_s}^{\alpha_c} \quad \text{..... (4)}$$

where $c_{s,\max}$ is the maximum stoichiometric lithium content in the particular solid host material.

Effective solid and electrolyte transport properties, i.e., diffusivities (D_s^{eff} and D_e^{eff}) and conductivities (σ^{eff} and κ^{eff}) are described in terms of corresponding volume fractions ε_s and $\varepsilon_e = 1-\varepsilon_s$ as exponential relationships of a general form $\Omega^{eff} = \varepsilon^p\Omega$. Exponent *p* could be taken as Bruggeman coefficient of 1.5 or used as an adjustable parameter to fit the discharge curve data [17]. Ionic conductivity of electrolyte can be set as a function of concentration c_e, generally in the form of a polynomial relationship. The diffusional conductivity is determined following the concentrated solution theory as [18].

$$\kappa_D^{eff} = \frac{2RT\kappa^{eff}}{F}\left(t_+^0 - 1\right)\left(1 + \frac{d\ln f_{\pm}}{d\ln c_e}\right) \quad \text{..... (5)}$$

where $f_{\pm}$ is the mean molar activity coefficient of the electrolyte.

The above system of equations can be cast onto any realistic 3D geometry of an electrode with application of corresponding boundary conditions at the solid-electrolyte interface, i.e. the gradient of solid concentration should be equated to the flux of lithium ions as

$$-D_s^{eff}\frac{\partial c_s}{\partial \mathbf{n}}=\frac{j^{Li}}{F} \quad \text{..... (6)}$$

Another modeling approach to describe electrochemistry of a cell under normal operating conditions is based on description of cell behavior from experimentally measured impedance characteristics. The model was originally developed by Newman, Tiedemann [19] and Gu [20] and thus commonly is referred as NTG model. The cell current density (*J*) is linearly related to the cell potential (*V*) as

$$J=Y\left(V-U\right) \quad \text{..... (7)}$$

where *Y* and *U* represent the effective conductance and the open circuit potential (OCP) of the cell respectively. They are expressed as polynomial functions of state of charge variable θ

$$\begin{cases} U=\sum_{i=0}^{N} a_i\theta^i \\ Y=\sum_{i=0}^{M} b_i\theta^i \end{cases} \quad \text{..... (8)}$$

The degree of polynomial (*N*) and the values of constants a_i and b_i are determined from the cell discharge curves for a number of C-rates. When the cell potentials are plotted versus applied current density, the cell voltages at zero current represent the OCPs of the cell and the slopes of potentials represent the cell impedance. Linear dependence of the latter on the current density is assumed resulting in *Y* being a function of state of charge only. As can be seen the NTG model describes the overall cell response and thus cannot be used in situations when local distribution of specific species is of interest. At the same time, being described by polynomial functions, the model provides great savings in compute time and is a suitable tool when fast computation of a large system (module or a pack) response is needed.

The vast majority of the modeling at the module and pack levels has been done with averaging approaches or based on effective electric circuit representations of the cell assembly. Similarly to NTG approach, equivalent circuit models use electric circuits to match the behavior of a cell. Resistance-capacitance circuits (RC-circuits) are typically used. The equivalent circuit model is an effective tool for fast estimation of currents and potentials in battery modules or packs and can be used in on-board diagnostic devices. With some models incorporating degradation and aging [21] such diagnostics provides for fast monitoring of battery pack health. Resistors-based representation of a battery pack allowed development of an approach for localizing a faulty cell in a module in Reference [22]. Module-level computations of the internal short circuit (ISC) were performed by using equivalent circuit model with potential and current values coming from ISC simulation of a single cell. Strategies for localization of ISC were proposed.

In addition to state estimation with techniques such as Kalman filtering [23], [24], [25] and boundary evolution strategy [26] for on-board diagnostics, the equivalent circuit representations of a cell operation can be coupled to some degree with thermal analysis of a module or a pack. The general analysis of equations for equivalent circuit model is available in Reference [27], where the lumped thermal model was used in conjunction with equivalent circuits to estimate temperature in nickel metal hydride traction battery module. In Reference [28] thermal modeling of a car battery module was performed prescribing the ARTEMIS European drive cycle currents. An equivalent circuit model was constructed to calculate the cell potential and the model parameters were obtained experimentally through pulse test measurements. The OCP of the cell was built from the literature data of OCPs for anode and cathode materials. The calculated overpotentials were used to obtain the heat source for the thermal simulation. Thermal solution was coupled to the battery

model via temperature-dependent forms for impedance and OCP. Each cell in the module had averaged properties and the heat source was applied uniformly within the cell, except in the current collector tabs. Modeling of 16P (16 cells connected in parallel) module of cylindrical cells with positive thermal coefficient (PTC) current limiting devices has been performed in Reference [29]. Electrical response was modeled by equivalent circuit model with temperature-dependent resistance of PTC. The modeling was supported by an external short circuit experiment. Thermal response was modeled with lumped thermal model containing 5 nodes along the cylindrical cell axis.

In addition, the equivalent circuit models are helpful in localizing the source of potential or current fluctuations in packs consisting of a large number of cells when highly resolved modeling strategies become computationally expensive. Experimental in-vehicle testing of a battery pack consisting of 504 Kokam lithium-polymer pouch cells was performed in Reference [30]. The pack was composed of modules, 84 cells each in 12Px7S (12 cells connected in parallel in 7 blocks connected in series) configuration. During the acceleration test, the potential in one of the parallel strips in the module experienced an unusual drop. A Simulink model of cells connected via resistors in module was built with empirical formulations of charge and discharge cell potentials in each cell in order to localize the source of the fault causing the potential drop. It was determined that the fault was coming from anomalously high contact resistance in cell interconnects resulting in uneven current flowing through the parallel cells. In this regard, the authors cautioned against highly parallelized design of modules and packs, although such parallel configurations are apparently easier to monitor in drive cycle.

2.2 THERMAL MODELS

In its general form the three-dimensional heat conduction equation is expressed as

$$\rho C_p \frac{\partial T}{\partial t} - \nabla\left(k \nabla T\right) = q \quad \text{..... (9)}$$

where ρ is the density, C_p is the specific heat capacity, $k = \left\{k_x, k_y, k_z\right\}$ is the generally anisotropic thermal conductivity, and T is local temperature. The anisotropy of thermal properties comes from the layered structure of a Li-ion battery cell, where the in-plane conductivity could be several times higher than out-of-plane thermal conductivity. Equation (9) can be applied everywhere in the cell (module, pack), including, for consistency, the pouch material. Computation of the heat source, q, depends on the domain and is represented by the Ohmic heating in electrical interconnect components and current collectors. The general form of the heat generation within electrochemical dual-electrode cell was derived by *Bernardi et al.* [31]. In this rigorous description the heating within the cell, in addition to electrical work, is attributed to electrochemical reactions, changes in the heat capacity of the system, phase changes, and heat of mixing. In simplified form, commonly adopted in battery simulations, the heat generation consists of irreversible energy loss due to cell polarization, reversible entropy change due to particular half-cell reaction and Ohmic heating within the cell sandwich

$$q = \sum_j a_j i_j \left(\phi_s - \phi_e - U_j\right) + \sum_j a_j i_j T \frac{\partial U_j}{\partial T} + \frac{\left(i_s\right)^2}{\sigma^{eff}} \quad \text{.....(10)}$$

where the summation occurs in general over all reactions, j = 1...M, which in the case of Li-ion intercalation system simplifies to two half-cell reactions at each electrode with corresponding OCP vs lithium being denoted as U_j. When NTG model is used, the set of model equations is imposed at

the cell level and the local solid and electrolyte potentials are not known. Thus in this case Eq. (10) is applied in its integral form as

$$q = \left[J\left(\eta - T\frac{\partial U}{\partial T} \right) + \frac{J^2}{\sigma^{eff}} \right] \frac{1}{h} \quad \text{.....(11)}$$

where η is the cell overpotential and *h* is the cell sandwich thickness.

Thermal modeling of modules and packs in many cases has been de-coupled from electrochemical processes with a focus on overall pack cooling strategies without investigating the thermal effects on the cell level. Thermal analysis of a fan-cooled module, which was represented by eight homogeneous rectangular plates approximating Li-ion prismatic cells, was performed in Reference [32]. Analysis was performed at the end of discharge state when each cell was prescribed uniform temperature rise of 9.66 ^{o}C above room temperature. The gap between the cells and the cooling fan speed were varied to find the optimal cooling strategy. A simplified thermodynamics model for packs containing very large number of cylindrical cells was proposed in [33]. Similarly to reference [32], no coupling with electrochemical or electrical models was included and the heat generation rate in the cells was prescribed based on literature data for similar cells. In other cases, the input for the thermal modeling comes from analysis of cell resistance providing the heat source term. In Reference [34], similar to [30], empirical equations for the cell potential at different regions of the discharge curve were used to obtain the overpotential-based heat sources. The electrical model parameters were independent of temperature. Lumped thermal model with uniform temperature in the cells was used to study the lithium iron phosphate based battery pack subject to different driving cycles. The linear cell polarization model [20], [19] was used in Reference [35] to predict the cell potential and to calculate the heat sources within the cell. Lumped cell temperature was employed in pack level thermal analysis, which was decoupled from the cell electrochemical model. The effects of size and shape of cooling air inlets and outlets on the pack temperature were studied.

2.3 APPROACHES TO BRIDGING LENGTH SCALES

Equations 1 and 2 describe the mass and charge balances in electrode and electrolyte domains of a redox cell in three dimensions. Several simplifications to this general description have been developed over the years. One of the better known approaches is the pseudo-2D (P2D) model developed by Newman, Doyle and Fuller [17], [18], [36]. The model is based on porous electrode theory and casts the equations of diffusion and charge transfer onto a simplified geometry. This geometry is described by two coordinates – one through the electrode thickness and the other being radial coordinate of an electrode particle idealized as a sphere. This additional coordinate related to the solid state diffusion in the particle gives the model its name 'pseudo 2D' since it is a one-dimensional approach where transport of species occurs along the thickness direction. Transport through the electrolyte is modeled by using the concentrated solution theory and the lithium ion flux is naturally set to zero in the separator region of the cell sandwich while at the active material interface it follows the Butler-Volmer equation (Eq. (3)). With such simplification, solid state diffusion reduces to a 1D equation in radial coordinate *r* of a spherical particle

$$\frac{\partial c_s}{\partial t} = D_s\left(\frac{\partial^2 c_s}{\partial r^2} + \frac{2}{r}\frac{\partial c_s}{\partial r} \right) \quad \text{.....(12)}$$

In order to reduce compute time, Eq. (12) can be solved either using the Duhamel superposition method [18] or by using approximations for the surface lithium concentration based on the diffusion length formulas derived by reference [14]. In the latter case the approximation for surface concentration can be expressed as [37]

$$c_s = c_{avg} + \frac{j^{Li} l_s}{F D_s}\left[1 - \exp\left(-\frac{4}{3 l_s}\sqrt{D_s t}\right)\right] \quad \text{.....(13)}$$

where $l_s = R_s/5$ is the diffusion length corresponding to a spherical geometry with radius R_s. With such description, the initial surface concentration is equal to the average concentration of lithium in the solid and approaches a linear asymptote at long discharge/charge times of

$$c_{avg} + \frac{j^{Li} l_s}{F D_s} \quad \text{.....(14)}$$

The system described by general equations (Eqs. (1, 2)) is further simplified in the one-dimensional single particle model (SP model) developed originally in [38] for analytical determination of hydrogen diffusion coefficients in metal hydrides [39], [40], [41]. The main assumption of the single particle model is that the reaction current density stays uniform through the electrode thickness. Thus each particle in the electrode experiences the same state of lithiation/delithiation and the whole electrode can be represented by one particle with the surface area characteristic to the active surface area of the electrode. The particle is simplified by a spherical geometry to drive diffusion as a function of radial coordinate only (Eq. (12)). Since the current is uniform across the electrode, the representative spherical particle experiences average flux of lithium ions determined based on the cell current density and electrode active surface area S_a

$$D_s^{eff}\left(\frac{\partial c_s}{\partial r}\right) = -j$$
$$j = \frac{I}{F S_a} \quad \text{.....(15)}$$

Considering the above assumptions the single particle approximation is suitable for thin electrodes and for slow rates of discharge so that gradients do not develop through the electrode thickness.

2.4 APPROACHES TO NUMERICAL COUPLING OF PHYSICAL PHENOMENA

Based on the interaction of the dependent variables different coupling strategies between the physics involved in the battery model can be implemented. When the influence between two states is predominantly in one direction, a one-way coupled numerical technique suffices to get plausible solutions. In a one-way or forward coupling, a set of variables in one of the physics components depends on the solution of the other components, but not vice versa. On the other hand, as the inter-dependence between the variable becomes strong a two-way coupled numerical technique must be used to obtain an accurate solution. In this case, the state variables within the components strongly depend on the solutions of the other components and exchange needs to occur in both directions. Picard iterative method is applicable to fully coupled physics, for example in cases when the interfaces or domains are shared between the two sets of physics. In the case of explicit coupling, the exchange of data between different physics occurs at the end of the time step, while implicit coupling imposes simultaneous solution of all physics.

A two-way coupling via the temperature-dependent cell resistance was implemented in thermal analysis of a Li-ion battery module in Reference [42]. A 2-dimensional ANSYS/FLUENT CFD modeling of a cylindrical cell module consisting of 32 cells subject to air flow perpendicular to the cylinder axis of cells was performed. The heat source coming from each cell was approximated as ohmic heating only, i.e., $q = I^2 R(T)$ with I being the applied current as a function of time and R being the temperature-dependent resistance of the cell. The latter was approximated as a third

order polynomial function of temperature. The validation was done with eight cylindrical cells (A123 26650, 2.3 Ah) arranged into 2Px4S module with air cooling provided by the fan and the temperature of the cells measured with thermocouples attached to the top sides of the cells. Based on the results of CFD computations and experiments, a reduced order two-zone model was suggested in which the temperature of the cells is uniform in the columns belonging to the same zone; the zone temperature depends on the distance from the air inlet and on the air flow rate. The model can be used in on-board assessment of module temperature. However, due to the lack of coupling with electrochemical model, the distribution of SOC as well as non-uniformities in potential distribution across the cells cannot be obtained. Similar approach was undertaken in Reference [43] where the authors report on 2D thermal modeling of prismatic battery stack and 3D thermal modeling of cylindrical battery pack to investigate the effects of width of cooling channels and air flow velocity. The heat generation in the cells was assumed to be uniform throughout the pack and the heat source was approximated based on the experimental measurements of cell resistance as a function of state of charge and temperature.

Finally, some modeling efforts describe coupling with electrochemical models that incorporate processes occurring at the microscale. In this case the formulation of heat release rate from the cell sandwich becomes more rigorous and allows for two-way coupling with thermal analysis through temperature-dependent reactions and open circuit potentials. A pseudo-2D electrochemical model [18] was applied in conjunction with a lumped thermal model to obtain characteristics of a 72-cell module during pulse current tests in [44]. The temperature was assumed to be uniform within a cell and no variations in SOC or potential was assumed among the cells integrated in the module. A more rigorous approach was undertaken in Reference [45] where a model of a module with three prismatic cells connected in series was built and solved for potential and temperature gradients. A pseudo-2D model for cell electrochemistry was coupled to the thermal solution through volume averaging of the variables in the heat source term. High thermal gradients (up to 6 ^{0}C) were observed in the cell tabs as a result of thermal analysis.

2.5 SOFTWARE

Numerous software tools have been developed or adapted to model the physical phenomena associated with the normal operation of batteries. Some examples are listed in Tables 1-3.

The Virtual Integrated Battery Environment (VIBE) provides a common simulation environment that includes several of these capabilities [11]. Fig. 1 conceptually illustrates the package architecture of VIBE, including the Python-based Open Architecture Software (OAS), developed under the DOE/EERE CAEBAT program, which provides the integrating framework for VIBE.

Of particular value for this project was the 3D electrochemical, electrical, and thermal capability provided by AMPERES.

Table 1. Electrochemical

Tool	Source	Comment
DualFoil	http://www.cchem.berkeley.edu/jsngrp/	freely-available
Battery Design Studio	http://www.cd-adapco.com/	commercial
EC-Power	http://ecpowergroup.com/	commercial
AMPERES	http://batterysim.org/	freely-available
MATLAB-based models (e.g. MSMD)	http://www.mathworks.com/ and component developers	commercial, NREL, LBNL
Python-based models (e.g. PyECM, PyDFN)	https://www.python.org/ and component developers	freely-available
COMSOL Battery & Fuel Cell module	http://www.comsol.com/	commercial

Table 2. Electrical

Tool	Source	Comment
AMPERES	http://batterysim.org/	freely-available
MATLAB	http://www.mathworks.com/	equivalent circuit models, commercial
COMSOL AC/DC module	http://www.comsol.com/	commercial
ANSYS	http://www.ansys.com/	commercial
Star-CCM+	http://www.cd-adapco.com/	commercial

Table 3. Thermal

Tool	Source	Comment
AMPERES	http://batterysim.org/	freely-available
MATLAB	http://www.mathworks.com/	commercial
COMSOL Heat Transfer module	http://www.comsol.com/	commercial
ANSYS	http://www.ansys.com/	commercial
Star-CCM+	http://www.cd-adapco.com/	commercial

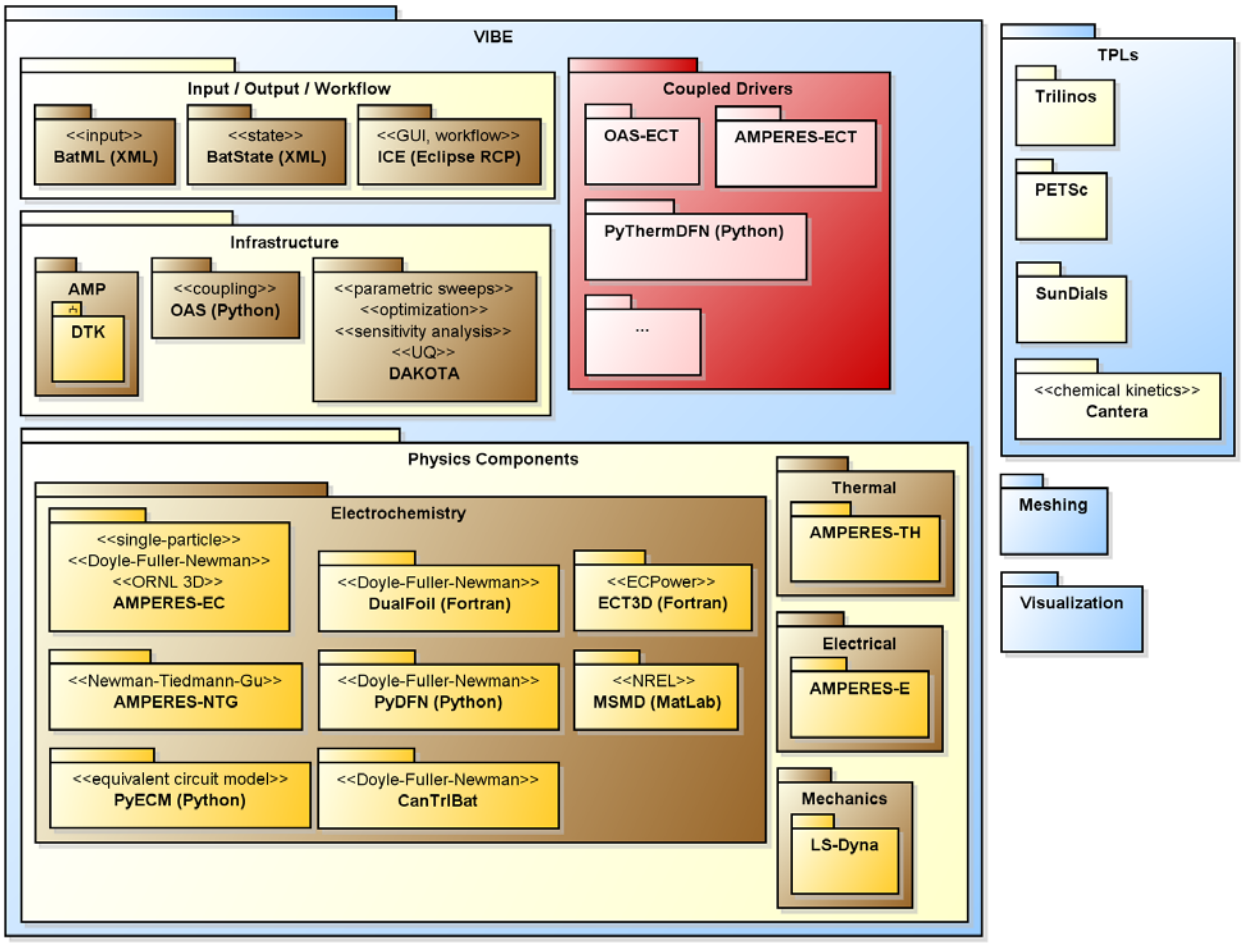

Fig. 1. UML package diagram for VIBE

3. MODELING OF BEHAVIOR UNDER ABNORMAL CONDITIONS

This section concentrates on modeling approaches for scenarios when the electrochemical system is driven very far from equilibrium possibly resulting in catastrophic failure of a Li-ion battery. Such scenarios may involve externally applied mechanical loading, leading to severe displacements, external and internal short circuits, and thermal abuse that would trigger exothermic side reactions inside the cell. Thus, the list of physics that has to be included during the normal cell operation needs to be augmented by:

- rapid discharge under short circuit conditions
- mechanics (impact, nail penetration)
- side reactions

3.1 SHORT CIRCUIT AND THERMAL RUNAWAY

The current abuse tests are carried out at a cell level using methods such as short circuit [46], nail penetration [47], oven tests [48], pinch test and crushing and operation of cell under overcharged conditions [49]. Each of these conditions can lead to local heat generation arising from multiple factors by physical contacts between partially/fully charged electrodes, electrolytes, current collectors, oxygen generation etc. A typical Li-ion cell is an assembly of multiple composite electrode materials casted on metallic current collectors, liquid electrolytes, and polymeric separators and packaging [50]. The operation of the Li-ion cell involves complex interplay between the cell constituents, and their thermal and electro-chemical properties are important design parameters, as they determine the overall safety of the cells. The heat of reaction, also referred to as the enthalpy change (ΔH), is estimated as the difference between the sum of the heat of formation of all the constituent products and that of the reactants [51]. An overall negative ΔH implies the reaction is exothermic while positive ΔH indicates that the reaction is endothermic. Under constant pressure, the temperature change associated with a reaction is a measure of ΔH . The heat change is then measured by monitoring the temperature as follows:

$$\Delta Q = mC_p \Delta T \tag{16}$$

where *m* is the mass, C_p is the specific heat and ΔT is the temperature difference. The other method of determination of ΔH is based on the Hess Law [51], which states that enthalpy change for a reaction depends on the products and reactants and is independent of the pathway or the number of steps between reactants and products. In other words, if a reaction is carried out in a series of steps, ΔH for the reaction will be equal to the sum of the enthalpy changes for the individual steps. Therefore, the enthalpy change for a given reaction is calculated by taking the sum of the enthalpy changes associated with each of these individual chemical equations. Most of the reactions involving lithium metal or lithium compounds are known to be exothermic. In an earlier work Spotnitz et al. [52] have listed various potential exothermic reactions possible for lithium-ion batteries and their onset temperatures. The details are discussed in a later section on properties.

3.1.1 EXPERIMENTS ON CONTROLLED INTERNAL SHORT CIRCUIT DUE TO SEPARATOR FAILURE

In any form of mechanical abuse of Li-ion battery, maintaining the integrity of the separator appears to be a key factor in prevention of internal short circuits. While the technologies to improve abuse tolerance have been developed and many are in use (these include Positive Temperature Coefficient (PTC) parts, safety vents, Current Interrupt Devices (CID), etc.) mechanisms leading to internal short circuit and subsequent thermal runaway are still not completely understood. This lack of understanding is based in part on difficulties associated with repeatability of the internal

short experiments. It is rather hard to precisely control the location, size and resistance of the internal short circuit during experiments in order to connect these variables with the experimentally measured external thermal response of the cell. In addition there is unavoidable manufacturing variability and gaps in quality control during the cell assembly that can lead to the production of defective cells and the addition of yet another variable to the system.

In order to minimize the variability associated with inducing the internal short by large external mechanical loading, the Battery Association of Japan (BAJ) developed a test procedure [53] for artificially induced internal short circuits. In this test, a cell is disassembled and a small nickel particle is placed between the anode and the cathode. The cell is then put back together then, and the internal short is achieved by applying pressure so that the separator is punctured by the particle. This test was adopted by Celgard, LLC in a study for evaluating the models for exothermic side reactions [46]. While the location of the internal short can be controlled with reasonable accuracy, the size and resistance of the short circuit may not be controlled well and could be influenced by the neighboring electrode layers in the cell. The test was modified by Celgard, LLC [54] so that more accurate representation of contact occurring during the short circuit could be achieved. In the modified experiment, a small hole of predefined size is made in the separator at the desired location. Application of pressure on the cell induces the internal short circuit in that location. Without the Ni particle, contact occurs directly between the layers; different combinations of contact pairs can be achieved by local removal of electrode material within the area corresponding to the hole in the separator.

It was determined that the maximum temperature rise and thus the highest likelihood of thermal runaway is attributed to the cells where the shorting occurs between anode and aluminum current collector. The lowest thermal peak was observed when Cu current collector made contact with cathode material. If exothermic side reactions are ignored, the temperature rise of the cell during the internal short would be dictated by the local electronic resistance of the contact area, amount of current flowing through the short area (i.e. SOC) and the thermal conductivity of the components. Thus the internal short occurring between Cu and Al current collectors is very similar to external short between the cell positive and negative tabs simply due to significant heat dissipation via current collectors. Therefore the final temperature rise is mitigated despite the significant amount of energy associated with such short due to very low short resistance. Out of four possible contact scenarios, the highest temperature increase was observed for Al-anode contact. In this scenario high conductivity of both aluminum and graphite anode results in high-energy short circuit since the heat cannot be dissipated as efficiently as in the Al-Cu contact case. Table 4 shows the maximum temperature achieved in 1 Ah prismatic cell at different SOC and three different short scenarios [54].

Table 4. Maximum temperature rise and voltage drop in the controlled ISC tests.

	Temperature rise, C^0			Voltage drop		
SOC	Anode-Cathode	Anode-Al	Nail	Anode-Cathode	Anode-Al	Nail
60%	50	157	124	0.11	3.26	3.42
80%	81	225	113	0.34	3.2	3.58
100%	106	257	135	0.74	3.86	3.75

3.1.2 EXPERIMENTS ON MECHANICAL ABUSE

The response of the cell/module/pack to the external mechanical loading is checked in the abuse experiments in order to evaluate the behavior of electrochemical energy storage systems under extreme loads. Several tests have been developed over the years [55]and a majority of them have been standardized (Table 5). Out of different abuse scenarios, the three most relevant in terms of causing internal short circuit and thermal runaway are crush, impact and penetration tests. The latter evolved from the early tests by the Battery Association of Japan [56] through extensive testing at Sandia National Laboratories [57], and the final standard was adopted by SAE International as the J2464 Standard [58]. It should be noted that in the original recommendation in SAND2005-3123 Abuse Test Manual [57], a rather high speed of penetration (8 cm/s) was specified as opposed to slow penetration (1 mm/s) in BAJ recommendations. The test was described as penetration of a steel conductive rod that should be 3 mm in diameter for single cells and 20 mm in diameter for modules. Modifications to the penetration tests have been proposed where the penetrating rod ('nail') was designed to contain a thermocouple to measure the temperature during slow penetration [59].

The safety tests developed by the Underwriters Laboratories and later adopted into the United Nations Recommendations on transport of Li-ion batteries [60] prescribe the impact testing applicable to cylindrical cells greater than 20 mm in diameter. A 15.8 mm 316 stainless steel bar is placed across the middle of the cell and 9.1 kg mass is dropped onto the bar from a height of 61 cm. UN 38.3 T.6 Crush Test Standard is applicable to prismatic, pouch, coin and cylindrical cells. The cell is crushed between two flat surfaces with 1.5 cm/s speed at the point of first contact. The crushing stops when any of the following conditions occur:

- The applied force reaches 13 kN
- The voltage of the cell drops by at least 100 mV
- The cell is deformed by 50% or more of its original thickness.

The passing criteria for the above tests include no fire within 6 hours of the test and the temperature of the cell during the test not exceeding 170 ^{0}C.

Table 5. Standards for mechanical abuse testing of batteries

	UL		SAE	UN	IEC	
Test	UL 1642	UL 2054	J2464-200911	38.3 T6	IEC 2133:4.3.6	IEC62133:4.3.4
crush	●	●	●	●	●	
impact	●	●		●		●
penetration			●			

Internal short circuit experiments were developed at ORNL based on the "door knob" test originally started at Motorola Mobility in Lawrenceville, GA [61]. It had a better quality control option compared to the nail penetration tests. However, the tests were found to cause too much damage to the cells and could not test high capacity cells (>1 Ah). The test developed at ORNL was on a servo hydraulic MTS load frame and had better control of the displacement and load. A systematic study was carried out using parameters such as loading speed, indenter diameter, voltage drop sensitivity

and post-short circuit action. Larger capacity cells with up to 2.0 Ah capacity were capable of being tested at 100% State-of Charge (SOC). The pinch-test was sensitive enough to distinguish cell safety factors using regular and ceramic-coated separators.

Further development at ORNL added a torsion factor into the pinch test. Due to the highly plastic deformation behavior of the separators, the cell stack (jelly roll) must be compressed to over 60% of the original thickness to induce short circuit. It was realized that a slight torsion results in more consistent short circuit. The new torsion-compression pinch test was able to give a Thermal Runaway Risk (TRR) factor to the cell, making it possible to select safer cells from various designs. Simulations of the pinch-torsion tests were also carried out at ORNL.

The pinch and pinch-torsion tests were extended to large format cells under a DOE Vehicle Technology Office program in collaboration with the Naval Surface Warfare Center (NSWC). Li-ion cells with capacity of more than 15 Ah were tested at the Carderock MD facility using the motor-driven load frame developed at ORNL. Large format cells tested included 18 Ah lithium iron phosphate (LiFePO4 - LFP) cells and 25 Ah NMC cells. The pinch-torsion test was able to evaluate LFP cells with 100% SOC and NMC cells with 60% SOC.

3.1.3 CELL THERMAL RUNAWAY

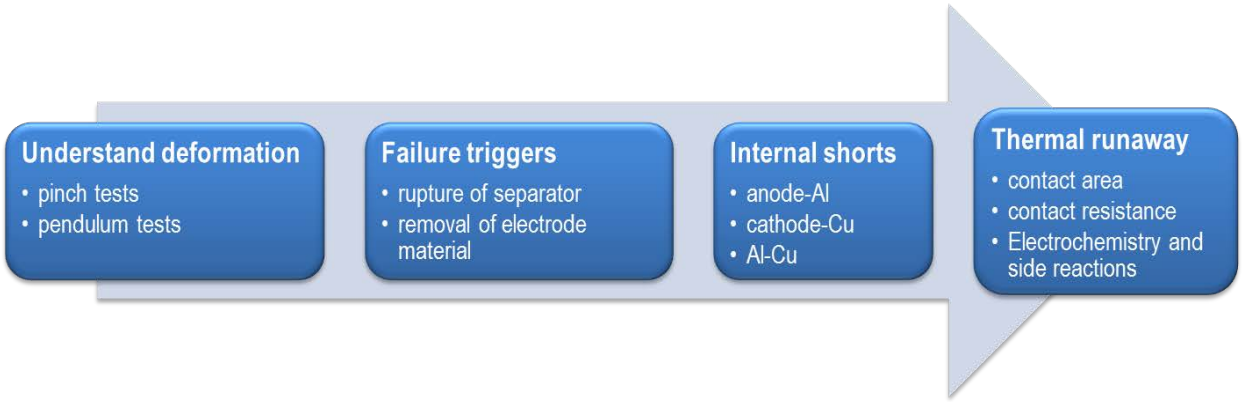

Fig. 2. Mechanical deformation leading to thermal runaway

Mechanical deformation [9] of the batteries can trigger thermal runaway events as shown in Fig. 2. The deformation (through abuse) leads to rearrangement of electrode material, transfer of normal and shear stresses to the separator, and eventually, rupture of the separator [13]. This can lead to various internal shorts such as between the anode and aluminum collector, cathode and copper collector, or even aluminum and copper collectors [54], [62]. These electrical contacts may have complex configuration and the subsequent thermal runaway event will depend on the contact area, contact resistance, cell capacity, and the ability of the current through this short to generate sufficient heat to cause the local temperature to rise above ~90 ^{o}C to trigger the thermal runaway events described earlier.

3.1.4 PROPERTIES

This section summarizes the properties necessary for successful modeling of cell electrochemical and thermal behavior under abuse conditions. Under normal battery operation (close to equilibrium), the system can be described by the set of equations discussed in Section 2 along with the corresponding set of properties and material constants such as electrode and separator porosity, electrolyte conductivity, cation transference number, and so on. While better studied than for instance mechanical properties of electrodes, many of those constants are not available in the literature. When the cell operates under abnormal conditions (thermal abuse or short circuit)

additional models are required to evolve the state of the battery in time. Such models require additional set of constants, such as activation energies for side reactions as well as contact resistances for the internal short circuit.

Reaction parameters can be determined experimentally using differential scanning as well as accelerating rate calorimetry (DSC and ARC respectively) techniques. The accelerating rate calorimeter was used in References [63], [64] to determine thermal stability of lithiated carbon (mesocarbon microbeads - MCMB) anode with ethylene carbonate (EC) and diethyl carbonate (DEC) based electrolytes containing $LiPF_6$ and $LiBF_4$ salts. ARC results showed that self-heating of anode powder in electrolyte starts at 80 ^{0}C when $LiPF_6$ is used as a salt. The self-heating profile revealed an initial peak of approximately 100 ^{0}C, with position relatively independent of the degree of lithiation in the anode. Since the self-heating associated with electrolyte decomposition does not occur until the sample temperature reaches 190 ^{0}C, this peak was attributed to the decomposition of the solid-electrolyte interface (SEI) and formation of stable inorganic layer. It is interesting to note that subsequent self-heating rate depended significantly on the lithium content in the sample and the heating rate actually decreased in partially delithiated (0.127 V vs Li) anode ($Li_{0.25}C_6$). This indicated consumption of Li as temperature increased which was confirmed by the X-ray diffraction (XRD) studies.

Reactions of electrolyte ($LiPF_6$ in EC:DEC) with cathode were studied by both ARC and DSC methods in References [63], [64], [65]. $LiCoO_2$ as well as $LiMn_2O_4$ cathodes were studied [66], [67], [68], [69]. In addition, thermal reactions between lithium nickelate ($LiNiO_2$) and different solvents in electrolyte were investigated using DSC in [70]. It was determined that the reactions between solvent and $LiCoO_2$ initiate at about 130 ^{0}C while reactions with $LiMn_2O_4$ start at about 200 ^{0}C.

Based on the experimental results and relying on an excellent review in Reference [52] the following reactions can be considered as playing major part in Li-ion cell self-heating under abuse scenarios:

1. Reaction between lithium in anode with electrolyte solvent: Negative-Solvent (NS)
2. Positive decomposition (positive-solvent, PS). Positive material can react directly with solvent [69] or decompose and release oxygen that combusts solvent according for example to:
   $Mn_2O_4 \rightarrow Mn_2O_3 + 0.5O_2$
   $2.5O_2 + C_3H_4O_2 \rightarrow 3CO_2 + 2H_2O$
3. SEI decomposition. The SEI layer consists of stable (Li_2CO_3) and metastable species ($(CH_2OCO_2Li)_2$). The latter react exothermically converting to stable SEI:
   $(CH_2OCO_2Li)_2 \rightarrow Li_2CO_3 + C_2H_4 + CO_2 + 0.5O_2$
4. Electrolyte decomposition. Ethylene carbonate (EC) can decompose into carbon dioxide and ethylene oxide and the latter can decompose exothermically. PF_5 gas coming from electrolytes with $LiPF_6$ salt ($LiPFF_6 \rightarrow LiF+PF_5$) reacts with EC.
5. Reaction of lithium in anode with binder (negative-binder, NB). The temperature for the onset of this reaction is typically high (240 ^{0}C) and the reaction completes at 350 ^{0}C.

The rate of each i-th reaction (approximating the reactions as first order) is described by equation

$$R_i = k_i \varphi(c_{ij}) \quad \text{..... (17)}$$

with the kinetic rate constant following the Arrhenius expression

$$k_i = k_{0,i} \exp\left(-\frac{E_{a,i}}{RT}\right) \quad (18)$$

and c_{ij} being the dimensionless amount of species j participating in reaction *i*. The amount of species changes with time as

$$\dot{c}_{ij} = \pm R_i \quad (19)$$

The cumulative heat source representing all of the exothermic reactions triggered is expressed then as

$$q = \sum R_i H_i \quad (20)$$

with H_i being the reaction heat of the *i*-th reaction.

The function $\varphi(c_{ij})$ is chosen for each reaction as follows.

1. **Negative-solvent reaction (*i=1*)**

$$\begin{cases} \varphi(c_{11}) = (z_0/z)(a/a_0)\exp(-z/z_0)c_{11} \\ \dot{z} = R_1 \\ \dot{c}_{11} = -R_1 \end{cases} \quad (21)$$

Where c_{11} is the dimensionless fractional amount of Li in carbon anode available for reaction 1, z is the dimensionless fractional amount of Li in SEI per unit of surface area, a is the anode specific surface area, and a_0 is constant. Rate equations for z and c_{11} have opposite signs because the SEI thickness increases as the concentration of intercalated lithium decreases.

2. **Positive-solvent reaction (*i=2*)**

$$\begin{cases} \varphi(c_{22}) = c_{22}(1-c_{22}) \\ \dot{c}_{22} = R_2 \end{cases} \quad (22)$$

Where c_{22} is the dimensionless fractional amount of cathode that has reacted with the electrolyte (degree of conversion). The reaction is assumed as first order.

3. **SEI decomposition (*i=3*)**

$$\begin{cases} \varphi(c_{31}) = c_{31} \\ \dot{c}_{31} = -R_3 \end{cases} \quad (23)$$

Where c_{31} is the dimensionless amount of Li in metastable SEI.

4. **Electrolyte (solvent) decomposition (*i=4*)**

$$\begin{cases} \varphi(c_{44}) = c_{44} \\ \dot{c}_{44} = -R_4 \end{cases} \quad (24)$$

Where c_{44} is the dimensionless fraction of non-decomposed solvent in electrolyte.

5. **Negative-binder (*i=5*)**

$$\begin{cases} \varphi(c_{55}) = (z_0/z)(a/a_0)\exp(-z/z_0)c_{11}c_{55} \\ \dot{c}_{55} = -R_5 \end{cases} \quad (25)$$

This is the reaction between Li in the anode and the binder and thus depends on both the amount of lithium c_{11} and dimensionless fraction of unreacted binder c_{55}.

The following three tables summarize the reaction constant, heats and initial concentrations based on the results available in literature.

Table 6. Activation energies and frequency factors for thermal abuse reactions

Reaction	E_a(J/mol)	k_0 (1/s)	*Ref*
Negative – solvent (Li_xC_6)	2.0 x 10^5	1.95 x 10^{20}	[52]
	1.3508 x 10^5	2.5 x 10^{13}	[69]
Positive – solvent (Li_xNiCoO_2)	3.94 x 10^5	7.25 x 10^{39}	[52]
Positive-solvent (Li_xCoO_2)	1.396 x 10^5	6.667 x 10^{13}	[71]
	1.235 x 10^5	6.667 x 10^{10}	[67]
	1.235 x 10^5	6.667 x 10^{11}	[69]
Positive – solvent ($LiMn_2O_4$)	2.18 x 10^5	1.06 x 10^{18}	[52]
SEI decomposition	2.81 x 10^5	7.88 x 10^{36}	[52]
	1.3508 x 10^5	1.667 x 10^{15}	[69]
Electrolyte decomposition	2.74 x 10^5	5.14 x 10^{25}	[52]
Negative-binder	1.67 x 10^5	1.79 x 10^{13}	[52]

Table 7. Reaction heats

Reaction	H(J/g)
Negative – solvent	350 – 1714 (1714)
Positive – solvent ($LiCoO_2$)	265 – 625 (314) (257)
Positive – solvent ($LiMn_2O_4$)	350 – 450
SEI decomposition	186 – 257 (257)
Electrolyte decomposition	155 – 285 (375 J/g for 1:1 EC:DMC and $LiPF_6$)
Negative-binder	1100 - 1500 (1700)

*Values without brackets are from literature data reported in Reference [52], values in brackets were picked from References [69] and [71] and can be used in simulations involving $LiCoO_2$ cathode and EC:DMC + $LiPF_6$ electrolyte.

Table 8. Initial values of variables and other constants

Description	Value
Initial value of c_{11}	0.75 (beginning of discharge *)
Initial value of z (z_0)	0.033
Initial value of c_{31}	0.15
Initial value of c_{22}	0.04
Initial value of c_{44}	1.0
Initial value of c_{55}	1.0
a/a_0	1.0

* this value should come from electrochemical solution for a specific SOC.

3.1.5 Gaps and Challenges

While the recent efforts at development of standardized methods to probe internal shorts in Li-ion cells have led to significant progress, the precise mechanisms and events leading to internal short circuit and thermal runaway are still not completely understood. There remains considerable uncertainty about the short mechanism, and the extent of failure of the separator. It is not clear if there is flat contact between the electrodes over an extended area, or if the contact is more localized because of fracture of the current collectors, which then pierce through the separator. This is an important aspect that needs to be well understood, because the contact area determines the short resistance, which in turn controls the amount of heat generated at the shorted region, and it is not easily measured during the experiment. The location and size of the internal short are hard to control in the experiment, and therefore they need to be estimated based on measurements of the external thermal response of the cell.

Another important aspect that needs to be better understood is the role of ion transport in the vicinity of the short. Once a short has been initiated, the presence of higher temperatures and gradients can lead to variations in the transport properties compared to normal cell operation. In addition, the time scales of the event are so fast that under such conditions certain assumptions (e.g. charge neutrality) may no longer be valid, and these are not typically accounted for in the simulations. Another aspect that is often not considered in the simulations is the change in properties of the different cell components due to degradation with time or repeated cycling of the cell. These parameters are often based on materials in their raw or unused state, and some of the parameters, especially for the electrochemical models, may need to be adjusted. Numerically, the electrochemical system of equations is very stiff, and the high rates at the advent of the short make the system extremely difficult to solve.

3.2 Mechanics of Battery Cells

3.2.1 Background

With increased usage of lithium ion batteries in automotive applications there is a critical need to address safety of battery packs in the event of crush induced by collision with another vehicle or road debris. One of the biggest challenges is lack of understanding of mechanical behavior of batteries under impact loading.

A lithium-ion pouch cell consists of stacked positive and negative electrodes that are kept apart by a

porous polymeric separator to prevent an internal short circuit of the cell. Active electrode materials are coated on copper (anode) or aluminum (cathode) thin foils and the whole structure is encased in metalized polymer pouch. The pouch is composed of aluminum foil with polyamide and polypropylene layers on both sides bonded together by polyester-polyurethane and urethane-free adhesive respectively. Graphite is the commonly used anode material; for cathode $LiCoO_2$, $LiFeP0_4$ and $LiMn_{0.3}Ni_{0.3}Co_{0.3}O_2$ are the most common materials. Cylindrical cells are formed by winding the strips of electrode pairs and separator, and encasing the resulting roll in a stainless steel protective tube with end caps. Due to metal casing, cylindrical and prismatic cells have a higher structural integrity than pouch cells, but they are also heavier. The structure consisting of electrodes and separator but without protective enclosure is termed as jelly roll; mechanical properties of this structure are of the greatest interest because that is where the electrical short occurs during impact.

The conceptual representation of the Li-ion cell structure at different length scales is shown in Fig. 3, with typical sizes in Table 9. We define electrode, as a metal foil (current collector) coated with composite coating consisting of active material particles, conductive additives and binder. We term the pair of electrodes with the separator a cell sandwich - the macroscopic unit which when repeated represents the complete layered structure of the cell. Details of one such unit are shown in Fig. 3 together with the corresponding microstructure of the positive electrode coating, which in this particular case contains particles of $LiMn_{1/3}Ni_{1/3}Co_{1/3}O_2$. Finally, the large cathode particles (usually termed as secondary particles) are agglomerates of much smaller primary particles, as shown in Fig. 3(c). The internal structure consists of materials that have significantly different mechanical properties, i.e. highly ductile copper and aluminum and brittle particles of metal oxides that are bonded together by a resin-like binder to maintain integrity of the electrode coating. Overall, the structure is transversely isotropic and as at first approximation can be homogenized by isostrain and isostress approaches in the in-plane and out-of-plane directions respectively. However, an accurate description of mechanical behavior that includes internal failures would require resolving all the layers involved in cell sandwich structure.

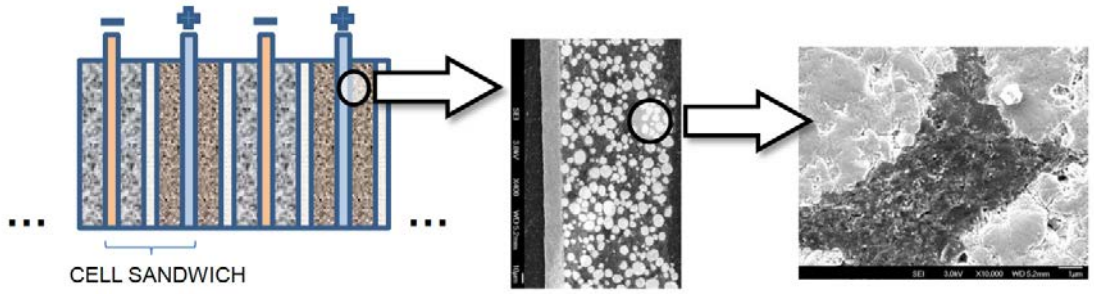

(a) (b) (c)

Fig. 3. (a) Hierarchical structure of Li-ion cell: (a) cell sandwich as a repeating unit; (b) cathode coating containing secondary particles; (c) zoom-in showing agglomerates of primary particles.

Table 9. Specification of cell components

Component	Material	Typical Thickness/µm
Cover Sheet	Polyamide	120
Copper layer	Copper foil	11
Anode	Graphite	65
Separator	Polypropylene	25
Cathode	$LiMn_{0.3}Ni_{0.3}Co_{0.3}O_2$	80
Aluminum layer	Aluminum foil	19

3.2.2 MECHANICAL EXPERIMENTS

Building models for Li-ion batteries requires experimental work that provides both the data for mechanical behavior of individual components of the cell (foils, separator, pouch, etc.), as well as validation data for simulations of internal short circuit induced by mechanical abuse. In Table 10 various experiments performed by several research groups either for material parameter extraction or for validation of computational models are summarized together with corresponding references. Detailed explanation for the tests are given in the Sections 3.2.2.1 – 3.2.2.3.

Table 10. Types of experiments investigating mechanical abuse of lithium ion cells

Test	Objective	Ref
Tension/ Compression of individual components such as anode, cathode, separator, cover sheet and current collector	Experimental data for development of macro homogenized material models	[72-77]
Compression of the whole cell	Calibrate the material properties of jelly roll; validation of FE model	[73], [78-80]
Indentation/bending test of the whole cell representing mechanical abuse leading to short circuit and failure	Validation of Finite Element Model, Load Value at which short can occur	[74-76]

3.2.2.1 Tension/compression tests of individual cell components

Tensile tests [72]-[77] have been performed to obtain the nominal stress-strain curves of the individual components of the cell. ASTM E8/E8M-11 standard was followed for tensile test specimen design. Nominal strain rate of 0.0017 sec^{-1} was applied.

Due to the layered structure of Li-ion cells, micrometer scale thicknesses and high aspect ratios, compressive tests on individual cell components (i.e. electrodes) are difficult. Therefore, compression experiments were performed involving several cell components stacked together. In addition, the whole jelly roll/pouch cell was subjected to compression in some instances, and the

response was matched by calculating effective properties from properties of individual components [73], [74]. Details of such experiments are described in the next section. Due to transversely isotropic properties of layered Li-ion cell structure, compression experiments were done in out-of-plane (OP) [73] as well as in in-plane (IP) [72], [74] directions. Since the cell electrodes are not bonded to each other and are simply contained by the cell pouch, testing in out-of-plane tension appears unfeasible.

The calculated moduli of elasticity in tension (E_t) and out-of-plane compression (E_c) available from literature are arranged in Table 11. The tensile load bearing capability of electrode coatings was estimated by dividing the load by the cross-section area representing the metal foil alone. In both cases of positive and negative electrode this resulted in values of Young's modulus very close to those of aluminum and copper respectively, indicating very weak tensile stiffness of electrode coatings [72]. The values in Table 11 represent the elastic moduli obtained by normalizing the load to the total cross-sectional area and thus include properties of electrode coatings. A factor of two difference in out-of-plane compressive modulus of elasticity between anode and cathode should be noted from Table 11, while the tensile properties of the positive and negative electrodes are very similar since they reflect the tensile modulus of the metal foil and binder that keeps the active material particles together.

The effective elastic modulus determined for in-plane compression ($E_{c,eff}$) of different components in Reference [74] is also arranged in Table 11. In-plane compression was performed under constrained conditions by inserting a 5 mm thick stack of corresponding component sheets into a slot in a die with 0.4 mm slack. The compression was then performed by a rectangular punch moving at 0.5 mm/min inducing quasi-static constrained compression at strain rate of 0.0003 s^{-1}. Such configuration induces plane strain condition in the in-plane direction of the specimen. The effective elastic modulus for in-plane compression is $E_{c,eff} = E/\left(1-\nu^2\right)$, where E and ν are respectively the elastic modulus and Poisson's ratio in compression.

Values of the Young's modulus in out-of-plane compression in Table 11 come from Reference [73]. The layers of the same cell component were stacked together and compressed between two flat plates with the crosshead speed of 0.5 mm/min. It should be mentioned that the positive electrode in Reference [73] was $LiCoO_2$ as opposed to $LiFePO_4$ in Reference [3]. OP compression of pouch material was not studied in Reference [73].

Table 11. Mechanical properties of cell components in tension and compression

	Pouch	Negative Electrode	Positive Electrode	Separator	Ref
E_t / GPa	5.6	4.7	5.1	0.5	[72]
σ_0 / MPa	65	11	12	100	[72]
ε_f	0.52-0.57	0.017-0.031	0.009-0.015	0.5-0.8	[72]
E_c /GPa (OP)	…	1.6	3.2	0.6	[73]
$E_{c,eff}$/ GPa (IP)	0.575	0.083	0.275	0.09	[74]

E_t Young's modulus in tension
σ_0 Ultimate tensile strength
ε_f Fracture strain

E_c Young's modulus in compression
$E_{c,eff}$ Effective Young's modulus in constrained compression

Fig. 4 shows a comparison between stress-strain curves obtained from in-plane and out-of-plane compression of different components with data taken from [73], [74]. Initial linear elastic part in in-plane compression corresponds to deformation prior to elastic buckling of the sheets; the effective moduli in Table 11 are calculated from linear fits of this part of stress-strain curve indicated by dashed black lines in Fig. 4. Curves from OP compression in Fig. 4 display non-linear compaction and reduction in porosity, followed by a linear elastic part, which corresponds to elastic behavior of dense material in compression. It should be noted that the experiments on OP compression of stacked components of Li-ion cell revealed zero dimensional change in IP direction indicating zero Poisson's ratio [73], [74].

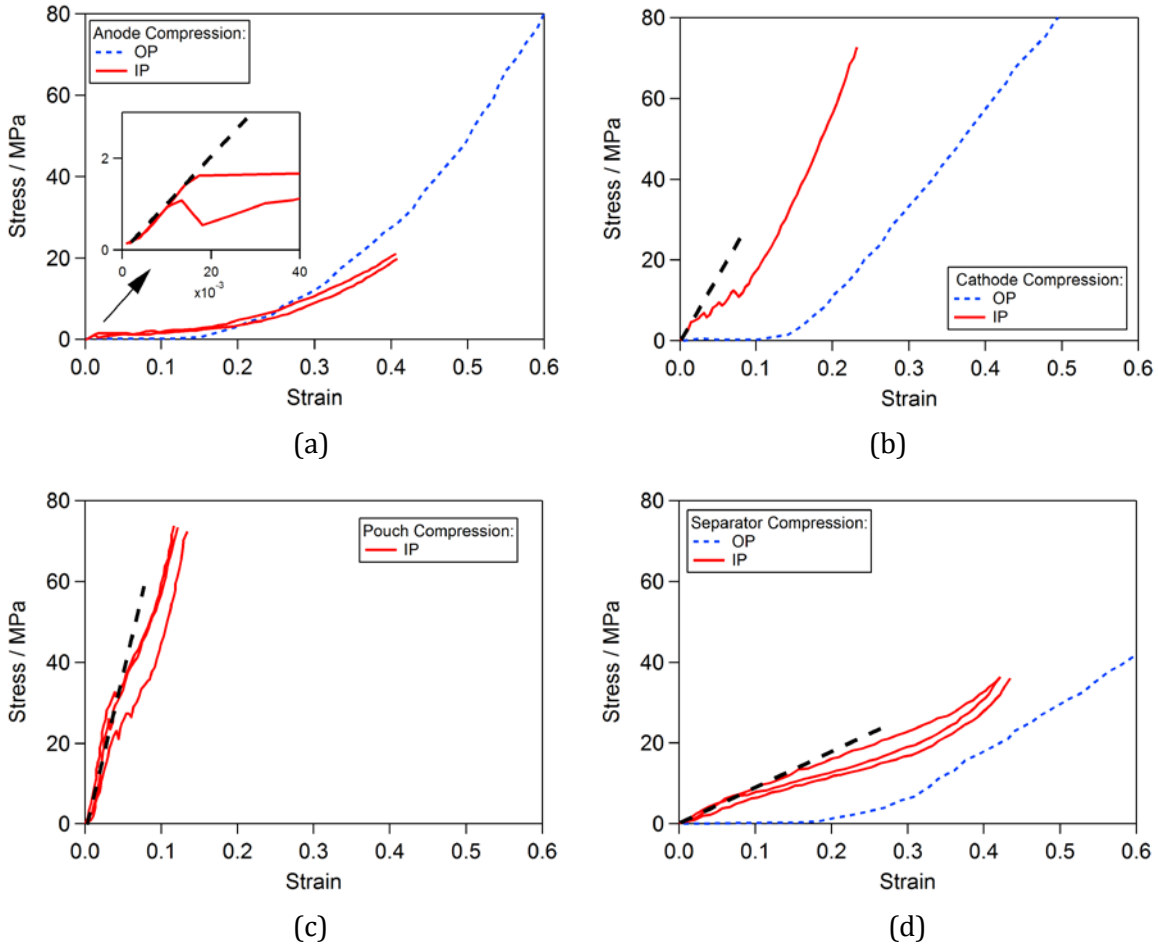

Fig. 4. IP [74] and OP [73] compression stress-strain curves of different cell components: (a) anode, (b) cathode, (c) pouch material, (d) separator.

Fig. 5 shows tensile stress-strain curves of different cell components [72]. Large disparity in tensile strength and ductility can be observed between different components, which makes homogenization of layered battery structure difficult beyond the initial elastic response.

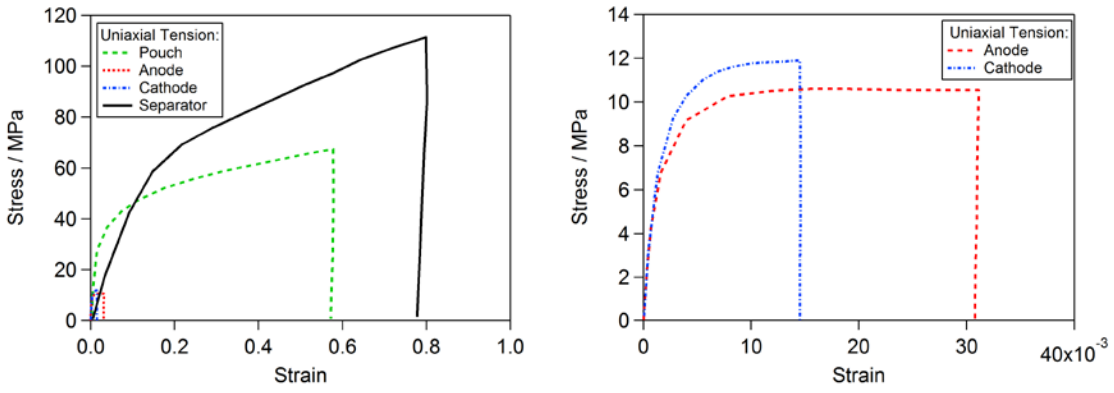

(a) (b)

Fig. 5. Stress-Stain plot for individual components of the cell [72]

Very low tensile strength of electrode composite materials deduced from the experiments in Reference [72] was directly confirmed by measuring stress-strain response of free-standing electrode coatings in Reference [75]. The cathode under investigation was $Li[Ni_{1/3}Mn_{1/3}Co_{1/3}]O_2$ and experiments targeted investigation of calendering effect on electrochemical performance as well as mechanical behavior. Cathode slurry was first cast onto the aluminum foil, dried and calendered at different pressures to desired porosity (ranging from 50% to zero). Then the electrode coatings were carefully detached from the aluminum current collector and mounted into a Chatillon TCD 225 force measurement system [75]. The results of tension experiments show significant dependence of Young's modulus on calendering pressure (Table 12). The overall strength of the composite coatings however remained very low; even severely compressed laminates to near zero porosity showed breaking stress of only ~2 MPa. The electronic conductivity of electrodes did not change significantly with calendering.

Table 12. Strength and modulus of elasticity in tension for Li[Ni1/3Mn1/3Co1/3]O2 cathode as function of electrode porosity [75]

Porosity	Breaking Strength (MPa)	Young's Modulus (GPa)
0 %	1.7 ± 0.4	0.27 ± 0.05
10 %	1.3 ± 0.3	0.16 ± 0.03
20 %	1.0 ± 0.25	0.14 ± 0.025
30 %	0.7 ± 0.15	0.12 ± 0.01
40 %	0.3 ± 0.1	0.04 ± 0.005
50 %	0.2 ± 0.05	0.01 ± 0.005

Similar approach was used in Reference [76] to study tensile strength of anode coatings. The mechanical properties of the free-standing composite films were studied as a function of processing parameters for electrode coating fabrication.

All electrodes were fabricated with the same materials but using different mixing sequences; details of those can be found in Reference [76]. The strength of the negative electrode laminates was studied in the same setup as in Reference [75] using the stretching speed of 1.25×10^{-3} mm/s. The findings were rather peculiar: the strength of anode coatings did not correlate with the preparation technique, while the elastic modulus appeared to have a strong dependence on the mixing sequence

for electrode preparation. The results are arranged in Table 13 preserving the same nomenclature for marking the sample groups corresponding to different mixing orders as in Reference [76]. Order of magnitude difference in Young's modulus can be noticed between samples from groups A and E. Unlike in cathodes [75], processing influences only Young's modulus in the case of negative electrodes. Comparison with Table 12 shows much higher strength for graphite-based anodes even when compared to NMC positive electrode fully densified by calendering. The porosity of graphite anodes was maintained at 35% for all the samples; this was achieved by calendering to an experimentally established gap that provides the desired value of porosity [76].

Table 13. Strength and modulus of elasticity in tension for graphite anodes as function of slurry mixing sequence [76]

Sample	Breaking Strength (MPa)	Young's Modulus (GPa)
A	4.1 ± 0.2	0.7 ± 0.1
B	3.9 ± 0.2	0.16 ± 0.03
C	3.8 ± 0.15	0.14 ± 0.025
D	3.9 ± 0.2	0.12 ± 0.01
E	4.0 ± 0.2	0.04 ± 0.005

Several investigations on mechanics of battery separators revealed the anisotropy of properties in tension as well as strain rate sensitivity of many commercial separators. Properties of Celgard separators in tension were studied in Reference [77] under load control at 6.66 MPa/min. Very strong anisotropy of properties was observed. The anisotropic structure of this class of separators comes from the manufacturing technique that produces porous sheets through crazing (Fig. 6). Results from Venugopal et al [78] confirmed anisotropic behavior of separators. The stress-strain curves of the separators (Fig. 7) provide clear difference between tensile behavior in transverse and machine directions (TD and MD respectively). While a major portion of the stress-strain curves from MD oriented samples can be approximated by a linear elastic material, the TD-tested specimens showed a clearly defined yield stress and material flow. A higher value for strength of separator in machine direction compared to transverse direction is observed.

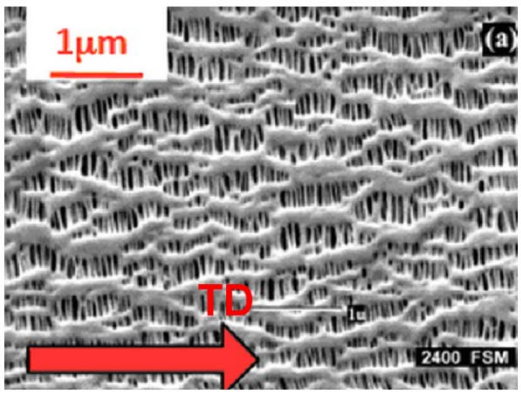

Fig. 6. Microstructure of Celgard 2400 separator [77] showing the transverse direction (TD); the man machine direction (MD) is perpendicular to TD.

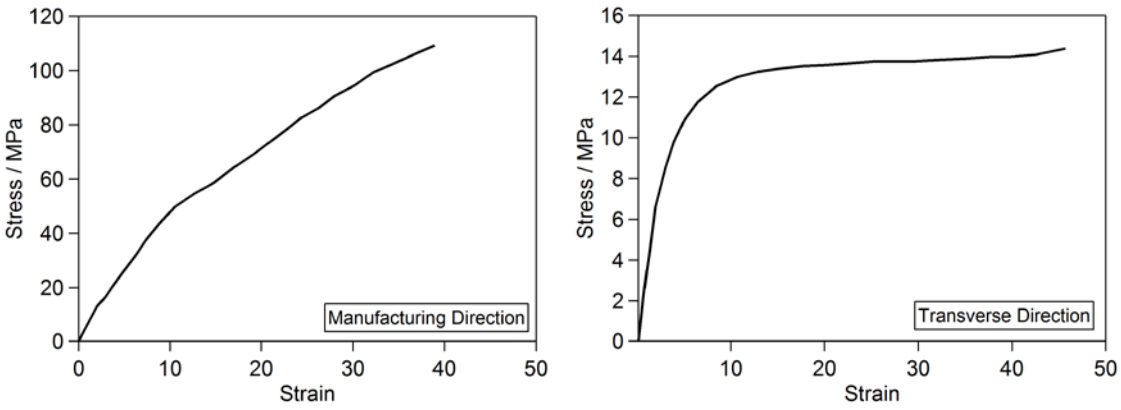

(a) (b)

Fig. 7. Tensile stress-strain curves of dry Celgard 2400 separator in (a) MD, (b) TD [77]; The strain is in %.

Anisotropy of thermo-mechanical properties (creep) of polymeric separators was observed in Reference [79]. The experiments were performed by running a thermal ramp while holding a Celgard 2320 separator at static tensile load of 0.015 N. The temperature rate was 10 ^{0}C/min from 35 ^{0}C until rupture of the specimen. The results in Fig. 8 show complex response as a function of temperature. When held along the manufacturing (axial) direction the separator internal structure starts shrinking and final rupture occurs at temperature beyond the melting temperature of the separator. More complex deformation occurs in TD, where several phases of deformation can be found (Fig. 8). The shrinkage force and release of internal stress after manufacturing are greater then applied force during the experiment, thus the shrinking phenomenon is observed. In TD, positive strain is followed by shrinking at around the melting temperature of PE which in turn is followed by extension and necking up to final rupture. One interesting aspect of thermal deformation in TD is the presence of a zero strain point along the deformation path, occurring at temperature denoted as T_0 in Fig. 8.

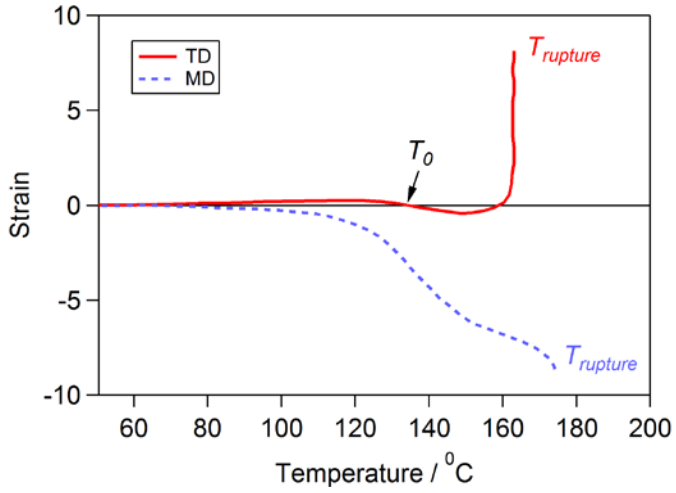

Fig. 8. Anisotropic thermomechanical behavior of Celgard 2320 separator [79]

Effect of liquid electrolyte filling the pores of the separator was studied by testing separators immersed in 1.1 M LiPF6 EC/DMC electrolyte and pure DMC [77]. The Young's modulus of wet separator in MD was found to be almost 2 times lower than that of a dry Celgard sample. Properties

in transverse direction were not influenced significantly by presence of liquid electrolyte or DMC solvent.

Avdeev et. al [80] observed similar behavior for Celgard 480 in tension. The studies were performed under different strain rate and temperature and it was observed that the separator is effectively stiffer at higher strain rates or low temperature. Young's modulus and failure strain determined from tensile tests of different dry separators [81] are summarized in Table 14.

Table 14. Tensile Properties of separators [81]

Separator	Thickness (µm)	Porosity [%]	Direction	Elastic modulus (MPa)	Strain at failure [%]
Celgard 2325	25	39	MD	935 ± 43	155.9
Celgard 2325	25	39	TD	510 ± 24	164.9
Celgard 2400	25	41	MD	873 ± 37	164.3
Celgard 2400	25	41	TD	502 ± 28	164.2
Toray V20EHD	20	42	MD	675 ± 25	333.2
Toray V20EHD	20	42	TD	781 ± 39	241.5
Toray V20CFD	20	43	MD	696 ± 48	547.7
Toray V20CFD	20	43	TD	823 ± 52	453.2

Gor et al [82] had carried out compressive tests in both dry and wet condition on Celgard 3501 separator. The modulus of elasticity and the flow stress are found to be dependent not only on dry or wet testing conditions but also on strain rate. In comparison to tensile test, when loaded in compressive mode wet separator is stiffened considerably at higher strain rate. Behavior in tension can be modeled using viscoelastic formulation, but under compression poroelasticity formulation needs to be included.

3.2.2.2 Compression of pouch cells

Effective properties of jelly roll in compression can be determined from qausi-static compression between flat plates. In References [73, 74, 83] Li-ion cells were compressed between two flat plates with the speed of compression varying from 0.5 to 3 mm/min. Tests are performed on dry cells and with flat plate and thus no short circuit or thermal events are observed. Similarly to testing stacks of cell components, the experiments on full cells can be done in in-plane and out-of-plane modes revealing anisotropy of the layered structure. The results from References [73] and [74] are shown in Fig. 9. The same setup as discussed in the previous section for cell component compression was used to compress the full cells. The cell in Reference [73] (Cell 1) was a Li-polymer pouch cell with $LiCoO_2$ as positive electrode paired with graphite. The cell in Reference [74] (Cell 2) was a $LiFePO_4$ based pouch cell with considerably thicker electrodes due to higher active material loading. Same speed of 0.5 mm/min was applied in both cases.

The results in Fig. 9 demonstrate qualitatively similar behavior from both types of cells. The mechanical properties for the two cells however appear to be different and $LiCoO_2$ based cell shows higher initial stiffness. This emphasizes the necessity for constitutive models on electrode level and formulation of models where the component layers are fully resolved in order to avoid conducting experimental testing every time the Li-ion cell parameters and geometry changes. It should be mentioned that the overall cell response in Reference [74] was matched by combining the properties from individual component testing (see Section 3.2.2.1) and applying corresponding iso-strain or iso-stress homogenization formulations.

Similar to the case of compression of individual electrodes, OP compression of a full cell reveals minimal deformation along the lateral direction, which is the basis for assuming a crushable foam material model of active material for numerical simulations. Since Poisson's ratio is close to zero volumetric strain is taken the same as the strain in the compression direction. Such assumption is applicable considering that the electrode coatings constitute up to 80% of the cell volume.

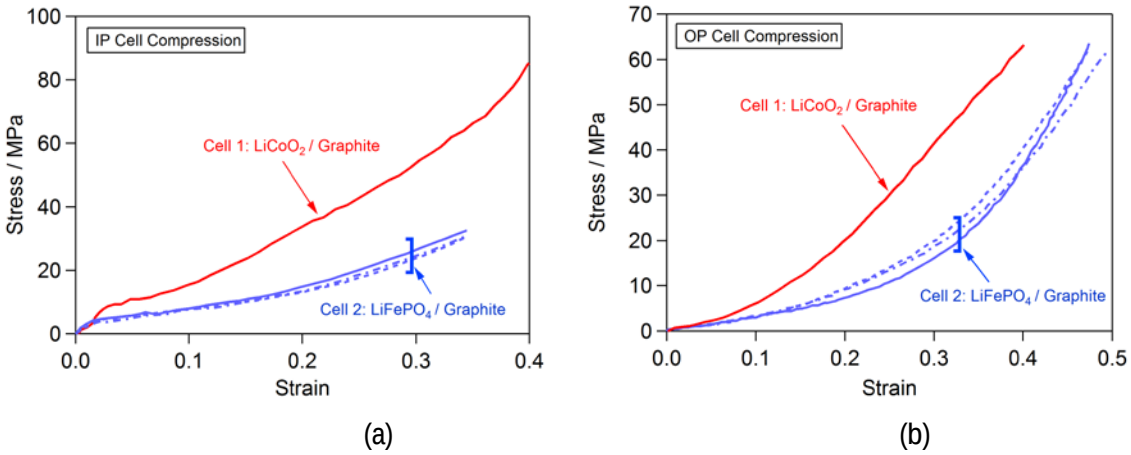

Fig. 9. In-plane (a) and out-of-plane (b) compression of $LiCoO_2$ [73] and $LiFePO_4$ [74] pouch cells

3.2.2.3 Lateral Indentation of cells

In this type of test the cell is indented by different punches varying in shape (conical/hemi-spherical) and diameter (Fig. 10b). Upon short circuit in any of the indentation tests, a drop in voltage coincides with a drop in load [84]. Drop in load is caused by failure of one of the components and once failed it can also reduce the load carrying capacity of other constituents. A comprehensive study of response of pouch cells to indentation and formulation of corresponding models was done in Reference [84]. Small (740 mAh), medium (3.2 Ah) and large (19.5 Ah) pouch cells were tested. Maximum load at which short occurred increased with punch diameter, due to increase in contact area. No short was observed when the medium size cell was subjected to out-of-plane compression between two flat plates [84] even though the load exceeded 60 kN. This suggests that uniform compression of layered cell structures will not lead to separator failure and short circuit, and that the presence of shear and tensile strains is necessary to trigger failure. Mechanical properties of the large pouch cell were determined by indentation with a flat cylindrical punch since the compression between the plates resulted in loads exceeding the load cell capacity. In this case, the short circuit was induced by sharp edges of the punch cutting through the cell pouch [84]. Force-displacement curves for all indentation cases are shown in Fig. 10(c). It should be noted that tests on partially charged and fully discharged cells did not reveal any dependence of mechanical behavior on state of charge.

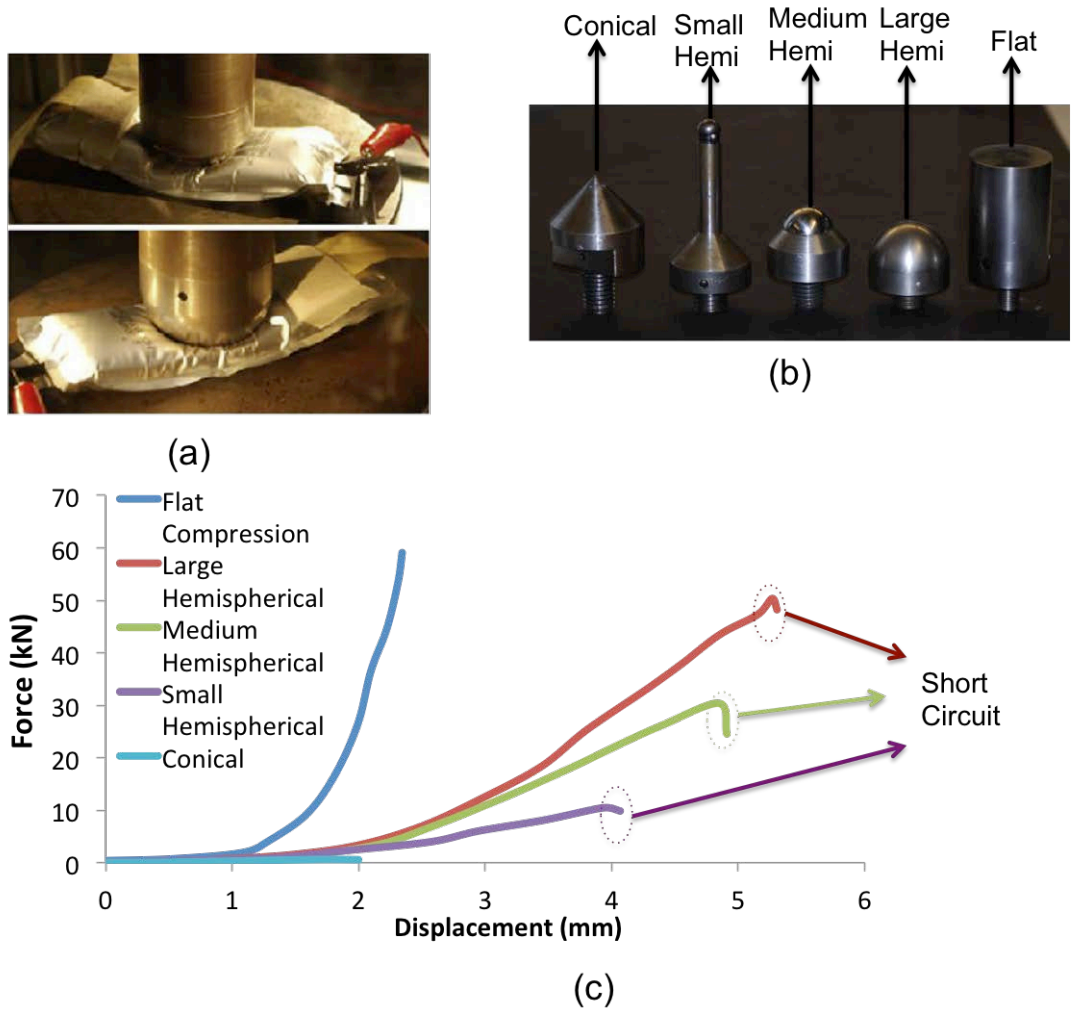

Fig. 10. Punch indentation test (a) Deformation of cell (b) indenters used (c) load-displacement curves [84]

3.2.3 COMPUTATIONAL MODELS FOR BATTERY MECHANICS

There are two main approaches for developing the computational model to predict the strength and deformation of a battery under different loading conditions. In the first approach the behavior of the cell's layered structure is described by one material possessing effective properties. These are estimated by performing a set of mechanics tests on a cell (or string of cells). In the other approach the jelly roll is treated as laminated composite and individual layers are assigned properties based on the appropriate material behavior.

3.2.3.1 Homogenized Models

Mechanical response of pouch and cylindrical Li-ion cells was modeled in [73], [84, 88] using Finite Element (FE) analysis with homogenized material models for jelly roll. Conditions that lead to internal short circuit in the cell were also investigated in some instances.

Pouch cells with varying cell chemistries ranging in capacity from 740 mAh to 19.5 Ah were studied in Reference [84]. State of charge was less than 10 percent to prevent extreme reactions during indentation tests. Finite element simulations were performed using LS-DYNA. The cells were modeled using fully integrated solid elements. The hemispherical/conical punches were modeled

using rigid shell elements. Crushable foam material model (MAT-63) was used to describe the constitutive behavior for the cell. This constitutive model type was selected due to large through thickness compressibility of battery cells and other similarities between the deformation regimes for the two systems. The crushable foams deform primarily by compression, and are relatively weak in shear and tension. These weakness tendencies can be used to accentuate distortional deformation in the battery cells and use it for indicating failure in the separator and, thereby, onset of short circuit. Stress-strain (compressive stress and strain are treated as positive) relation for this material model is shown in Fig. 11. In Fig. 11 σ_i and ε_υ denote principal stress and volumetric strain respectively. Outside the elastic regime ($\sigma_i = E\varepsilon_\upsilon$) the material behavior is described by the yield surface [84]

$$\begin{aligned} & f_i = \left|\sigma_i\right| - Y \\ & \begin{cases} Y = Y_C + H(\varepsilon_\upsilon), & \sigma_i > 0 \ (\textit{compression}) \\ Y = Y_t, & \sigma_i < 0 \ (\textit{tension}) \end{cases} \end{aligned} \tag{26}$$

The value for compressive stress cutoff (Y_c) was negligible for all cells. Stress-strain curve obtained from compression between flat plates was used as an input for stress and volumetric strain in the region outside compressive yield. Area of tensile stress state develops under the indenter during the indentation; the material failure in this area is controlled by the tensile cut-off stress (Y_t), which is typically used to describe failure in concrete. In Reference [84] the value of Y_t was adjusted until the simulation would match the onset of short circuit in small punch indentation tests. In this manner, Y_t was determined for each cell, and ranged from 10 MPa for cylindrical cell to 30 MPa for medium-sized pouch cell. It should be noted that the tensile cut-off parameter varies depending on the method used to obtain its value. Different assumptions can be used to estimate Y_t : in Reference [73] it was calculated as a function of yield strength of individual components and in Reference [88] it was set equal to tensile strength of negative electrode (10 MPa). The latter approach is worth the attention since the failure stress of Celgard separator in transverse direction [78] is rather close to that value (Fig. 7).

Load and displacement during deformation, as well as onset of short circuit observed from experiments, was closely predicted by simulations [73] as shown in Fig. 12. Simulations were also performed by varying shape/size of indenter and size of cell [84] and it was concluded that homogenous and isotropic constitutive model of the jelly roll is suitable for a range of battery chemistries, cell sizes and loading conditions.

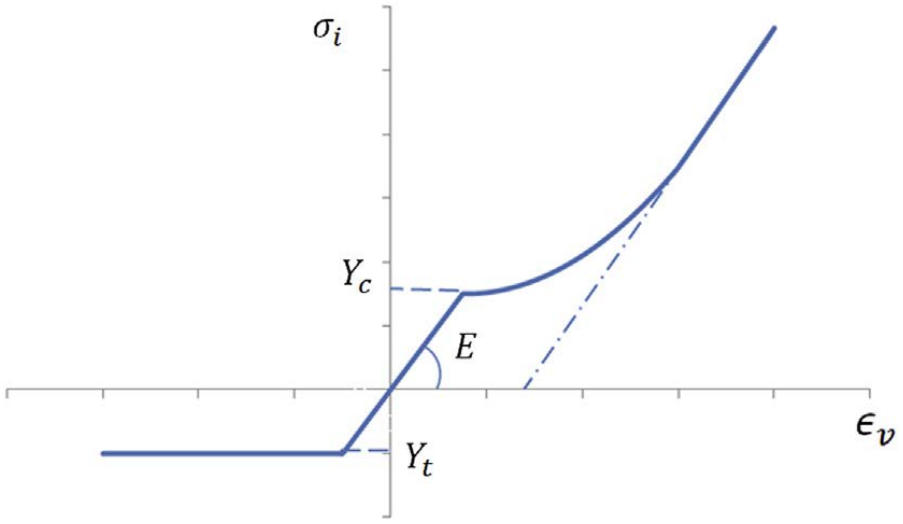

Fig. 11. Constitutive behavior for the active material described using crushable foam material model [84]

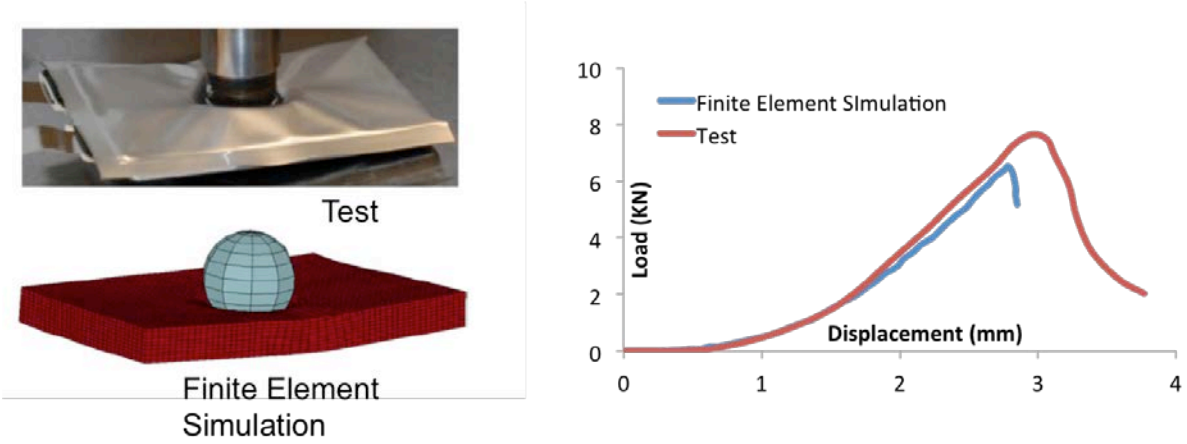

Fig. 12. Deformation and load-displacement history of the cell during punch indentation simulation. [73]

In Reference [85] a homogenized model was developed to simulate the in-plane constrained punch indentation test of lithium-ion battery module specimen. Material parameters for homogenized model were obtained from in-plane constrained compression test performed on the representative volume element (RVE) of a Li-ion module as schematically shown in Fig. 13(b). The RVE contained 14 cell sandwiches, adhesive foam separating the cells in module and the aluminum cooling plate inserted between two cells. For in-plane punch indentation test the module RVE specimen was placed in the die cavity and punch was moved downward with a displacement rate of 0.6 mm/min (Fig. 13(a)). Simulations were performed using ABAQUS finite element code. 2-dimensional plane strain 4-node finite elements CPE4R were used. The hyperfoam and crushable foam with isotropic hardening material models were used to model the constitutive behavior of the module. The desire to capture large compressibility of the cell is again evident from the material model selection. The hyper foam material model is based on the hyperelastic theory with use of the strain energy function and is suitable for quasi-static loading conditions. The crushable foam model can be used when rate-dependent effects are important. Details about these two models along with calibration procedure to determine material constants are described in Reference [85].

Predicted load-displacement curves using two different constitutive models in ABAQUS finite element analysis are compared to experimental results in Fig. 13(c). Overall good agreement can be

observed, with hyperfoam model making somewhat closer prediction at the later stage of compression. The models however failed to capture the initial stiffening during the in-plane indentation.

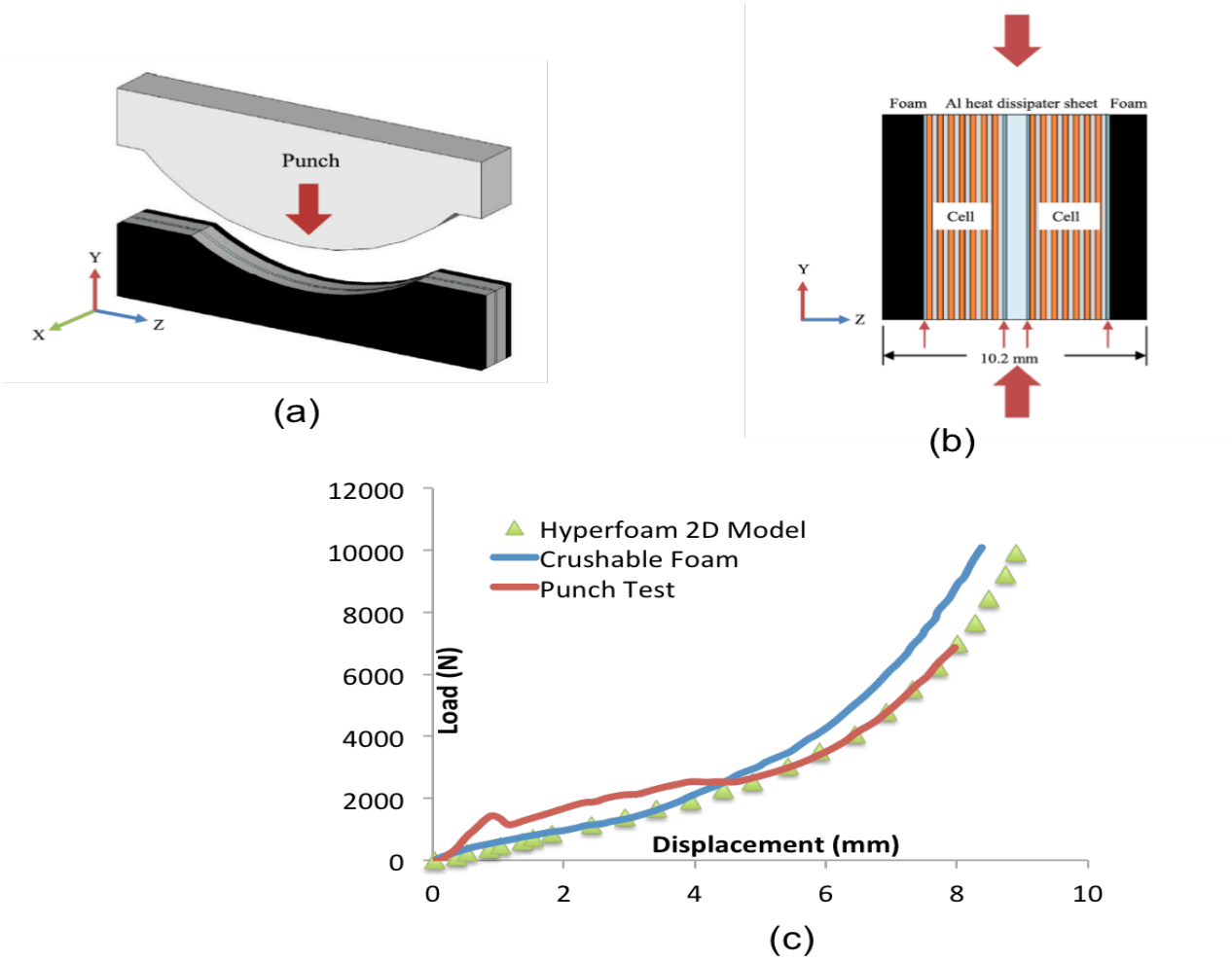

Fig. 13. Punch Indentation (a) Module Specimen under a punch test
(b) Schematic of module specimen along with individual components
(c) Load displacement curve from finite element analysis and test results. [85]

Greve and Fehrenbach [86] developed a finite element model for various loading conditions (radial crush, indentation and bending) of large 200 mm long and 60 mm diameter cylindrical cells. The commercial explicit code Virtual Performance Solution (VPS) was used for numerical analysis. The model of the cell included the steel casing and caps represented by shell elements, and the homogenized jelly roll with volume elements, For modeling, jelly roll was treated as a homogenized, isotropic material as shown in Fig. 14 and its compressive behavior was modeled using a pressure dependent yield criterion given by Eq. 27. Material properties for jelly roll had been calibrated from radial crushing load test.

$$f = \bar{\sigma} - R\left(\bar{\varepsilon}^{p}\right) = 0 \tag{27}$$

where $\bar{\sigma}$ is equivalent stress which can be simplified to standard Von Mises description for isotropic material

$$\bar{\sigma} = \sqrt{\frac{3}{2} S_{ij} S_{ij}} \tag{28}$$

with $S_{ij} = \sigma_{ij} - \frac{1}{3}\delta_{ij}\sigma_{kk}$ being deviatoric stress.

Analytical function for hardening curve is given as [86]

$$R\left(\bar{\varepsilon}^{p}\right) = \left[\sigma_{plateau} - \left(\sigma_{plateau} - \sigma_{yield}\right)\exp\left(-\frac{\bar{\varepsilon}^{p}}{\bar{\varepsilon}_{ref}}\right)\right]\left(1 + s\left(\bar{\varepsilon}^{p}\right)^{m}\right) \tag{29}$$

where calibrated parameters for radial crush tests are σ_{yield} = 0.0003 GPa, $\sigma_{plateau}$ = 0.0006 GPa, $\bar{\varepsilon}_{ref}$ = 0.009, *s*=1000, and *m* = 2.7. In this hardening model $\bar{\varepsilon}_{ref}$ dictates the shape of the hardening curve in between initial yield (σ_{yield}) and plateau stress ($\sigma_{plateau}$). The strain hardening behavior is controlled with the two constants *s* and *m*.

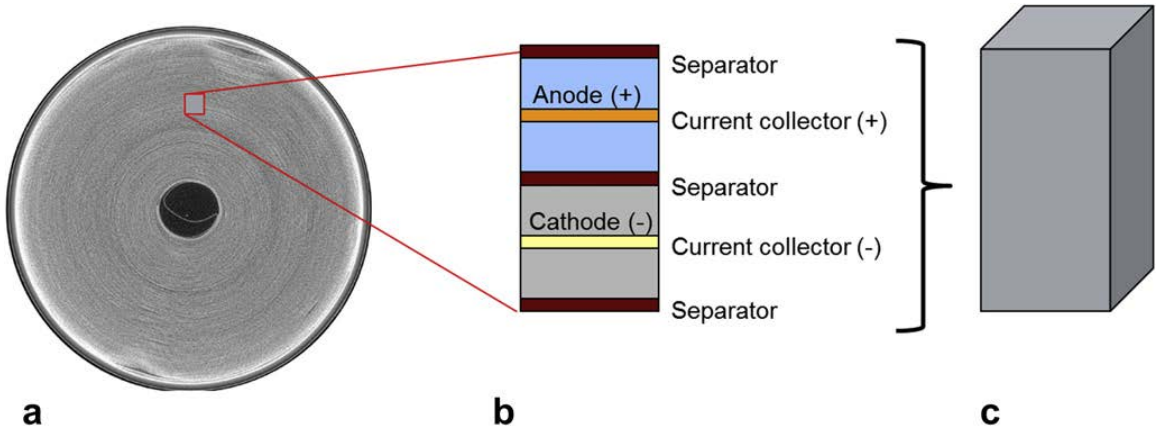

Fig. 14. RVE for jelly roll (a) cross-section of jelly roll (b) individual components (c) Isotropic continuum [86]

Load displacement curves obtained from simulation for various load cases were in good agreement with experiments. Being a homogenized model it fails to take into account interaction of individual jelly roll components (anode, cathode and separator) upon mechanical loading, such as folding and fracture of individual layers.

Avdeev and Gilaki [87] conducted experimental and numerical characterization of large cylindrical cells used in EV/HEV applications under lateral compression. Finite element simulation was performed using LS-DYNA and crushable foam material model was used for the jelly roll. Drop test on cylindrical cell was performed to validate results of numerical simulation.

3D finite element model for crushing the jelly roll between two rigid flat plates is shown in Fig. 15 (a). This model was used for validation of experimental results. In this model bottom plate is fixed and top plate is moved at a constant speed. Load-displacement curve obtained from simulation is compared with test results in Fig. 15(b). This study did not consider failure of cell under external loading.

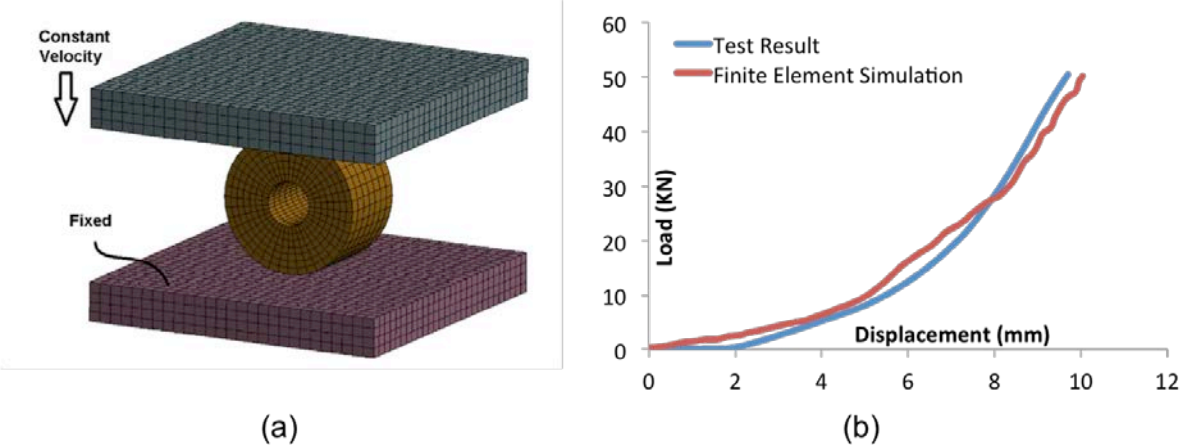

Fig. 15. Lateral compression of cylindrical battery (a) Finite Element Model of jellyroll during crushing (b) comparison of load-displacement curves from lateral jelly roll tests and simulation [87]

In computational simulations discussed in this section a homogenized material model for battery cell is formulated, by using either direct experimental homogenization [73], [84 - 86] or by hybrid experimental/analytical approach [83] and the failure criteria is driven by phenomenological parameters that depend on experiments and mesh conditions.

3.2.3.2 Layer-resolved (Non-Homogenized) Model

An alternative way of modeling the jelly roll is treating it as a laminated composite and predicting the onset of short circuit based on the properties of a system of individual layers of cover sheet, positive and negative electrode coatings, current collectors (aluminum and copper) and separator.

In Reference [88] a computational model using ABAQUS explicit solver was developed to study the behavior of battery cell under in-plane constrained compression test, details of which are described in Section 3.2.2.1 of this report. Pouch cell was modeled as layered composite. Schematic of geometry along with boundary conditions and mesh is shown in Fig. 16(a). Gurson's model [Reference 91] (usually used to simulate the plastic behavior of porous metals) is used to model active materials and separator in finite element analysis. This model attempts to account for the compressibility of the active material and plastic deformation of the electrode foils. Yield function for this computational model, modified by Tvergaard [89], is given by Eq.30.

$$\phi = \frac{\sigma_e^2}{\sigma_y^2} + 2fq_1 \cosh\left(\frac{q_2}{2}\frac{\sigma_m}{\sigma_y}\right) - \left(1 + q_3 f^2\right) = 0 \qquad (30)$$

where σ_e is equivalent stress in Von Mises representation, σ_y is yield stress, and σ_m is mean stress (hydrostatic pressure); q_i, $i = 1,2,3$ are fitting parameters, and f is porosity. The value of the latter was equal to 0.2 [88]. The values of fitting constants were chosen as q_1 = 1.5, q_2 = 1.0, and q_3 = 2.25 to better represent material subjected to plane strain condition [89]. It is noted that for fully dense material (*f=0*) the model Eq. (30) transforms to Von Mises yield criterion.

Compressive elastic moduli of individual cell components were determined from constrained compression tests (see Section 3.2.2.1). Stress-strain data in plastic region obtained from tensile test of an individual component was used to define plastic strain hardening behavior. Frictional contact is assumed at all interfaces and value for coefficient of friction is obtained by parametric

study. Fully integrated solid elements are used to model the anode, cathode and separator. Along the thickness direction one element is used for each layer. Finite element model for an individual cell is shown in Fig. 16(a).

Under in-plane compression loading dense layers (current collectors such as copper and aluminum) are buckled by pressing the softer porous layers of active material and separator. Due to this deformation a kink band is formed as shown in Fig. 16(b). Kink/shear bands and load-displacement curve obtained from numerical simulation were similar to those obtained from experiment (Fig. 16(d)). The model is capable of capturing the initial stiffening, - a feature that was not properly simulated by applying crushable foam constitutive behavior for fully homogenized models of cells [85]. Adding more elements along thickness and using in-plane compression test data to obtain the strain hardening behavior may possibly improve accuracy of simulation.

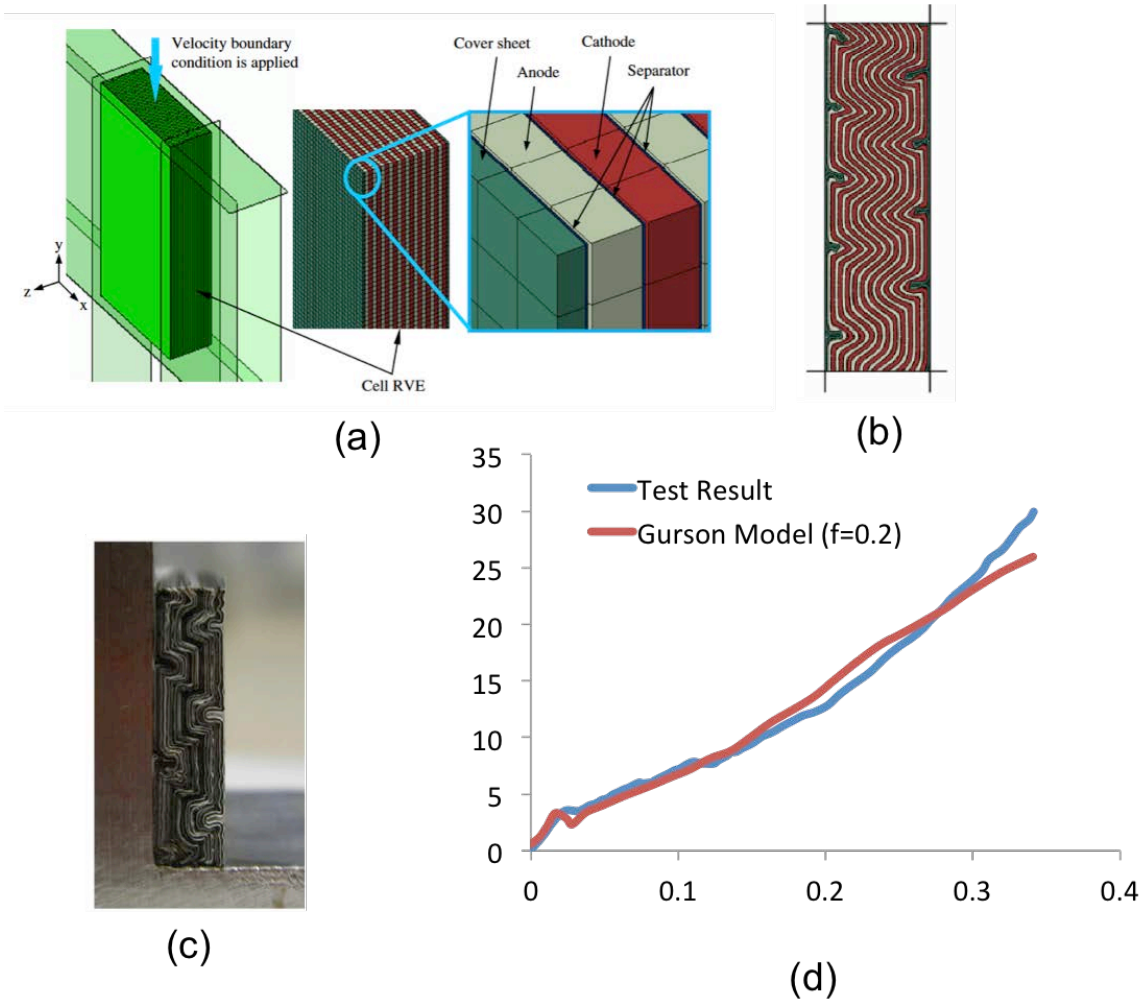

Fig. 16. In-plane compression loading (a) Geometry and boundary condition (b) Buckled configuration obtained from simulation (c) Buckled configuration obtained from test (d) Stress-strain diagram obtained from simulation and it's comparison with experiments [88].

3.2.4 GAPS AND CHALLENGES

The assumption of internal short circuit being caused by tensile failure of the separator under indentation may not hold true in all cases and is dependent on the internal configuration of the cell.

Rather formidable fracture strain in tension can be observed (about 40%) even in the weaker direction of the porous separator membrane (Fig. 7). Tensile fracture strain of the electrodes is orders of magnitude lower (Fig. 5), with the positive electrode appearing to be less ductile than the anode. This implies failure of electrodes prior to separator failure and possible rearrangement/folding of fragments, creating much more complicated scenarios for internal short circuit.

There is a tremendous gap in knowledge of mechanical properties of active electrode materials, especially as a function of state of charge and charge/discharge cycle number (age of battery). This significantly limits predictive capabilities of any models and necessitates performing a series of mechanical tests on a cell level to obtain effective load-displacement curves which are matched by modeling with homogenized material properties (crushable foam models seem to be the most commonly used). This cycle has to be done any time a new cell/module/pack is considered, since the parameters obtained by fitting the data to a specific cell may not be valid when there is a change in the type of cell or the cell geometry. Knowledge of mechanical properties of active electrode particles for the most commonly used materials would allow more accurate upscaling strategies and truly predictive computational models.

While many recent efforts have tried to model certain aspects of the behavior of the Li-ion batteries during mechanical abuse or internal short conditions, such as the electrochemical, electrical, thermal or mechanical response, coupling these various aspects to consider the response of the system in a comprehensive manner remains a challenge. There have been efforts at coupling some of the various physics, such as thermal with mechanical response, or electrochemical with thermal response. However, the large differences in the length and time scales at which these different mechanisms need to be modeled makes a truly rigorous coupling quite challenging.

Current models for the mechanical abuse of the battery, whether using a homogenized or a layer-resolved approach, do not explicitly include the strain rate effects in the mechanical response of the different materials. While this may not be very significant when the testing is done under quasi-static conditions, the strain rates under automotive crash situations are often orders of magnitude higher, and it then may become important to include the effect of high strain rates in the deformation and failure models for these materials.

4. TEST DEVELOPMENT FOR BATTERY SAFETY CHARACTERIZATION

4.1 EXPERIMENTAL RESULTS

4.1.1 DETERMINATION OF CONTACT RESISTANCE

Proper description of the exothermic reactions in the vicinity of an internal short circuit depends on the local temperature. The latter is determined from solution of the heat conduction equation (Section 2.2, Eq. (9)) with the appropriate heat source term. The heat source in the area of the internal short circuit depends on the passing current as well as short resistance. If the short is induced by local contact between the cell components, the contact resistivity needs to be known.

We have performed a set of experiments to measure the contact resistance in accordance with ASTM B539-02. The resistance of the contact between different pairs of electrodes and current collectors was measured as a function of applied pressure. The latter was applied by an MTS servohydraulic frame supplied with in-house designed insulated grips to sandwich the electrodes Fig. 17 (a). $LiNi_{0.3}Mn_{0.3}Co_{0.3}O_2$ was used as a cathode material paired with graphite anode. The results are shown in Fig. 17 (b). As can be seen the resistivity of the contact reaches an asymptote at a certain value of applied pressure. This asymptote appears to be lowest for Al-Anode pair, which often results in high energy internal short leading almost certainly to thermal runaway.

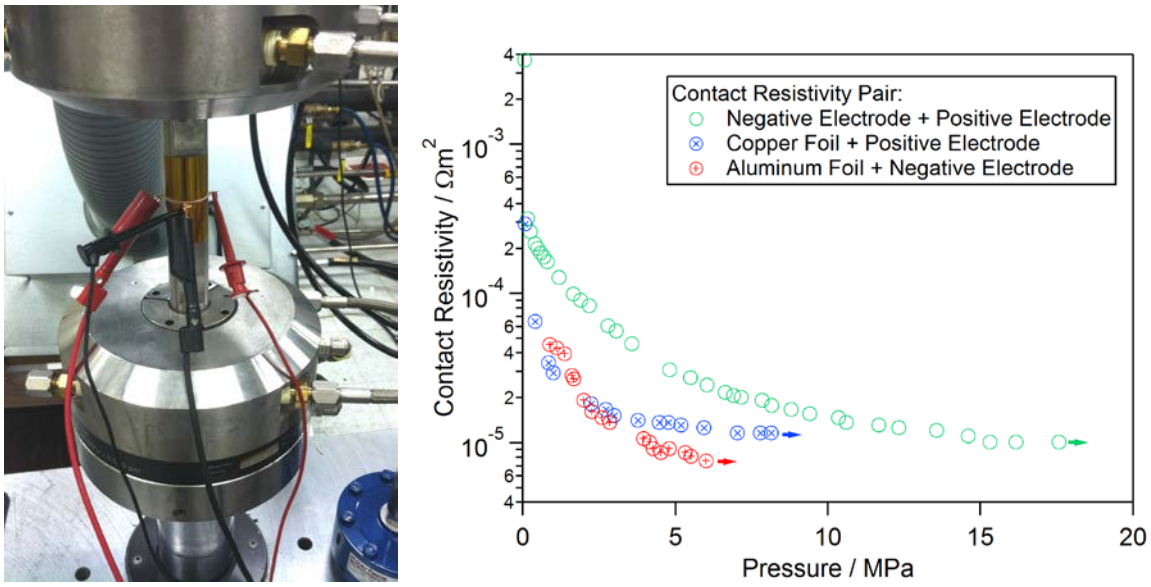

Fig. 17. Contact resistivity measurement: (a) experimental setup; (b) resistivity as a function of applied pressure

4.1.2 TEST SETUP FOR MECHANICAL ABUSE

Battery safety testing was developed at ORNL to simulate the internal short circuit of Li-ion cells. The same set up was used to simulate a high-speed impact or collision events in the current study. In order to simulate an internal short circuit event, two spherical indenters were used to create a separator failure deep inside the cell. The testing speed was very slow at 0.01" or 0.005"/min. To simulate vehicle crash conditions the failure location could be closer to the cell surface and the

testing speed has to be significantly increased. The pinch test may be replaced by a single-side indentation test to better simulate the crash.

The large format cell testing was performed at the Naval Surface Warfare Center (NSWC) facility at Carderock MD. A mechanical load frame was built at ORNL and installed at NSWC. The system components are shown in Fig. 18. A motor-driven actuator was installed on a steel frame and a load cell was used to detect the compressive force applied to Li-ion cell(s). Fig. 19 (a) and (b) are pictures of the actual setup at NSWC. Two stainless steel spheres with connecting rods are used for the pinch tests. A load cell was used to measure actual force in the system. The testing system is controlled through LabView software, which also handles the data acquisition (DAQ). Thermal insulations were used to protect the components from overheating in an event of thermal runaway. The test chamber at NSWC is a reinforced steel structure with ventilation. All the controls and monitoring were carried outside using two computers, as shown in Fig. 19(b).

A FLIR A325 infrared camera was used to monitor surface temperatures of the cell during and after the short circuit event. It is a micro-bolometer focal place array (FPA) camera with 320 x 160 pixel format. The camera can operate at 60 Hz and the temperature resolution is 0.15 Kelvin. A pair of neutral density filters is available inside the camera for high temperature imaging. For this study, the IR camera is set at room temperature to 150˚C range.

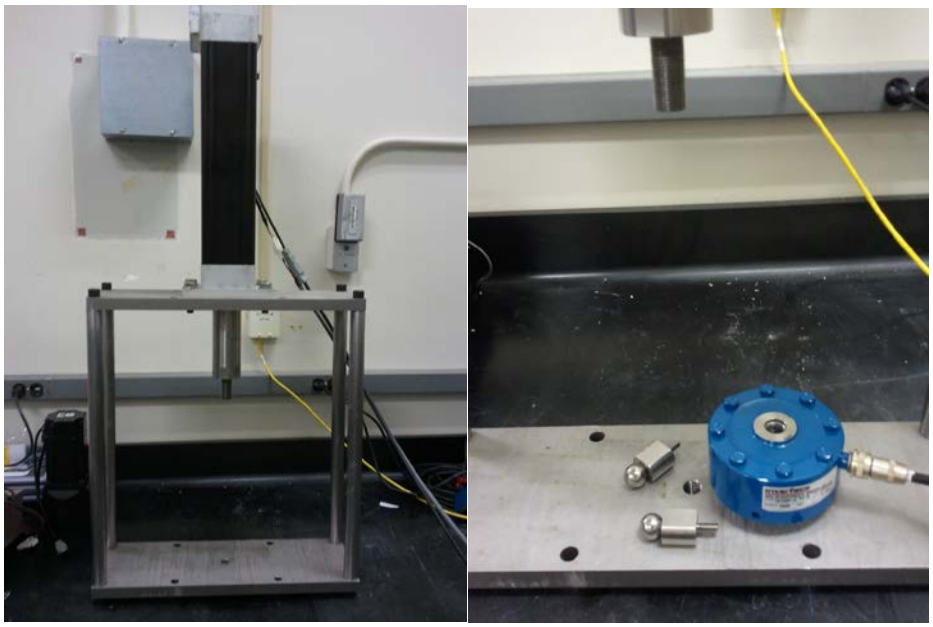

(a) (b)

Fig. 18. Load frame with (a) Motor-driven actuator and (b) load cell

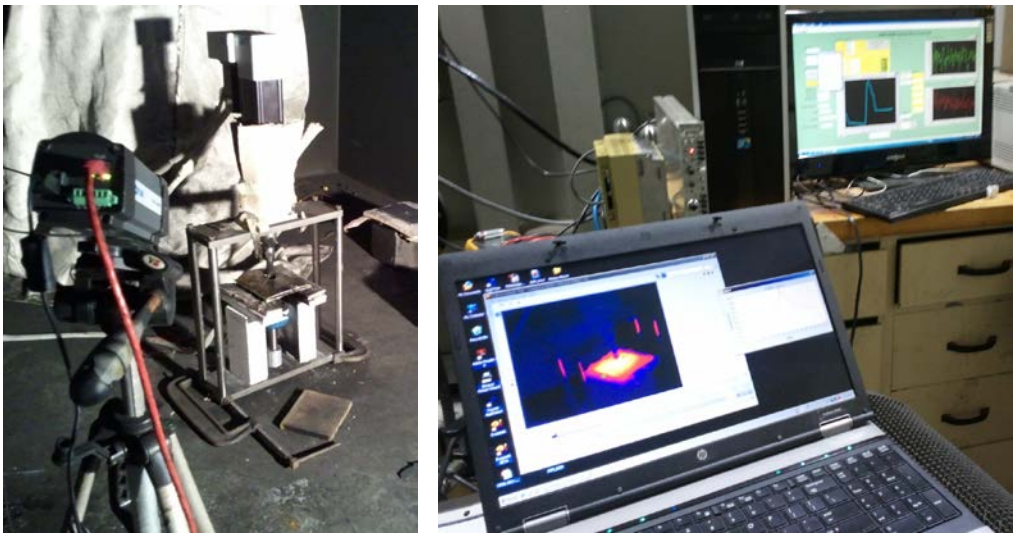

(a) (b)

Fig. 19. (a) Actual setup at NSWC and (b) experimental controls and monitoring outside the test chamber

The first system test was to evaluate the speed limit of the load frame. Under normal set up, the system is capable of moving at 1-2 in/min without any delays and overshooting the targeted displacement set point. However, when the speed is increased two main concerns must be addressed:

1) The data acquisition speed
2) How to effectively stop of the test

We found it is important to only move the specified distance in the current test rather than reading and reacting to a voltage feedback because the total cell thickness is only about 6 mm and some cell layers are only 12-20 microns. A slight overshoot will cause damage in additional layers. It was found the normal Tension, Compression, Stop buttons in the software did have enough response time to effectively stop the test at higher speeds. During the initial visit to NSWC, the testing system was modified as follows:

1) The data acquisition speed was increased from 2000 to 5000 points per second, which is sufficient to record data from each channel without any delay.
2) A “Move to” function was added in the software to move to the specific position at the predetermined speed.
3) An encoder threshold was added to ensure the test does not go over the total thickness of the cell causing collision of the spheres.

Fig. 20 is a screen shot of the modified software window. The maximum speed achieved was 12 in/min.

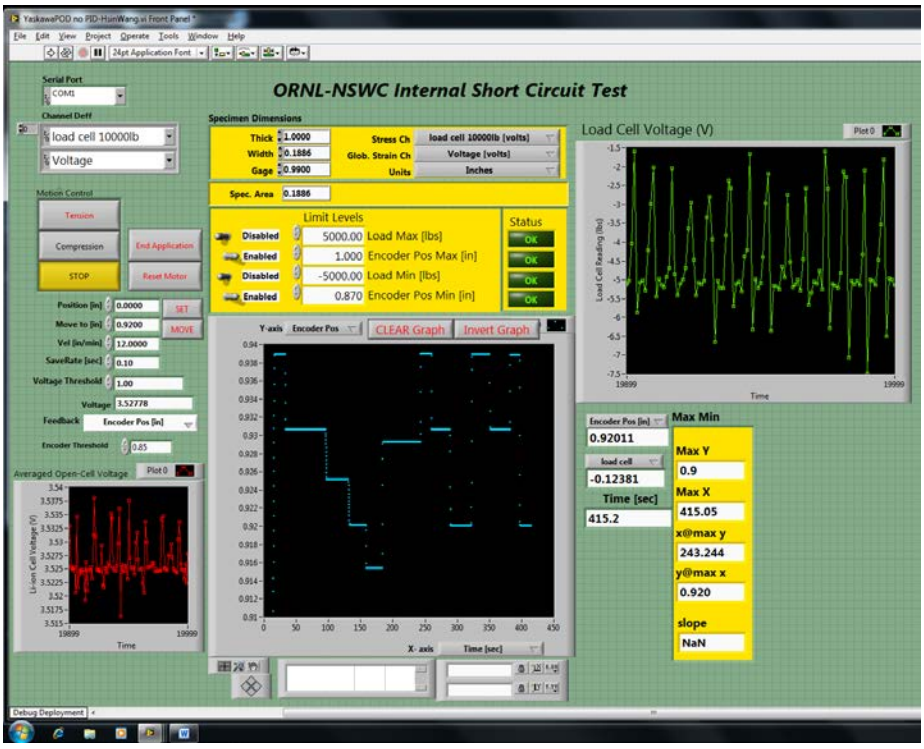

Fig. 20. Screenshot of the modified LabView interface at NSWC

For the current project, three testing speeds were selected and are shown in Table 15. This was designed to match the testing speeds of battery pack crash simulations conducted in other related NHTSA projects.

Table 15. Test Speeds for the current study

Speed	inch/min	mm/sec
Low	0.25	0.105
Medium	7	2.96333
High	12	5.08

4.1.3 PINCH TESTING OF SINGLE CELLS

High speed pinch tests were conducted at NSWC in October 2014. A total of seventy 25 Ah NMC cells were purchased from a vendor. The cells were at shipping voltage with State of Charge (SOC) of 10%.

Cell 0: (ID: DD220 1690) 0.25 in/min: first run set to move 0.12 in (about 3mm), the load reached 90-95 pounds. No short circuit was observed. The spheres were moved another 0.04 in with no short circuit. In the 3rd run, using the voltage as feedback, the cell shorted and voltage rebounded to 3.4V followed by a slow discharge. IR camera showed a small gas release and followed by heating to 90-95˚C. IR camera was running at 4Hz.

After setting the initial test conditions, the pinch tests were carried out using the parameters in Table 15 for test speeds. At least three cells were tested for each condition.

Test procedures:

1. Check cell voltage (should be around 3.5V)
2. Place the cell in test frame and lower the top 1”sphere close to the cell surface
3. Get LabView software and IR camera ready assigning proper file paths and names
4. Record the images and start the run
5. Use” Move To” function to compress the cell 5 mm and then hold
6. Voltage feedback is ON all the time. If the voltage dropped 0.1V, the short is detected, the load cell will retract at 1”/min
7. Check the cell voltage and temperature via the IR camera

Encoder setup: Initial contact point: 0.7740”, Move to: 0.6025”

Total displacement: 0.1715” or 4.356 mm (about 70% of total cell thickness)

A total of 10 cells were tested. All the low speed tests (cells 1, 4, 7) failed when the set displacement was reached. Three higher speed tests (cells 5, 6, 8) did not fail and an additional distance had to be moved to induce short circuit. The following are cell ID and test conditions:

Cell 1: (ID: DD205 0871): 0.25”/min

Results: reached 0.6025” and after 1-2 second, short circuit occurred (local runaway, no fire)

Cell 2: (ID: DD206 1455): 7”/min

Cell 3: (ID: DD205 1145): 12”/min

Cell 4: (ID: DD205 1254): 0.25”/min

Cell 5: (ID: DD205 1833): 7”/min: moved a few more steps to 0.590” after 100 seconds.

Cell 6: (ID: DD203 0316): 12”/min: moved to 0.600” after 60 seconds

Cell 7: (ID: DD205 0873): 0.25”/min

Cell 8: (ID: DD220 1489): 7”/min: move d to: 0.6025” (missed IR images)

Cell 9: (ID: DD205 1143): 12”/min

Cell 10: (ID: DD208 1901): Repeat 7”/min

Fig. 21 is a screenshot of a test. The main screen showed the voltage drop and recovery of the cell. During the test, the main screen can be changed to view displacement, load and voltage. Two smaller screens are used to show live updates of the cell voltage and load cell readings.

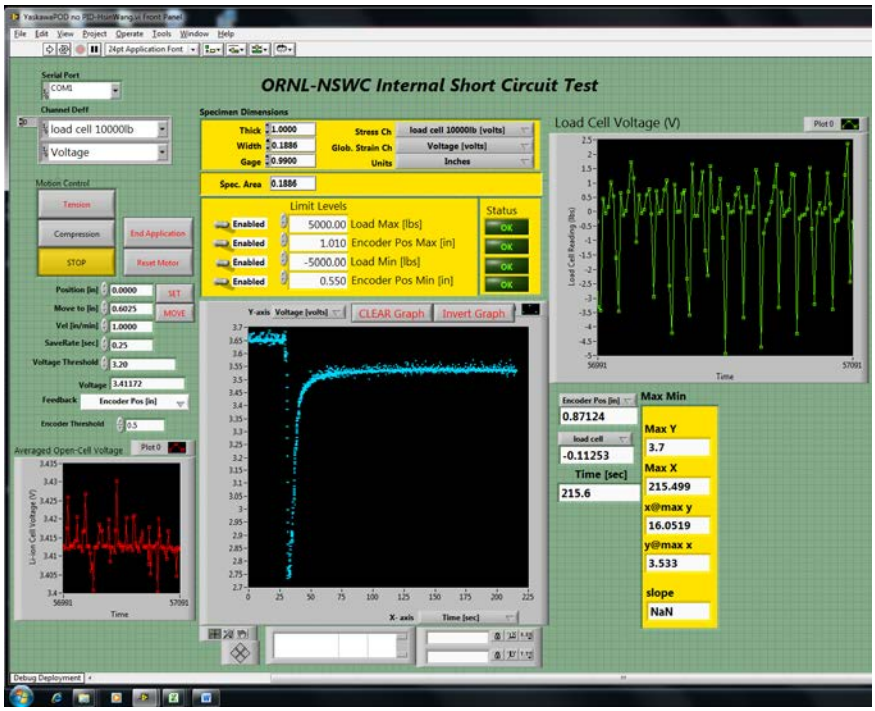

Fig. 21. Screenshot of a pinch test

The data were processed with displacement, load and voltage plotted against time. A typical cell after the pinch test is shown in Fig. 22. Both pouch surfaces showed cracking under the indenters after 70% compression. However, no evidence of the spread of the thermal runaway was observed.

(a) (b)

Fig. 22. Surfaces (a) bottom, and (b) top of 25 Ahr NMC cells after the tests

Test results of cells at low speed are shown in the following Fig. 23 - Fig. 25. All three cells failed at the preset 70% total thickness displacement values, although a couple of the cells had 5-10 seconds delay time before the short circuit. The load was in holding mode before the voltage drop.

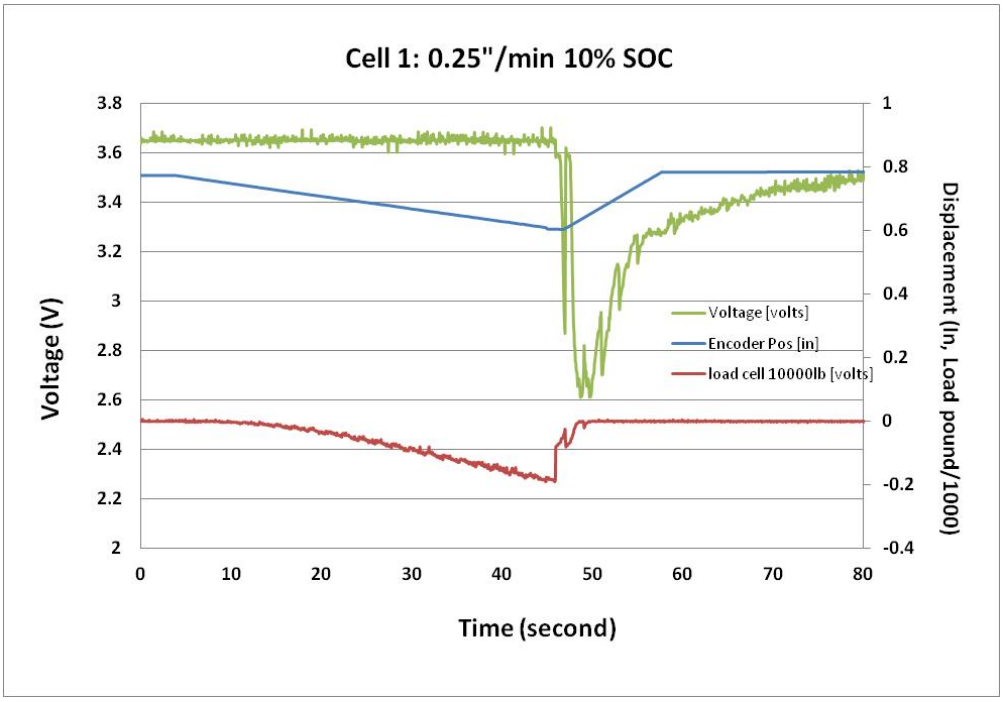

Fig. 23. Voltage, Displacement and Load vs Time plots of Cell #1 at 0.25"/min

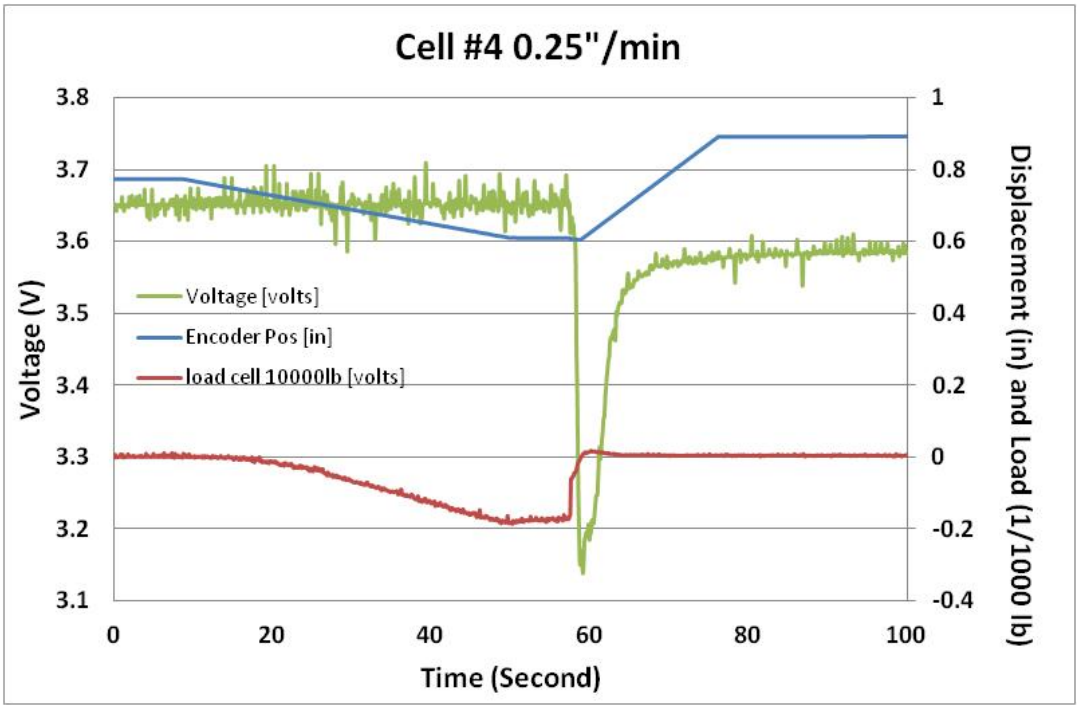

Fig. 24. Voltage, Displacement and Load vs Time plots of Cell #4 at 0.25"/min

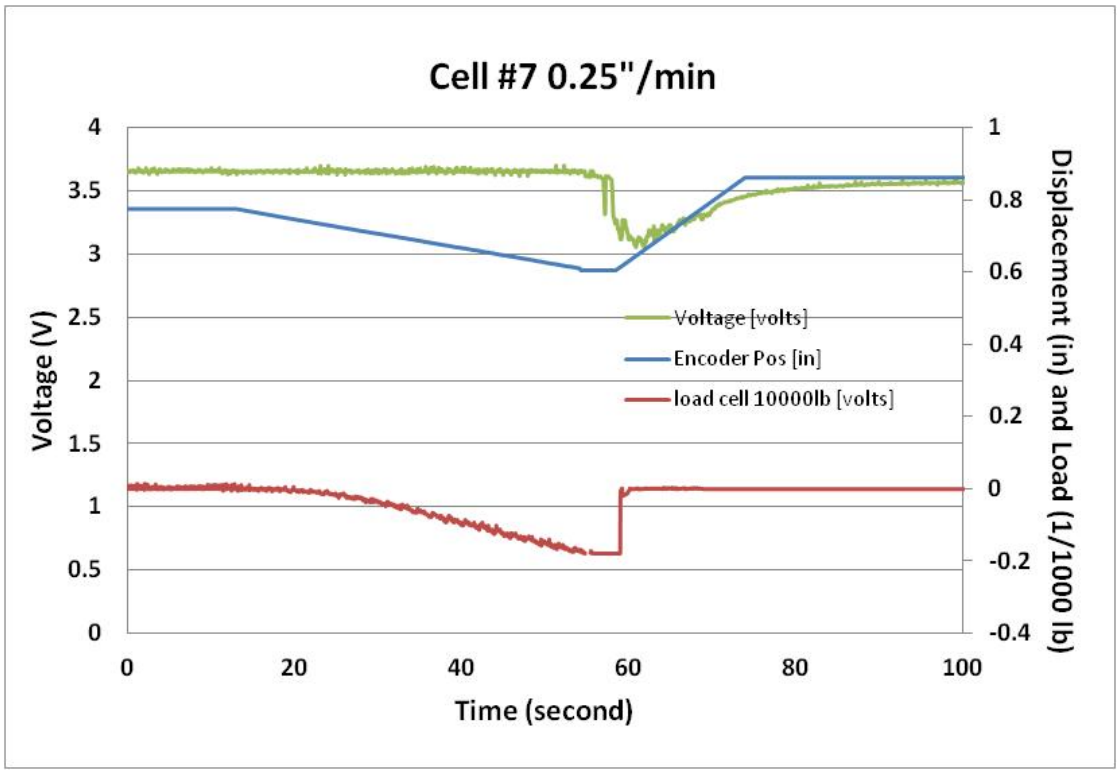

Fig. 25. Voltage, Displacement and Load vs Time plots of Cell #7 at 0.25"/min

Test results of cells at medium speed are shown in the following Fig. 26 - Fig. 29. Three out of four cells failed at the set 70% displacement values, all of them had 5-50 seconds delay time. One cell needed an additional step to induce short circuit.

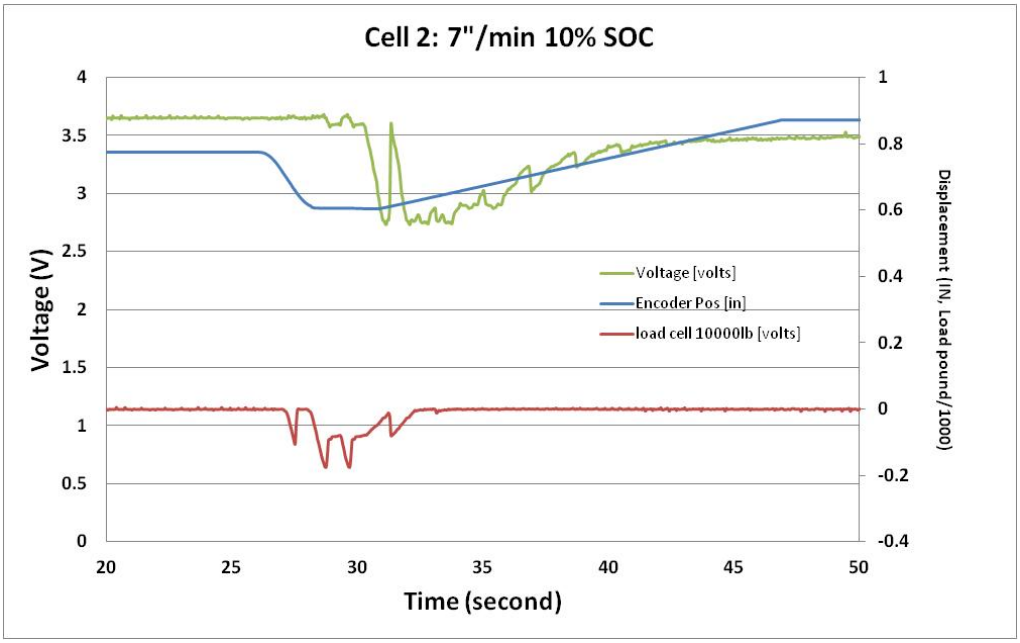

Fig. 26. Voltage, Displacement and Load vs Time plots of Cell #2 at 7"/min.

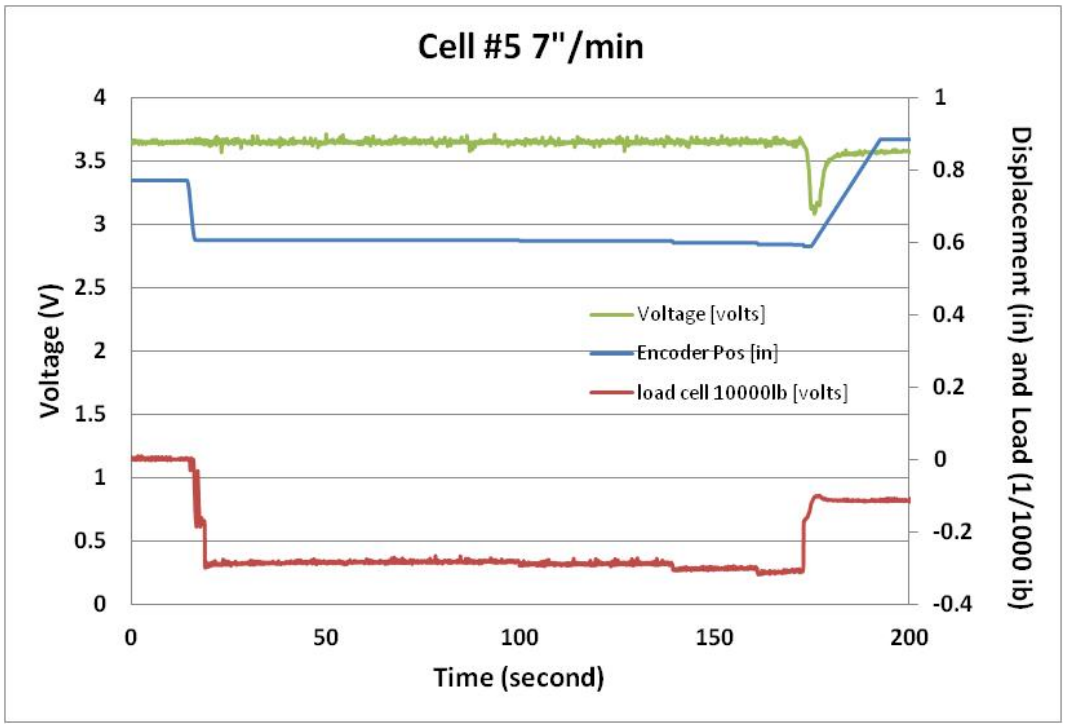

Fig. 27. Voltage, Displacement and Load vs Time plots of Cell #5 at 7"/min

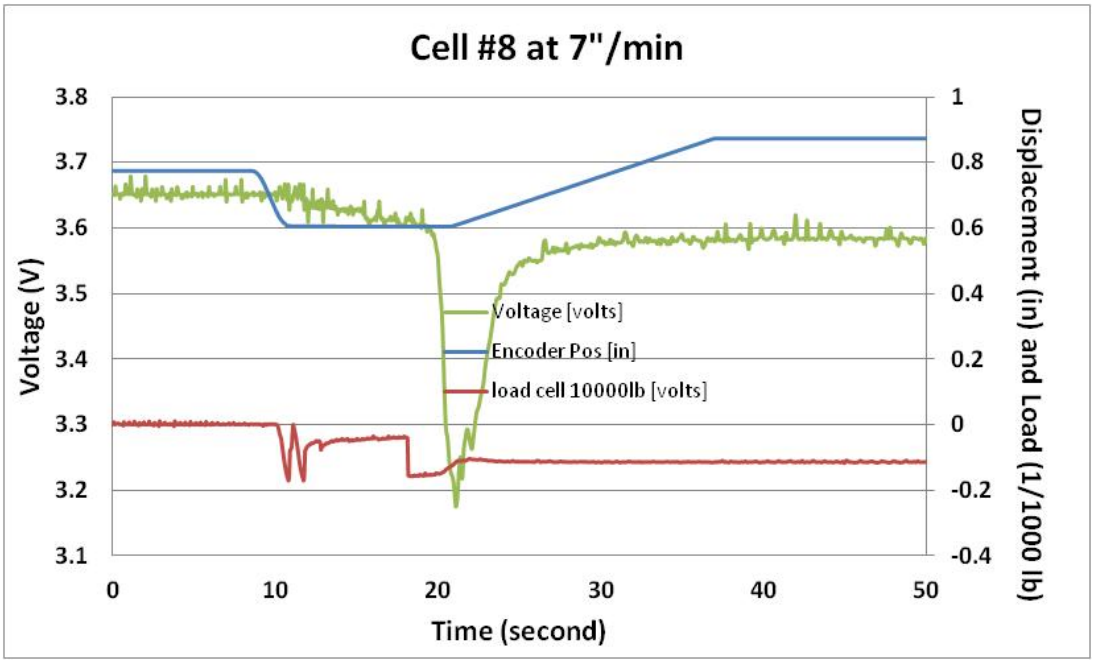

Fig. 28. Voltage, Displacement and Load vs Time plots of Cell #8 at 7"/min

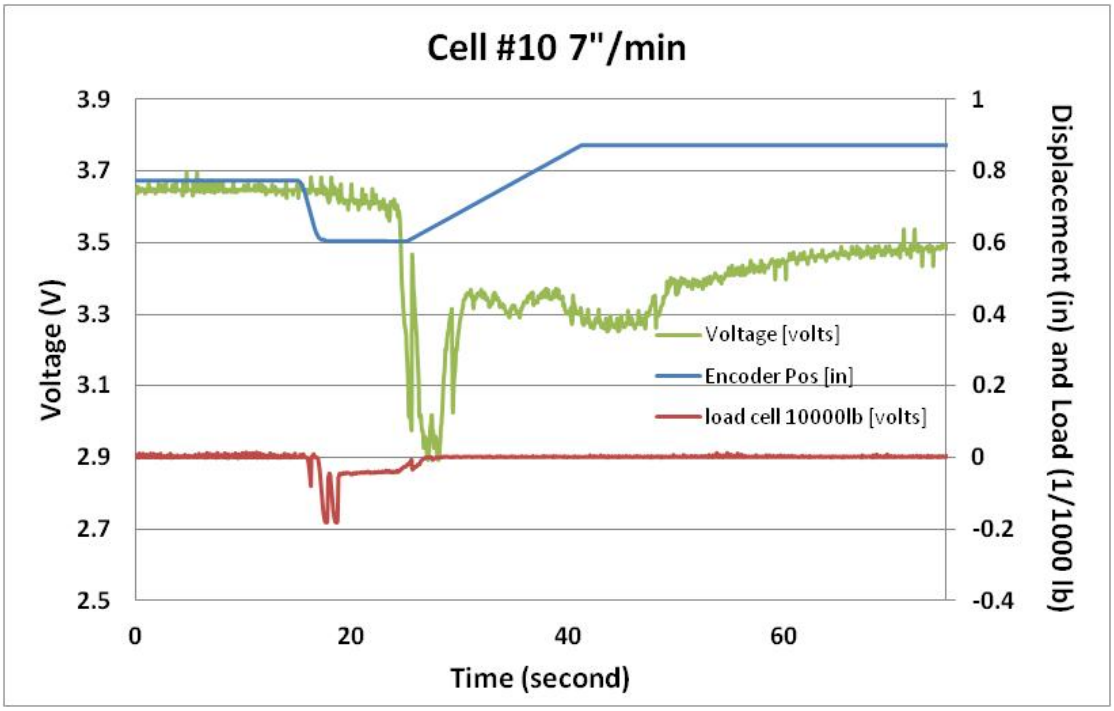

Fig. 29. Voltage, Displacement and Load vs Time plots of Cell #10 at 7"/min

Test results of cells at high speed are shown in the following Fig. 30 - Fig. 32. All three cells failed at the set 70% displacement values, all of them had 10-20 seconds delay time. One cell did not fail after 2 minutes and a couple additional steps were used to induce short circuit.

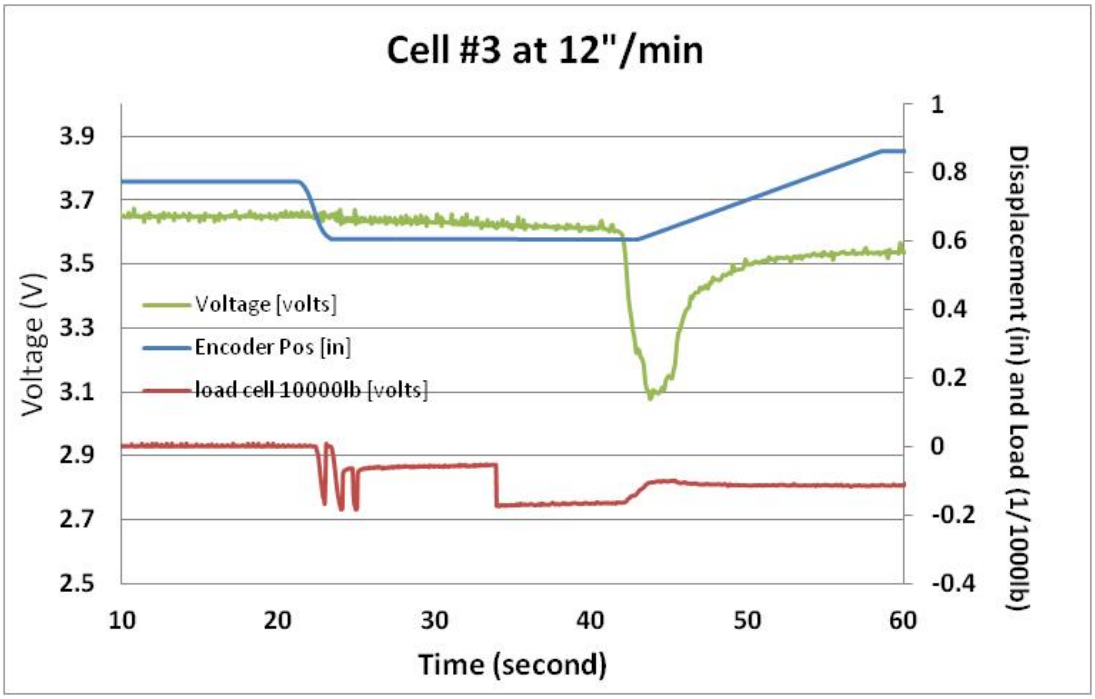

Fig. 30. Voltage, Displacement and Load vs Time plots of Cell #3 at 12"/min

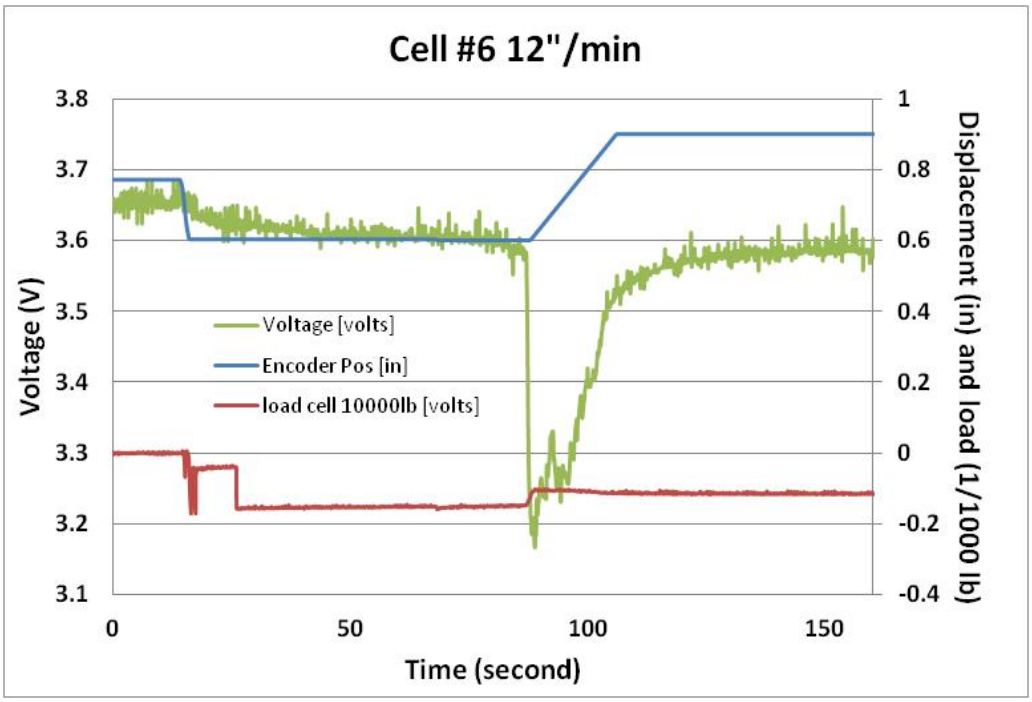

Fig. 31. Voltage, Displacement and Load vs Time plots of Cell #6 at 12"/min

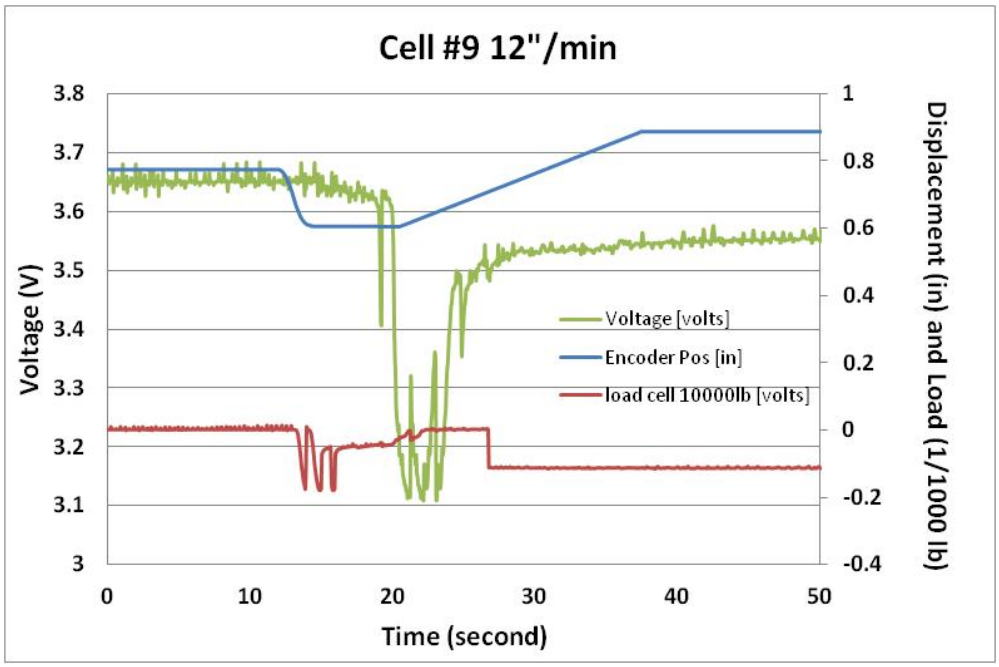

Fig. 32. Voltage, Displacement and Load vs Time plots of Cell #9 at 12"/min

Load values at medium and high speeds showed rapid changes. It was not confirmed if the changes were from the cell itself or some measurement responses at high speed. At 7 in/min and 12 in/min, the total time to move 4.356 mm took about 1 second. The movement of each layer in such a short time is unknown and the responses of the load cell also need further verification. It is clear that at higher speeds the failure is delayed. In a few cases, failure did not occur and additional compression was needed to induce short circuit. Both modeling and experimental efforts are needed to better understand the cell deformation under high speed compression.

4.1.4 INFRARED IMAGING OF CELLS

A FLIR A325 IR camera was placed in the test chamber recording the cell surface temperature during the test. Fig. 33 is the temperature of the cell #0 during a continuous compression at 0.25"/min.

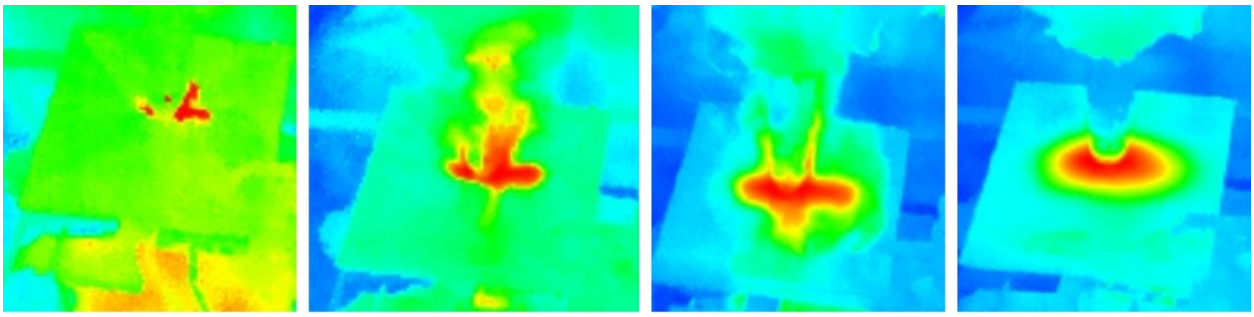

0.25 sec 1 sec 5 sec 10 sec

Fig. 33. Cell #0 at 0.25"/min constant speed. IR images at 0.25Sec, 1 sec, 5 sec and 10 sec.

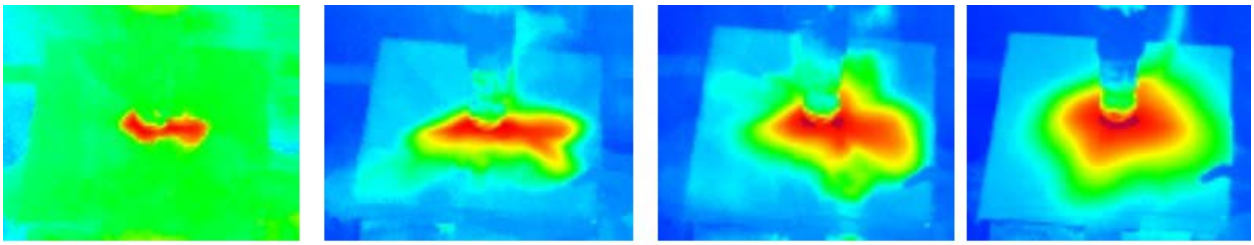

Cell #1: 1 sec 3 sec 5 sec 20 sec

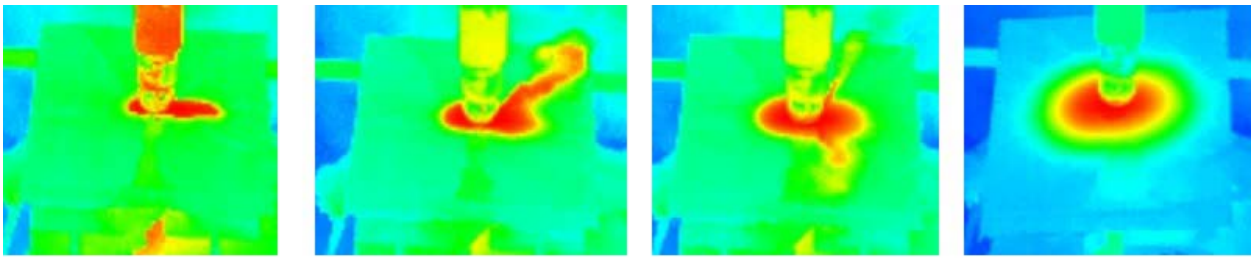

Cell #4: 1 sec 3 sec 5 sec 20 sec

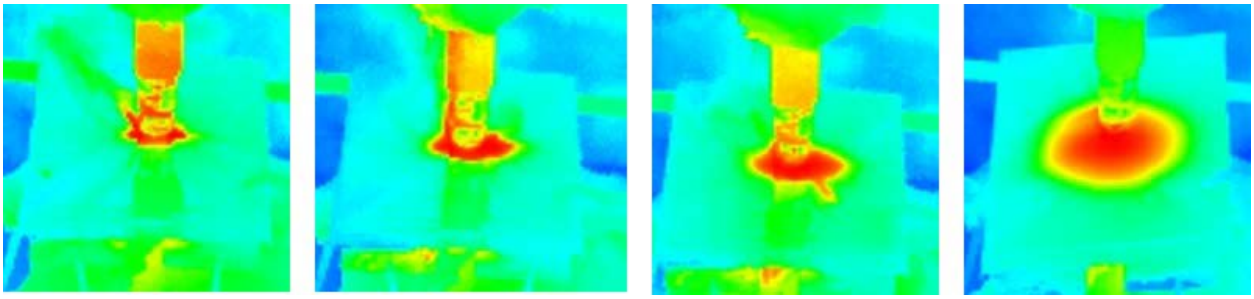

Cell #7: 1 sec 3 sec 5 sec 20 sec

Fig. 34. Cells at 0.25"/min low speed. IR images at 1 Sec, 3 sec, 5 sec and 20 sec.

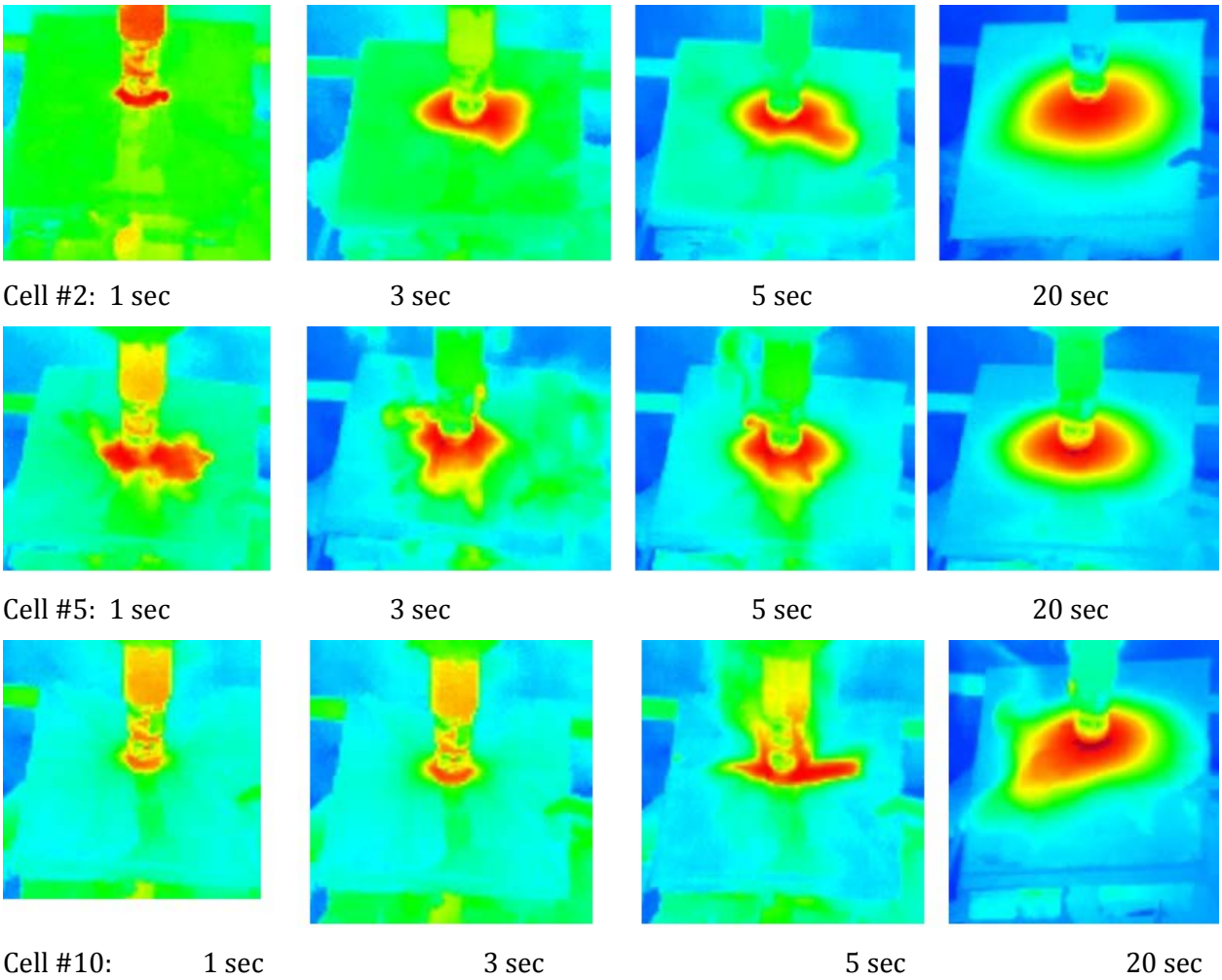

Fig. 35. Cells at 7"/min medium speed. IR images at 1 Sec, 3 sec, 5 sec and 20 sec.

General observations from the IR images (Fig. 33 - Fig. 36) are:

- All cells went to "local" thermal runaway:
- "Fingers" shooting out at high speed
- Pouch cracked with brief gas release
- Cell voltage rebounded
- Whole cell thermal runaway did not happen
- Slow discharge about 30-60 minutes followed

Besides imaging the surface for temperature maps, the temperature evolution as a function of time was also studied. In Fig. 37 - Fig. 39, the temperatures under the top indenter were tracked as a function of time. In most cases, the surface temperature increased to 80-90˚C and in some case the temperatures reached 130-140˚C. The local temperature reached thermal runaway critical point. However, the event did not spread throughout the cell. By monitoring the voltage of the cell, recovery was observed after the release of the compressive pressure, indicating that part of the cell was still functioning.

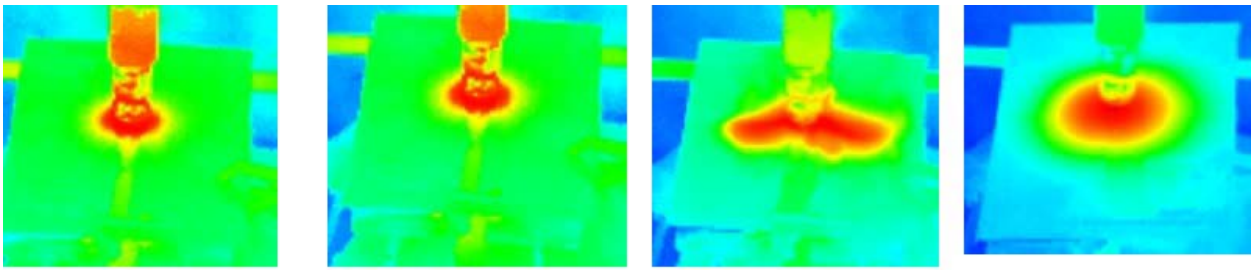

Cell #3: 1 sec 3 sec 5 sec 20 sec

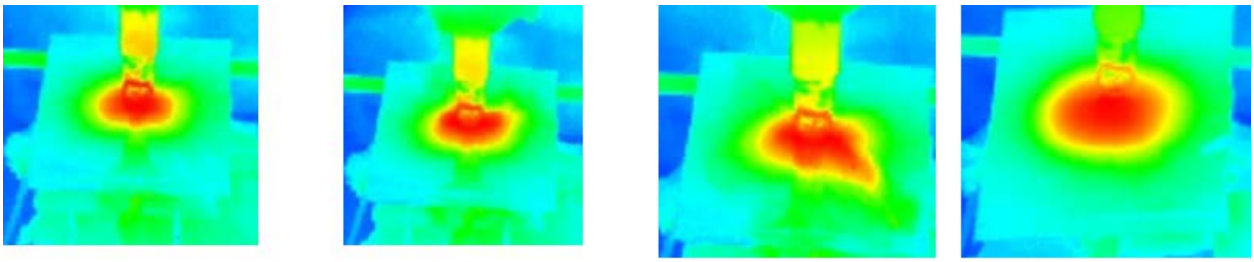

Cell #6: 1 sec 3 sec 5 sec 20 sec

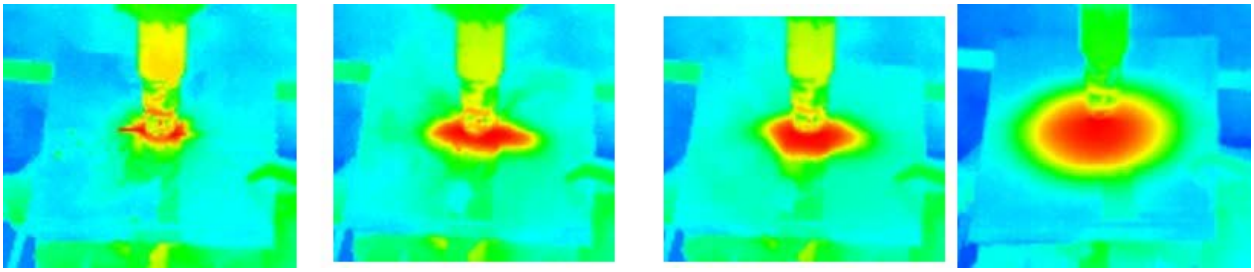

Cell #9: 1 sec 3 sec 5 sec 20 sec

Fig. 36. Cells at 12"/min high speed. IR images at 1 Sec, 3 sec, 5 sec and 20 sec.

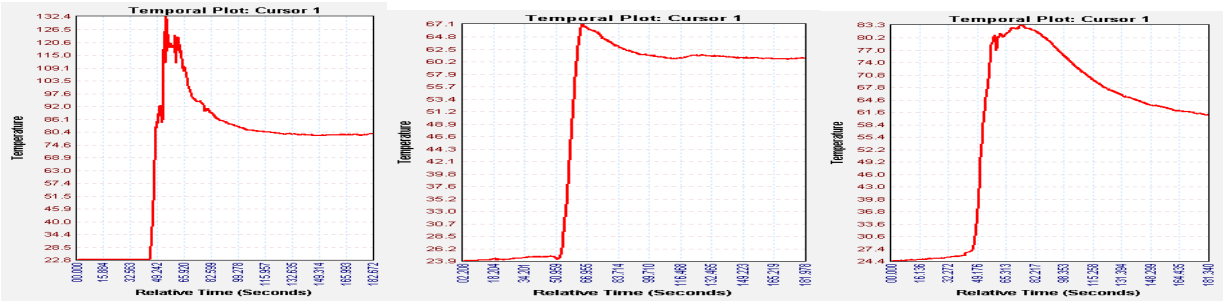

Cell #1 Cell #4 Cell #7

Fig. 37. Temperature vs. Time plots under the indenter at 0.25"/min.

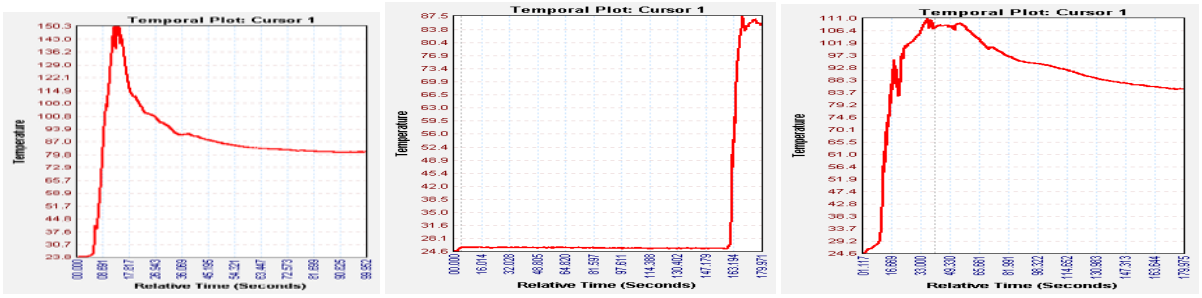

Cell #2 Cell #5 Cell #10

Fig. 38. Temperature vs. Time plots under the indenter at 7"/min.

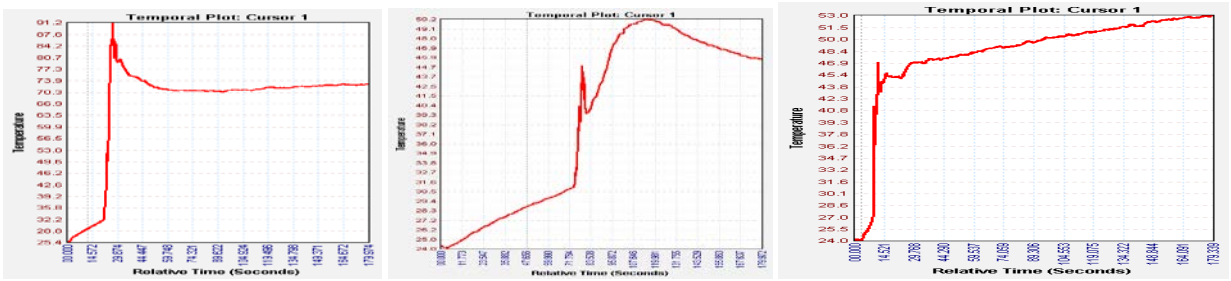

Cell #3 Cell #6 Cell #9

Fig. 39. Temperature vs. Time plots under the indenter at 12"/min.

4.1.5 PINCH TESTING OF 3P CELLS

After the single cell testing, the tests moved to a stack of three 25 Ahr cells connected in parallel. The three cells were stacked and wrapped by tape at both ends. No backing materials or cooling plates were used between the cells. Using the same test setup at NSWC, the 3P tests were carried out in November, 2014. The images of the 3P stack before and after the test are shown in Fig. 40. The cells were subjected to the pinch test using 1" diameter spheres.

Fig. 40. 3P string before and after the pinch test

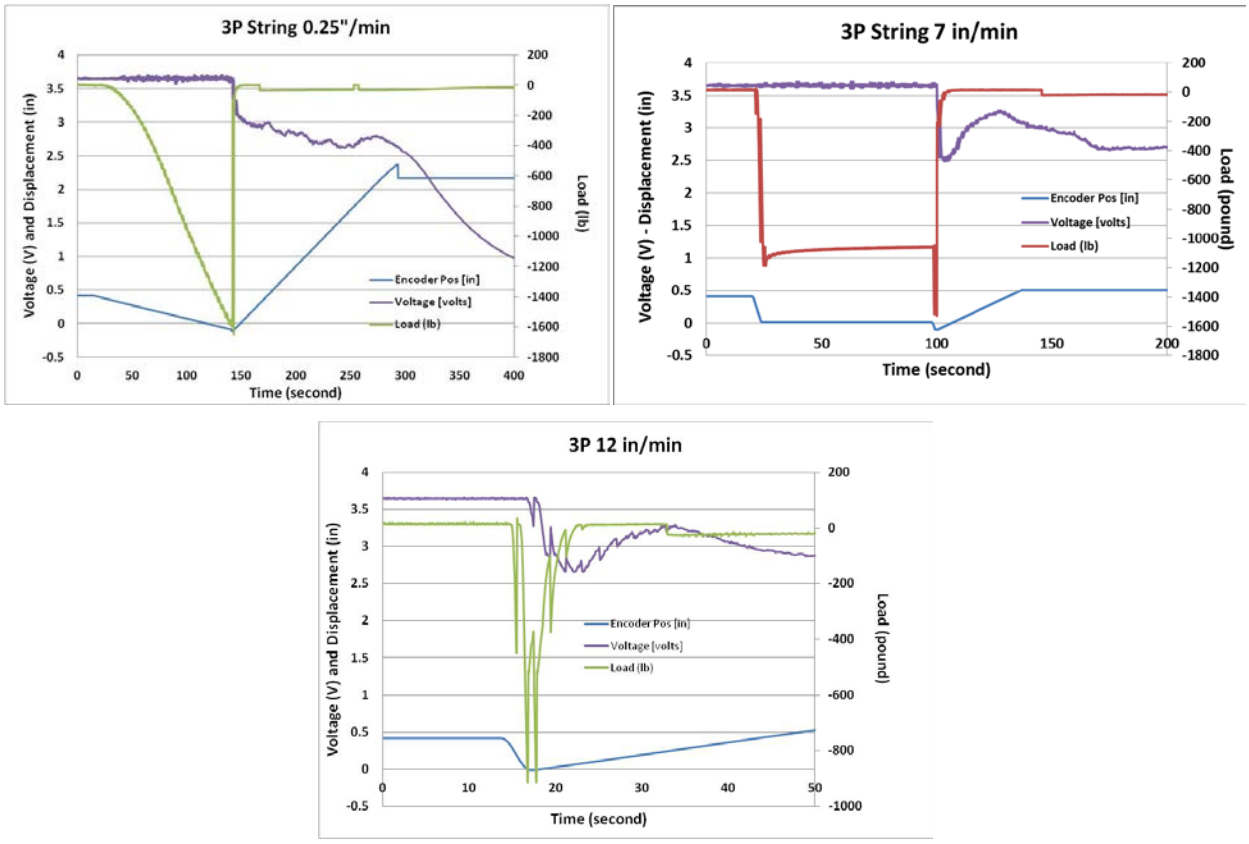

Fig. 41. Voltage, Displacement and Load vs. Time plots of 3P strings tests

Fig. 41 shows recorded experimental data of the 3P strings during pinch tests. One set of samples were tested using the low, medium and high speeds. The overall distance moved to induce short circuit was 60% of the total thickness of the three cells. The failure load was around 1600 pounds compressive force. The 7”/min test did not induce short circuit right away and a second step was needed to induce short circuit. In the 12”/min test, the load cell values were noisy and the final force was lower than the previous two speeds.

In all three tests, the cell voltage continued to drop after the short circuit. Discharge from all three cells through the short circuit location was observed. The 3P discharge is equivalent to the single cell discharge at higher SOC. At 10% SOC, the combined capacity was still not enough to cause the whole cell thermal runaway.

Infrared images and cell surface temperatures were recorded and shown in Fig. 42 - Fig. 44. At 0.25”/min, the cell temperature reached 102˚C under the indenter but 122˚C near the edge. The later heating was delayed about 2 minutes.

At higher speeds, extra heating near the electrodes were observed due to cell-to-cell discharge. The temperatures under the indenter were much higher, passing the maximum set point of the IR camera, 150˚C. The temperature rise and localized thermal runaway were more severe than for single cells.

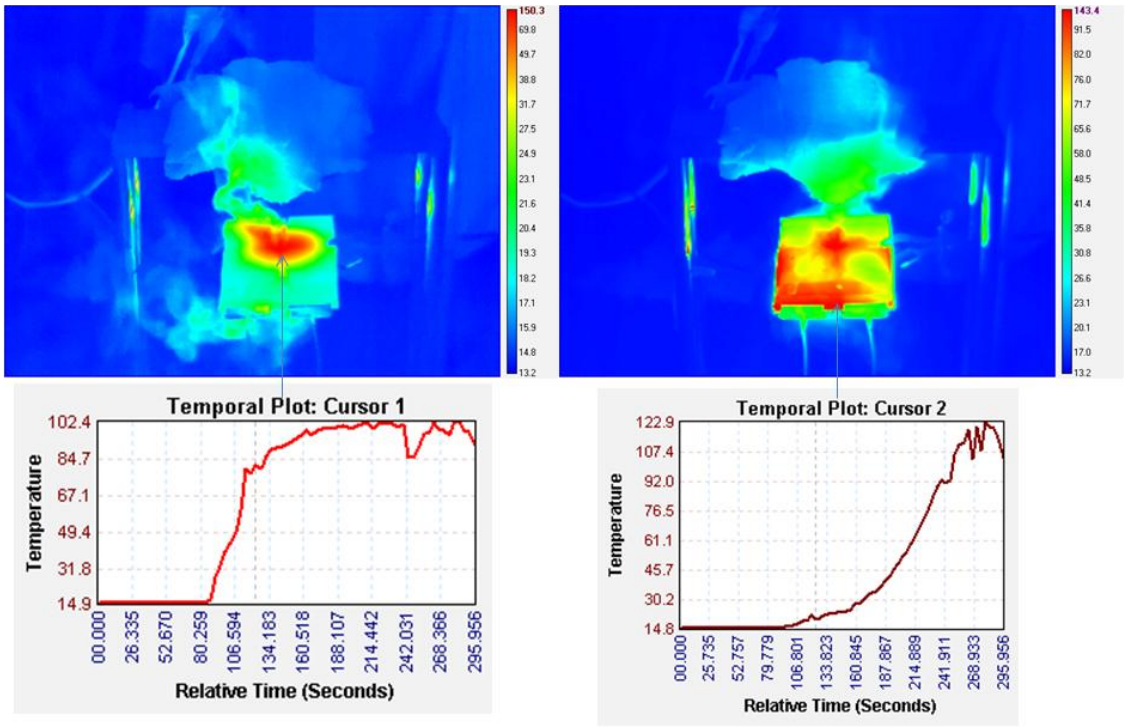

Fig. 42. IR images and temperature time profiles of the two points on the cell surface for 3P pinch test at 0.25”/min

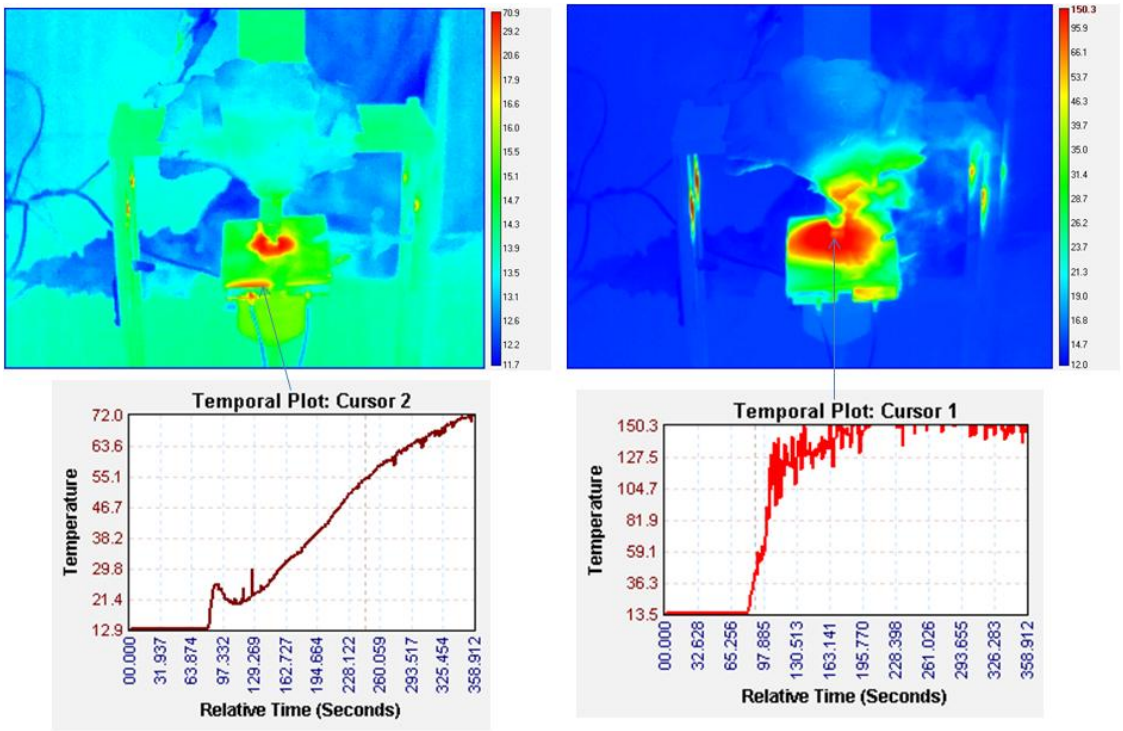

Fig. 43. IR images and temperature time profiles of the two points on the cell surface for 3P pinch test at 7”/min

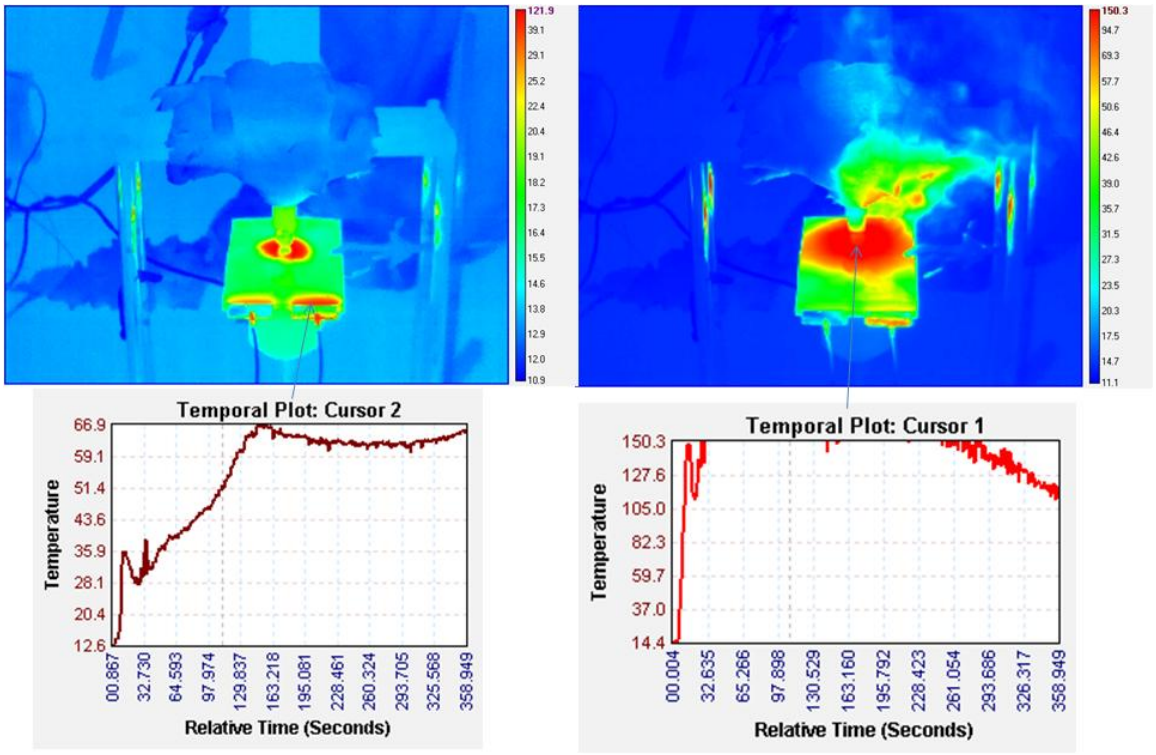

Fig. 44. IR images and temperature time profiles of the two points on the cell surface for 3P pinch test at 12"/min

4.1.6 SINGLE-SIDE INDENTATION OF 3P STRINGS

It was likely that some small misalignment was developed during the last 12"/min test. The subsequent 0.25"/min test on the 3P string was not successful. The cell stack started to slip. It was decided to switch to another configuration: Singe indenter (1" diameter) on 3P string on a flat plate as shown in Fig. 45.

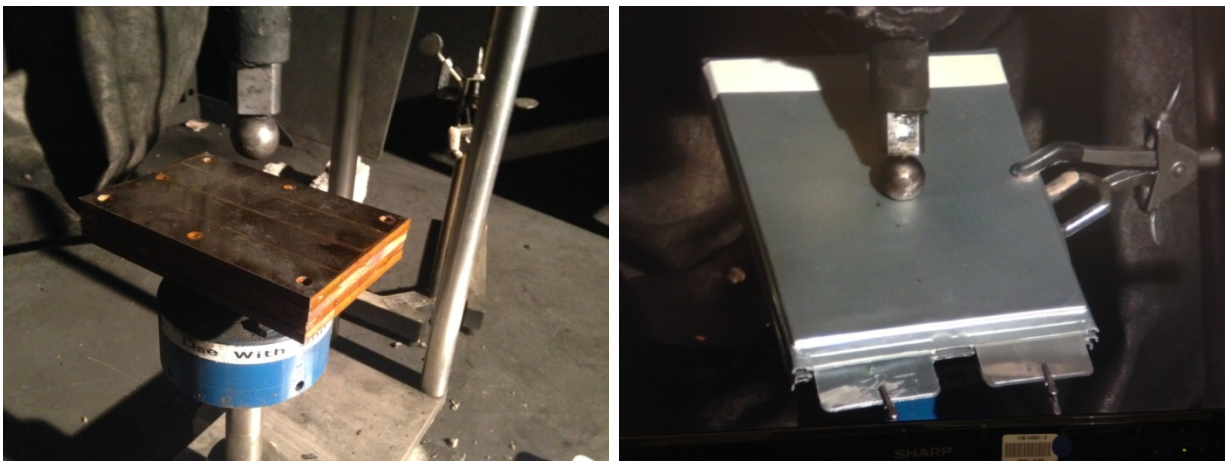

Fig. 45. Setup for single side indentation of 3P string on steel plates

The single side indentation using 1" diameter required much more load to induce the short circuit. In fact, multiple attempts reached the 2000 pound limit of the actuator and the short circuit did note occur. The final solution was to use a ½" diamater indenter shown in Fig. 46. The recorded data are shown in Fig. 47. The three tests with 1" diameter indenter all reached the actuator limit of

2000 pounds and could not cause the short circuit. After switching to the ½" diameter indenter, the short circuit was observed at 700 pounds.

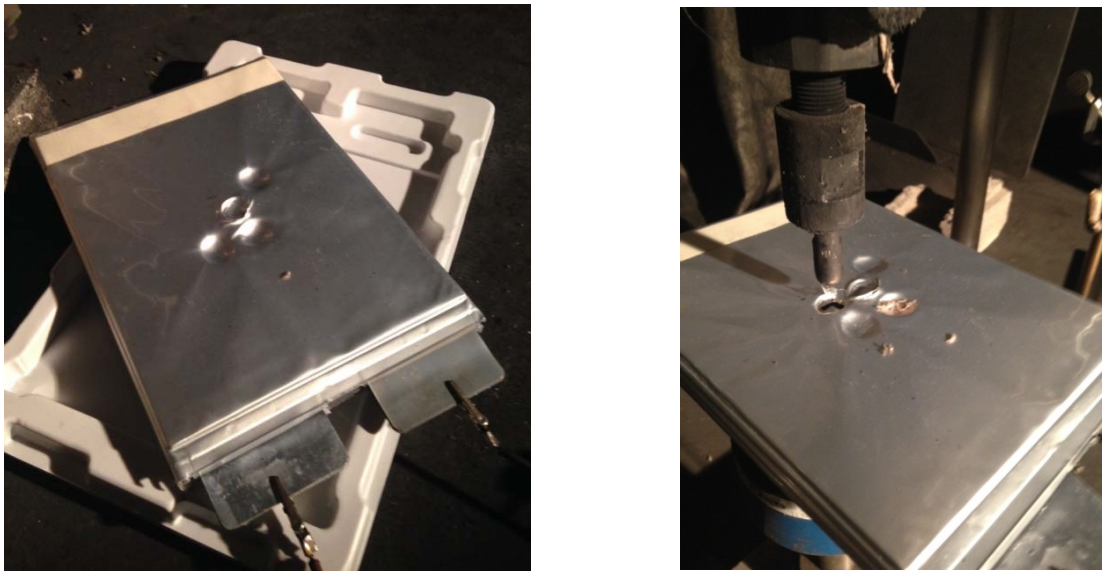

Fig. 46. 3P string on steel plates 1" diamater indentation vs. ½" diameter indentation.

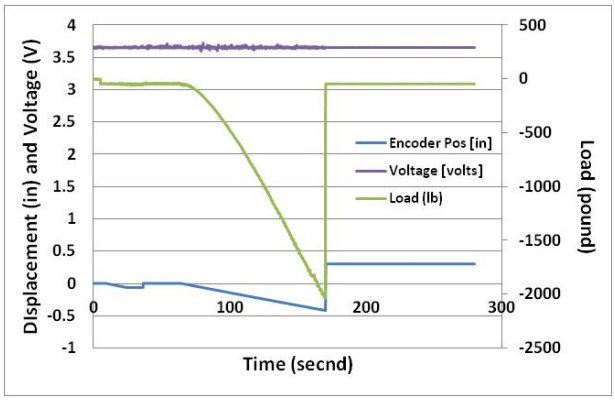

1" Test 1

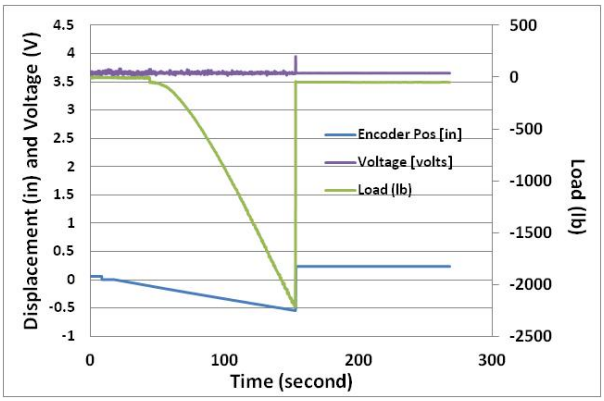

1" Test 2

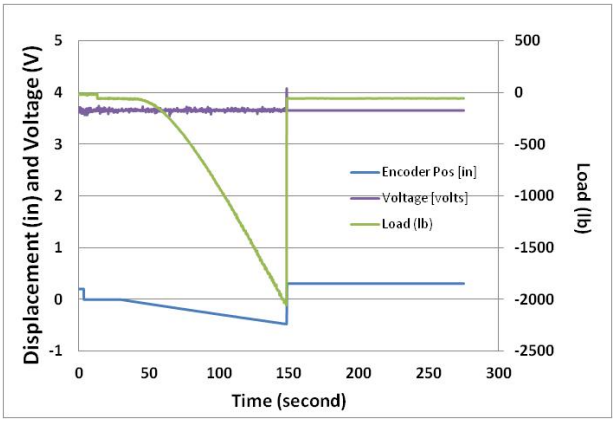

1" Test 3

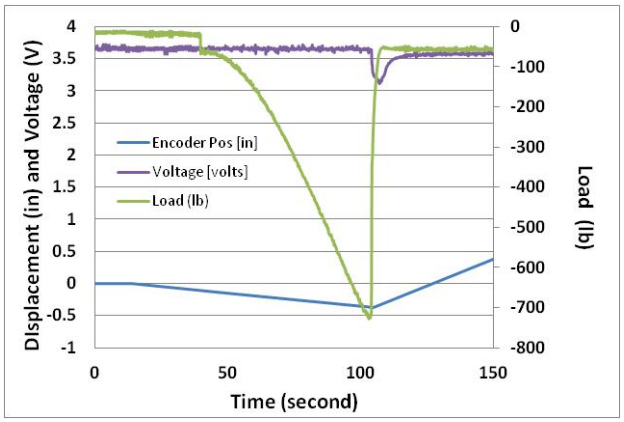

½" Test 1

Fig. 47. Voltage, Displacement, Load vs. Time plots of 3P string on flat plate.

4.1.7 SINGLE-SIDE INDENTATION OF SINGLE CELLS

After the 3P string on plate tests, it was decided the more effective test would be testing single cells on a flat plate using ½" and 1" diameter indenters. The original pinch test was designed to induce short circuit deep inside the cell to mimic internal short circuit. The actual crash simulation of the battery pack or module is closer to the single-side indentation. In this case, the top cell always fails first making it wasteful to test 3P strings. The bottom two cells are acting as backing materials only providing necessary compression of the stack.

The first set of tests was ½" diameter indenters on single cells using the same three test speeds. Multiple cells were tested at each speed and IR images were recorded as well. Fig. 48 -Fig. 50 show the Voltage, Displacement and Load vs. Time plots of these tests. For the slower speed (0.25"/min) all four test results are plotted in the same figure. The displacement values were all the same and all four cells failed at 600 pounds of force. The slopes of the load curves are not exactly the same and the final voltage responses were also varied. At higher speeds, 7"/min and 12/"/min, the load of failure became smaller, although the displacement values were the same. Noise in the load signal was observed in the 12"/min test.

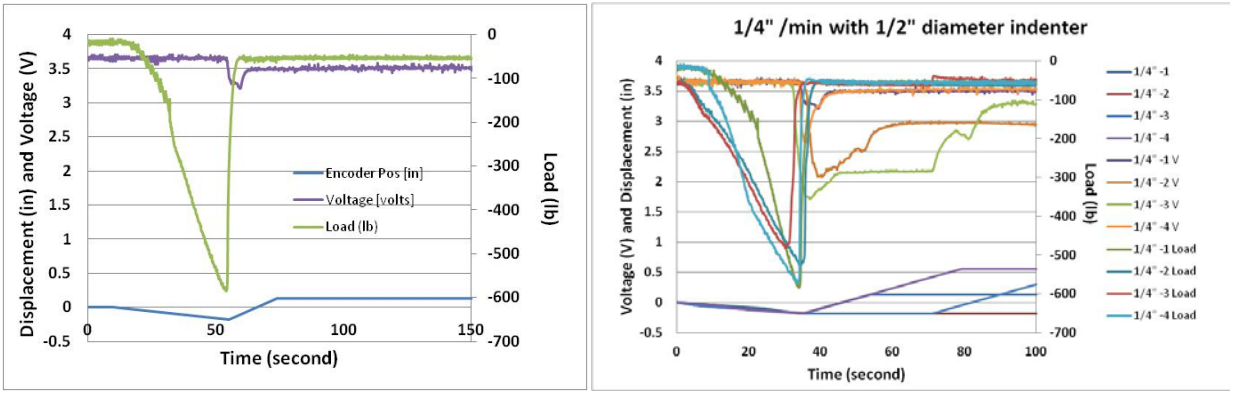

Fig. 48. Voltage, Displacement, Load vs. Time plots of single-side indentation at 0.25"/min

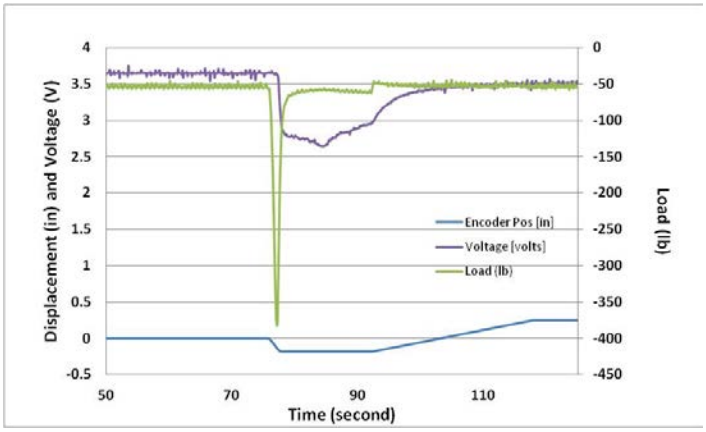

Fig. 49. Voltage, Displacement, Load vs. Time plots of single-side indentation at 7"/min

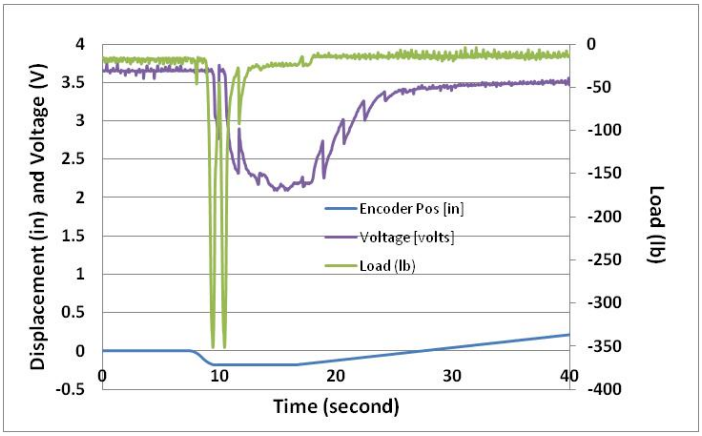

Fig. 50. Voltage, Displacement, Load vs. Time plots of single-side indentation at 12"/min

The IR images of the single side indentation are shown in Fig. 51 - Fig. 53. In some cases, the temperatures reached above 120˚C, although the localized thermal runaway areas were smaller due to the indenter size. In other cases, the maximum temperature rise was below 70˚C.

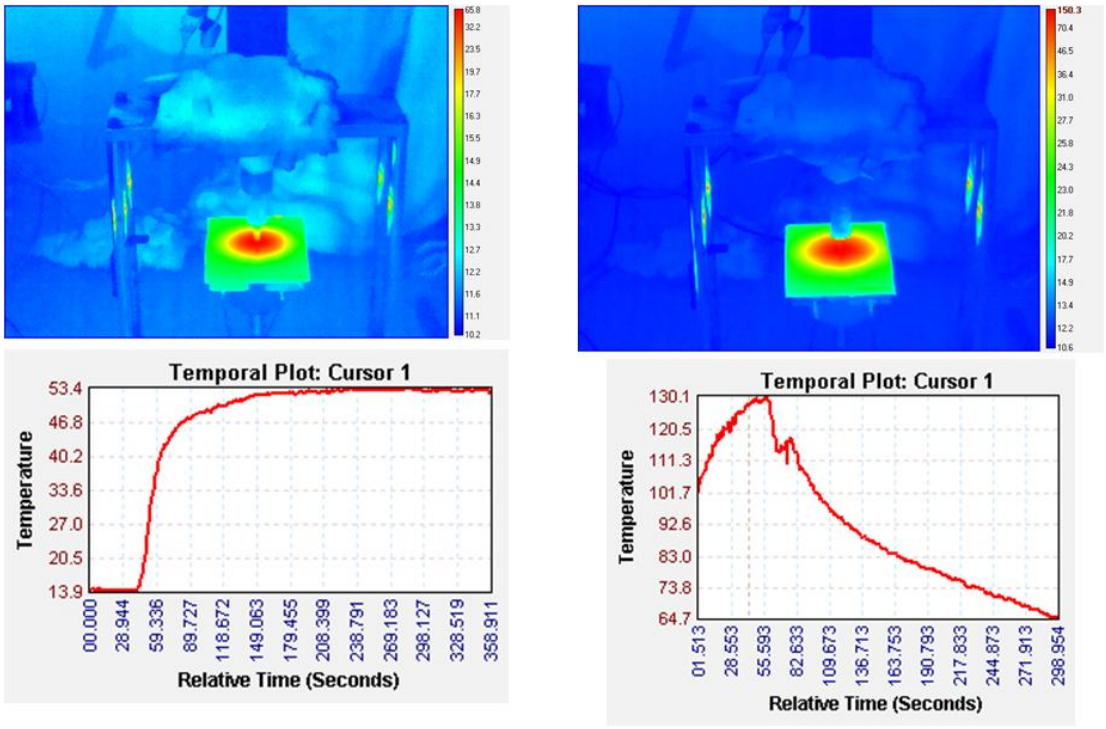

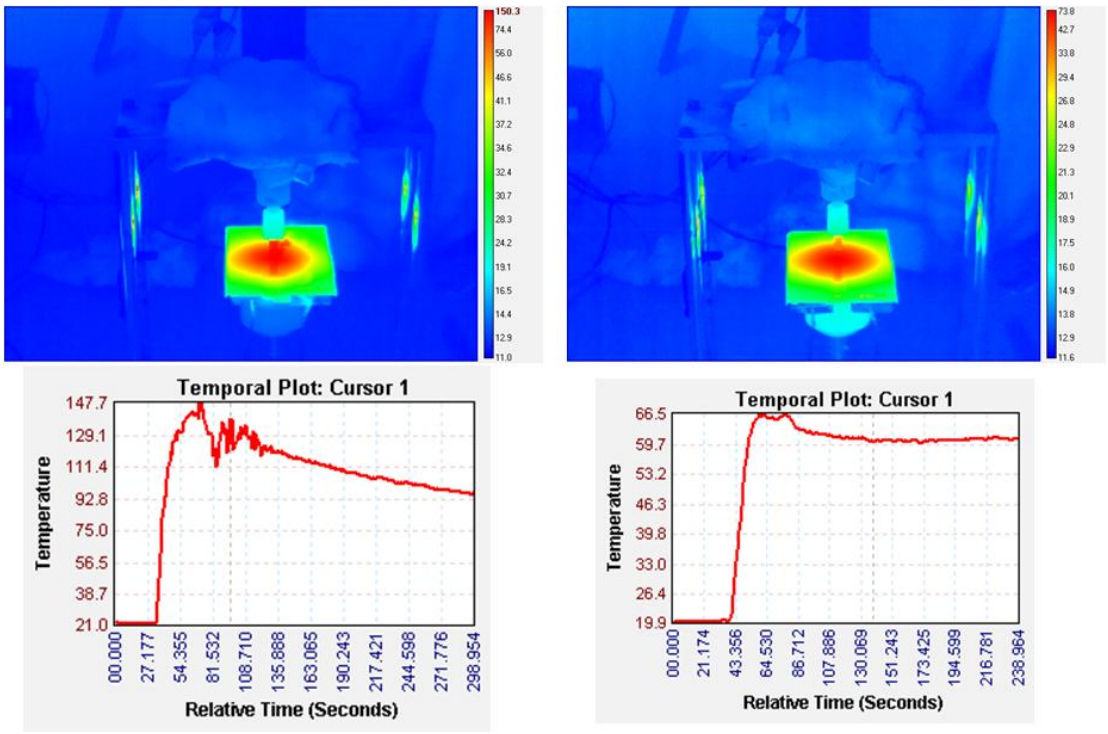

Fig. 51. IR images and temperature time profiles of four cells at 0.25”/min

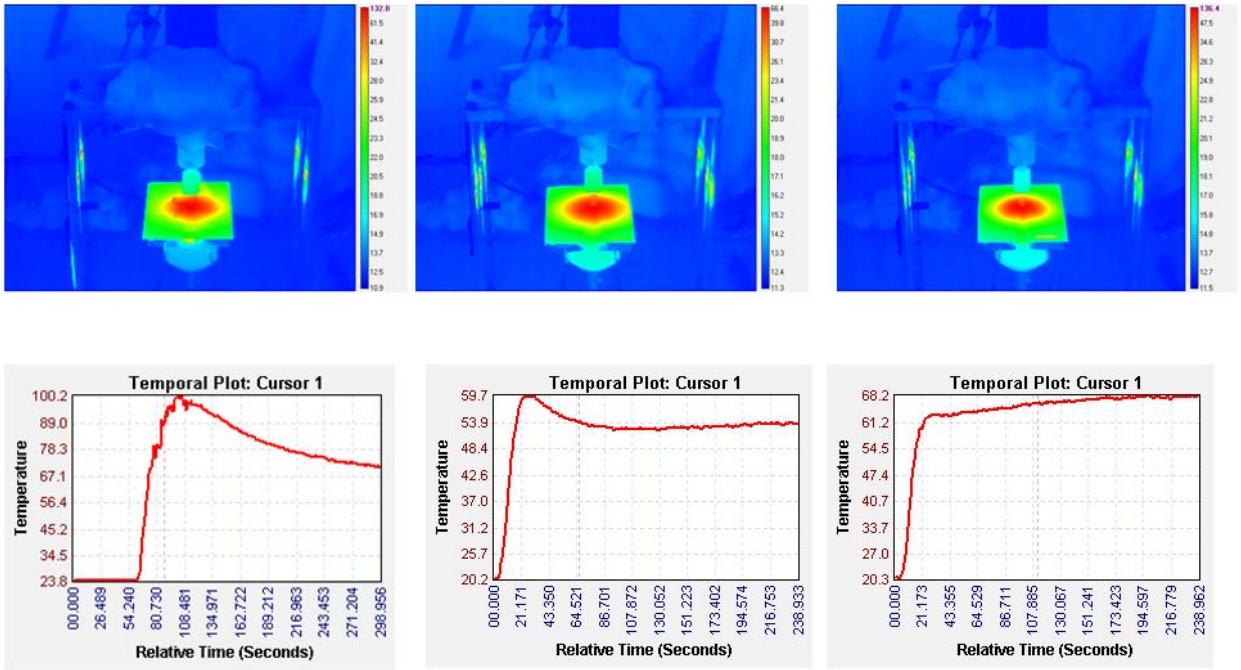

Fig. 52. IR images and temperature time profiles of three cells at 7”/min

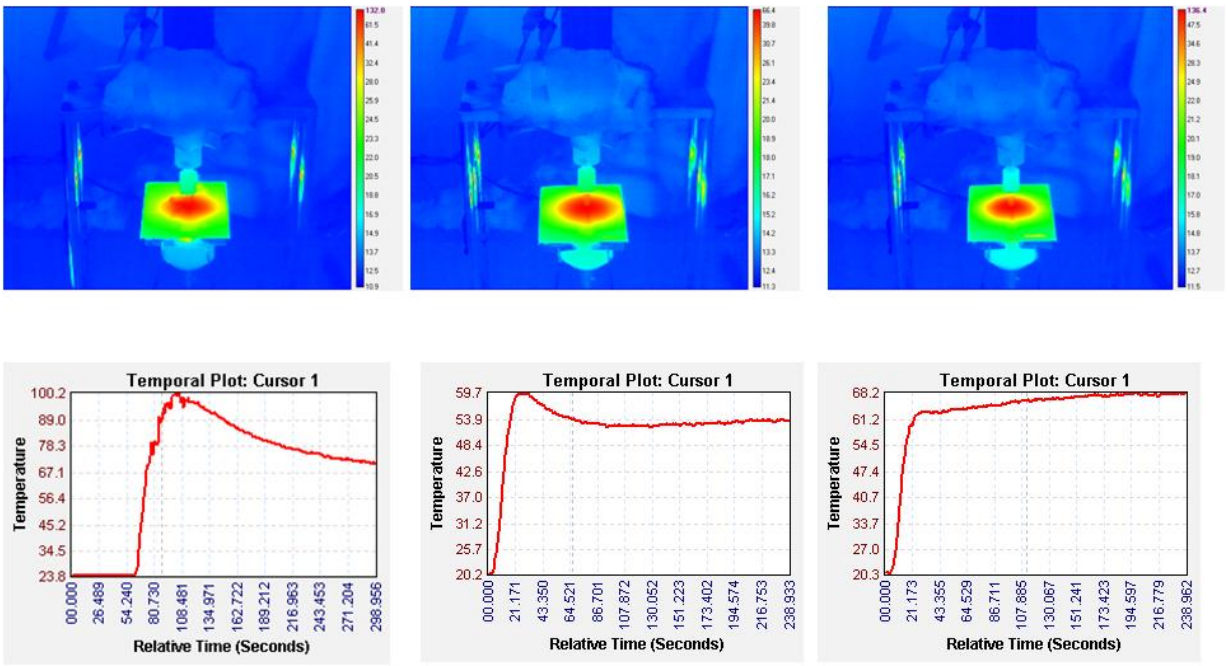

Fig. 53. IR images and temperature time profiles of three cells at 12”/min

The final set of experiment was single cells in single-side indentation against a plate using a 1” diameter indenter. Only one cell under each condition was tested. As shown in Fig. 54 - Fig. 56, the failure load increased from 600 pounds to 1200 pounds for the slower speed. Fig. 57 shows IR images and Temperature vs. Time plots of the three tests.

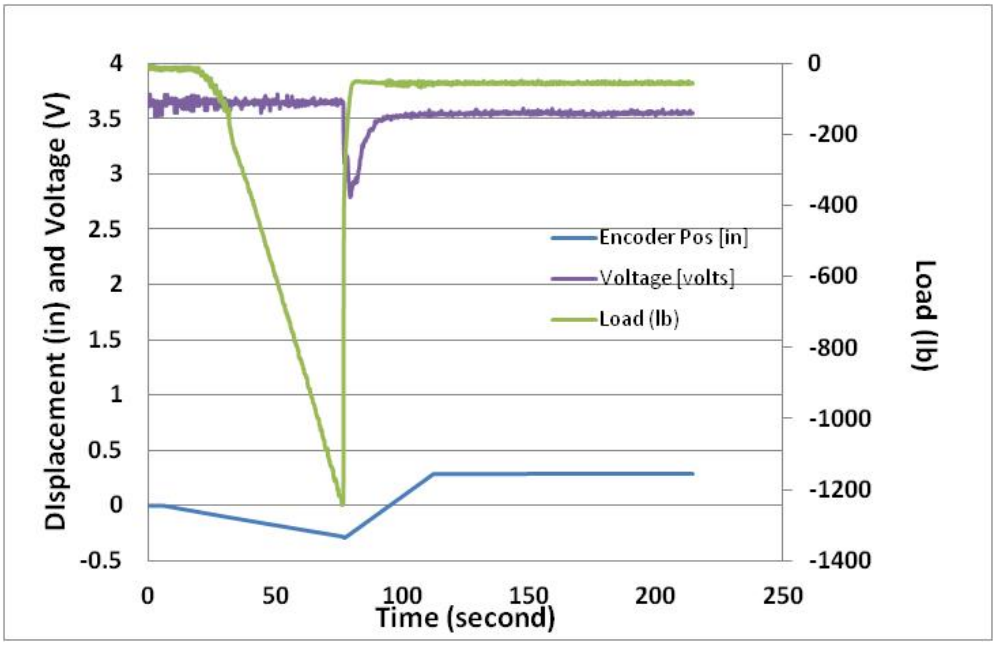

Fig. 54. Voltage, Displacement, Load vs. Time plots of single-side indentation at 0.25”/min

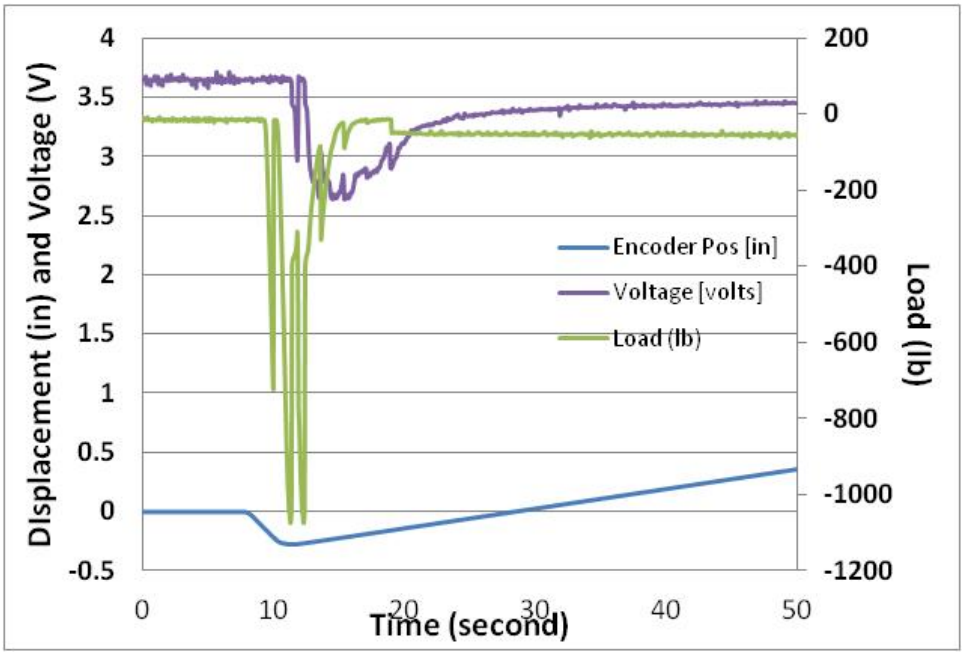

Fig. 55. Voltage, Displacement, Load vs. Time plots of single-side indentation at 7”/min

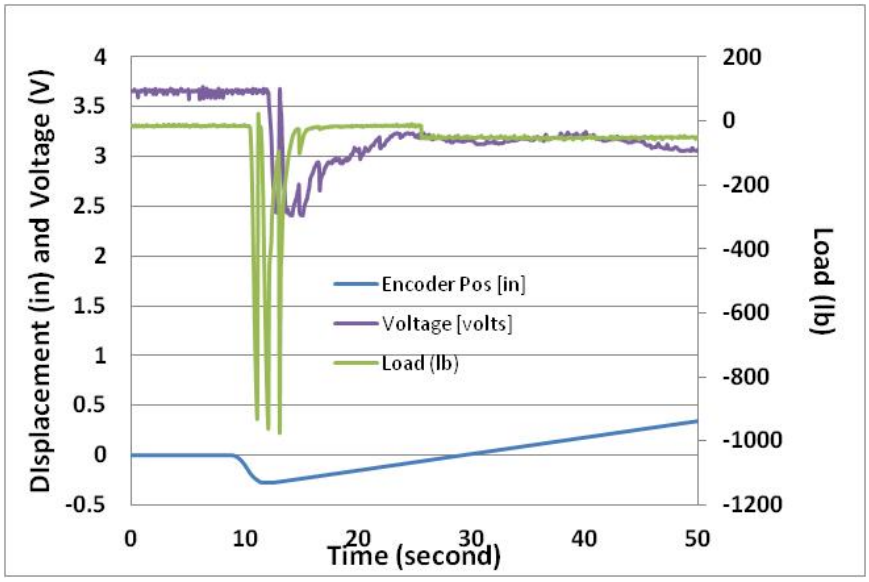

Fig. 56. Voltage, Displacement, Load vs. Time plots of single-side indentation at 12”/min

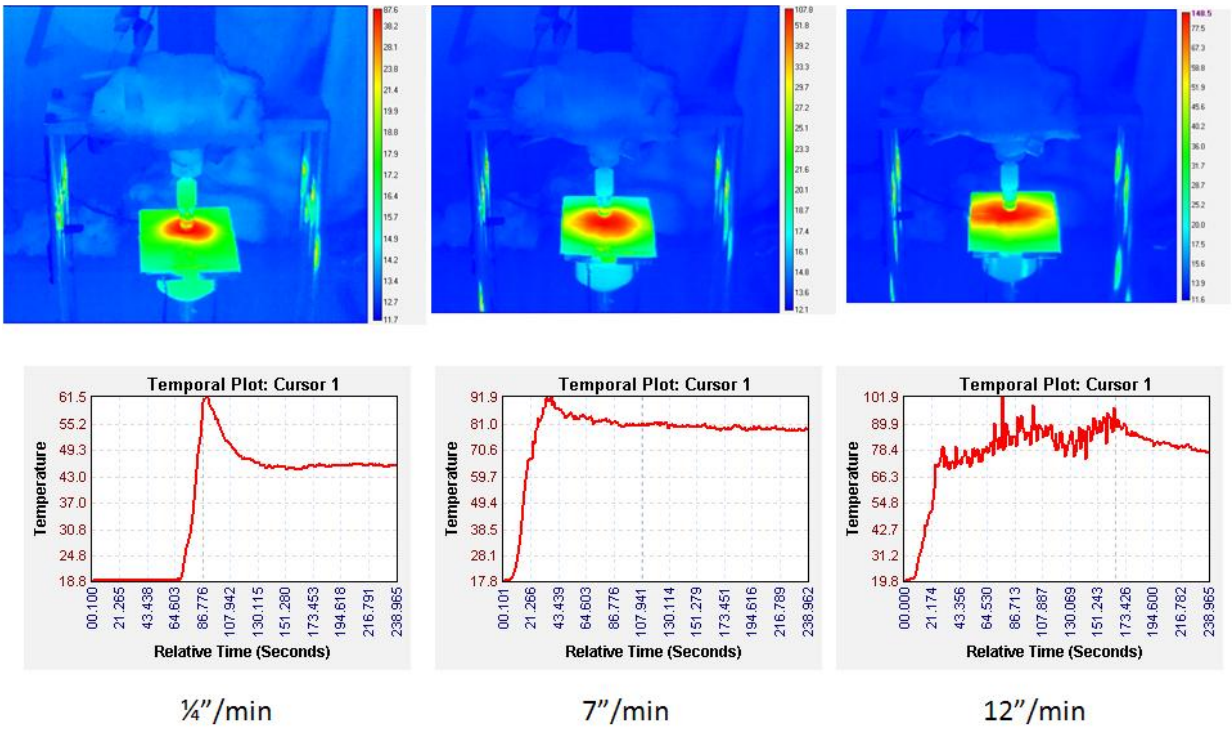

Fig. 57. IR images and temperature time profiles of three cells at 0.25", 7" and 12"/min.

In summary, mechanical simulation of high speed testing has been conducted using four test setups: 1) pinch test of single cells; 2) pinch test of 3P string; 3) Single-side indentation of 3P string; 4) Single-side indentation on single cells. These tests provided experimental data to the simulation efforts. Both mechanical deformation and temperature evaluation of the cells were recorded for this purpose. Several experimental related issues have been identified: 1) the load cell responses at high speeds (7"/min and 12"min) were noisy. It could be a real layered battery cell response or load cell electrical/mechanical issue; 2) the speed gap between 0.25"/min and 7"/min was too big. It has been suggested that testing at a couple more intermediate speeds is needed; 3) load cell calibration is needed. The load values were not critical in short circuit simulation. However, they are important to the modeling efforts. In order to verify the mechanical model, some materials level and layer level tests are needed to generate experimental data.

4.2 ADVANCES IN COUPLED ELECTRICAL-ELECTROCHEMICAL-THERMAL (EET) MODELS

In crush-induced shorts of Lithium-ion batteries, multiple physical phenomena closely interact and contribute to the thermal runaway event. The corresponding models have to be similarly coupled, as well. Unlike mechanics simulations where only the first few layers need to be resolved to capture the configuration of the internal short, the electrical-electrochemistry-thermal simulations are carried over corresponding domains of interest by resolving all the layers of current collectors and electrode materials. This is necessary to capture the total current flow through the shorted area and corresponding participation of the three-dimensional surface area of all the electrode layers. The thermal ramp due to the induced short and the following electrochemical reactions are highly nonlinear which require numerical methods capable of resolving different spatial and temporal scales. The sudden surges of electronic current and the heat through the shorted area require very stable solution techniques. We have explored several coupled solution techniques for solving the resulting nonlinear system of algebraic equations. Since the design of large format Li-Ion cell often involves several stacked electrode and current collector configurations where each domain is

discretized separately with different physical models, construction of full Jacobian matrix is computationally inefficient. In order to avoid constructing the full Jacobian and its inverse, we use a Jacobian-Free Newton Krylov (JFNK) method for our nonlinear solver. This technique is an established inexact Newton method that solves coupled nonlinear physics systems across spatial domains in a consistent manner. A Krylov subspace iterative linear solver, the generalized minimal residual method (GMRES), is used due to the non-symmetric Jacobian of the system. A preconditioner that exploits the stacked domains inherent in batteries is used to improve convergence of GMRES.

At low discharge rates linear dependence of averaged solid-phase Li concentration on surface Li concentration is sufficient to accurately predict the total discharge capacity. This is because the diffusion layer builds up to its steady state value as soon as the current is turned on. However, at higher rates this is not sufficient as concentration starts at zero and reaches the steady state value, suggesting that linear relation would be inadequate at short times or under high currents. We use Equation (13) to accurately represent the relation between the surface concentration and average concentration under the assumption of perfectly spherical particles, so that the discharge characteristics are accurate under high currents. We demonstrate the stability and robustness of the solution technique by discharging the 3D stacked cell sandwich at very high rates (Fig. 58).

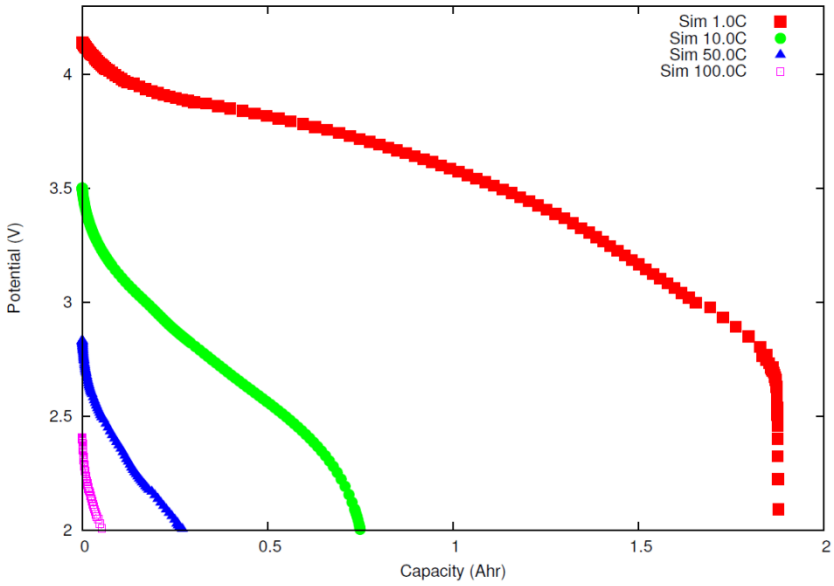

Fig. 58. Simulated discharge profiles of a cell sandwich under intermediate and very high current densities using 3D electrochemical model

Also we setup the simulation cases to short the batteries both externally and internally using representative boundary conditions. Under external shorting conditions, the potential difference between the electrical tabs is set to zero. We impose this condition gradually over few milliseconds to ensure all the gradients are captured properly. This gives rise to dramatic increase in total current passing through the system as shown in Fig. 59. Once the current reaches the peak value it starts to decay to equilibrate to a zero current system. For the internal short simulations, we select a pre-determined area in the separator region over which the damage happens and two electrodes come into contact. In this area, we impose contact resistance manually at the onset of the short and gradually decrease the resistivity over a short time to mimic increase in conductance under high load conditions. Internal short of the open circuit battery is easy to setup and simulate as long as you are able to transfer the deformations and contact area accurately from mechanics solution. But

during closed circuit i.e., charging or discharging, introducing an internal short is particularly challenging as the battery has developed gradients, and with any new conductance path the solution state needs to re-initialize to capture the evolution of the reaction currents. A new re-initializing scheme has been developed to compute the solution state with contact resistance to address this issue that allows us to capture the evolution of reaction currents.

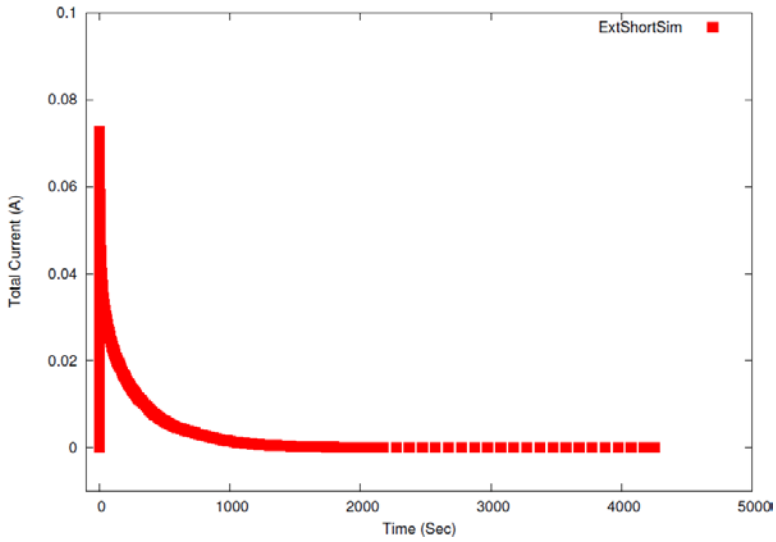

Fig. 59. Simulated evolution of cell current during external short circuit

In Fig. 60, we can see the increase in potential drop across the shorted area with decreasing contact resistance measured from the experiments in section 4.1.1. These contact resistivity values of 7.69×10^{-3} Ωm^2, 3.8×10^{-4} Ωm^2, and 7.69×10^{-6} Ωm^2 correspond to the different pressure values that are subjected to the negative and positive electrode pair.

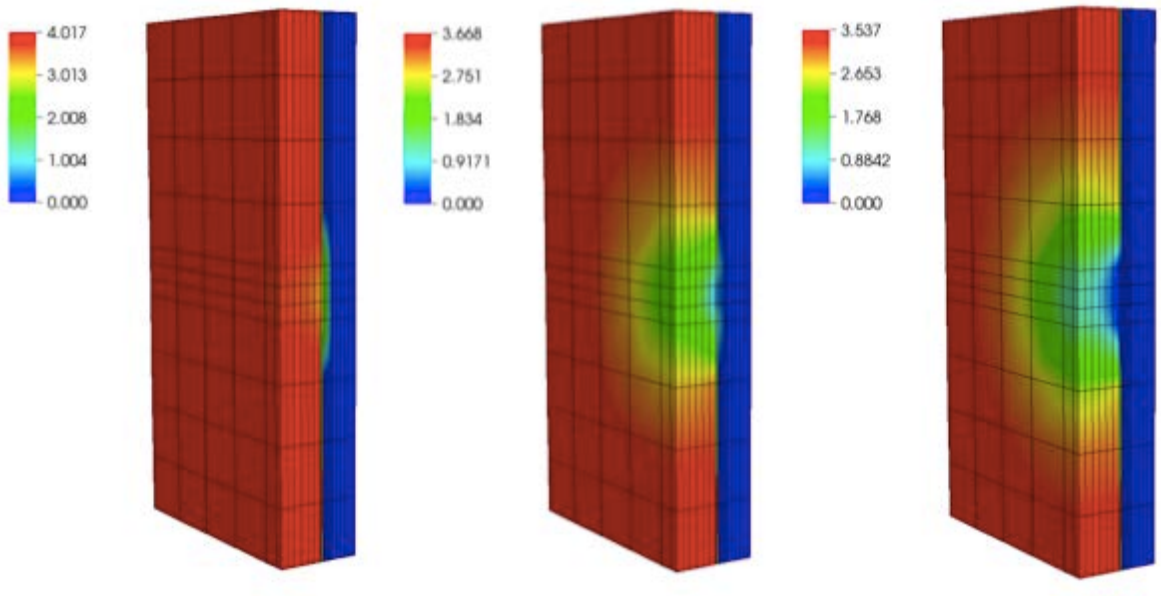

Fig. 60. Influence of contact resistance on potential distribution during internal short circuit

4.3 MODELING OF MECHANICAL DEFORMATIONS

In this section we describe the development of models for studying the mechanical deformation of Li-ion cells and for their coupling with EET models. The data used for validation of the simulations is based on the pinch testing of pouch cells described earlier in section 4.1. The commercial software package LS-DYNA has been used to create the FEM models for the cells. As described in section 3.2.3.1, most earlier efforts on modeling the deformation of Li-ion cells under external load were based on a homogenized approach, with effective properties for the entire cell or the jelly roll [84] - [87]. There has been limited effort at resolving the individual layers of the jelly roll and assigning appropriate material properties for each of these layers [90]. We explicitly model each of the cell layers in order to investigate possible internal failure mechanisms and simulate the configuration of the cell components involved in the internal electrical short. This configuration is then used in the EET model to assess the safety of the short for a given battery state.

The first several layers of a pouch cell used in this study, which consists of 17 jelly roll layers along the thickness direction, are fully resolved (different material parameters for pouch, active material coatings, separator and current collectors). The remaining layers of the cell are modeled using a homogenized material. It has been observed experimentally that internal short circuits occur in the cell layers closer to the indentation point, so that that above strategy is justified by the physical and computational arguments. The schematic for such a representation along the thickness of cell is shown in Fig. 61(b). In this particular example the top four jelly roll layers are fully resolved and a homogenized material represents the rest of the cell. The schematic for one individually resolved jelly roll layer is shown in Fig. 61(c), and there are four such jelly roll layers in this particular example. The remaining 13 layers are treated as a single material. We carried out simulations where the number of jelly roll layers that were individually resolved was varied between 1 and 8. It was found that resolving top 4 layers provided consistent results and an acceptable computational cost. The discretization approach would obviously need to be modified for other loading conditions and battery configurations. Figure 62 shows the different configurations used for the initial study to determine the appropriate number of layers that need to be resolved individually, and the corresponding load vs. displacement plots are shown in Fig. 63.

The piecewise linear plasticity material model (MAT-24) in LS-DYNA is used for the aluminum and copper current collectors and for separator layers. For both the anode and cathode active materials, crushable foam (MAT-63) material model is used. Parameters used in these models along with thickness and volume fraction of individual components are given in Table 16. For MAT-63 volumetric strain and stress values are required as an input. These volumetric strain and stress values are obtained from experiments on individual cells and entered in a tabular form in the material model. For homogenized material we used Voight averaging to calculate the lateral modulus (E_{33}),

$$E_{33} = \left[\frac{v_{pouch}}{E_{pouch}} + \frac{v_{copper}}{E_{copper}} + \frac{v_{anode}}{E_{anode}} + \frac{v_{seperator}}{E_{seperator}} + \frac{v_{cathode}}{E_{cathode}} + \frac{v_{aluminium}}{E_{aluminium}}\right]^{-1} \quad \ldots\ldots\ldots\ldots\ldots \quad (31)$$

where E and v denote the elastic moduli and volume fractions for individual components. The calculated value for E_{33} was 0.58 GPa. Volume fraction is calculated from the thickness of individual components and the number of layers for each component. In this particular configuration of the cell with 17 jelly roll layers, there are 2 pouch layers (one at the top and the other at the bottom), 18 copper layers, 17 aluminum layers, and 34 layers each of active electrode materials and the separator.

The battery pouch geometry used for the simulation has a length (x-direction) of 40 mm, width (y-direction) of 40 mm and thickness of 6.4 mm. The indentation test is conducted with a rigid sphere, which is moving downward at a constant speed. The diameter of the rigid sphere is 12.54 mm. The

bottom surface of the model is constrained by a rigid wall. Fully integrated solid elements are used to mesh the battery cell. Each cell component (foils, active materials, separator, pouch) is discretized by one to three solid elements in their thickness direction and assembled into the final model according to the cell's stacking sequence. Since such a discretization is insufficient to model details of localized failure in the individual layers, we focused instead on determining overall guidelines and discretization sensitivities for modeling the onset of failure.

We performed simulations to study the effect of varying the size of the geometry in the X-Y plane. Several cases of varying dimensions in the X-Y plane were studied. For spherical indenters, the domain length of approximately two times the indenter's diameter is required for converged force and deformation. This is illustrated in Fig. 64 where areal dimensions of 20 mm X 20 mm, 30 mm X 30 mm and 40 X 40 mm show almost identical load displacement curves.

The punch test results presented earlier in section 4.1 show that the onset of internal short circuit in the cell is indicated by a sudden drop in both the voltage and the load, resulting in contact between the anode and the cathode layers. The sudden drop indicates some form of internal mechanical instability and failure. The current model and experimental data were insufficient to postulate the character of internal failure mechanisms. As the first step towards developing an internal failure criteria for battery cells, we choose failure of the separator as a necessary condition for short circuit. A critical value of the effective strain in the separator was chosen to represent the failure threshold and it was treated as an adjustable parameter that can be chosen to match the experimental results. The magnitude of the failure strain was varied in the numerical simulation to match the resulting load-displacement curve with the corresponding experiment, as shown in Fig. 65. We have compared the simulation results with the experiment using a single cell indented on one side performed at a speed of 0.25 inch per minute. The load and displacement plots for this experimental result are shown in Fig. 48 and are reproduced in Fig. 65. It is seen that failure strain of 0.8 provides a good match between the simulation and experimental results. This match is limited to the experimental configuration and the FEM model used. Nevertheless, it gives a sense of the parameters and approaches that may be required for more realistic modeling.

The application of a failure criterion in the separator allows for detection of the onset of a short circuit. This is illustrated in Fig. 67(b), where the vertical coordinates (z-coordinates) of the cathode and anode are shown as a function of time. It can be seen that once the failure strain is exceeded in the separator, separator elements are removed, and the two layers come in contact, thus initiating the short circuit. The element failure is visible in the corresponding load drop in the load-displacement curve in Fig. 67(a). Distribution of the von Mises stress on the deformed mesh is shown in Fig. 66 for different cell components.

In addition to the simulations described above, we have carried out simulations of strings of two cells. We placed the two cells one on top of the other and performed the indentation simulation similar to that using a single cell. The overall geometry of the two cell configuration is shown in Fig. 68(a), and the load-displacement curves are shown in Fig. 68(c). For the top cell, the first four jelly roll layers are fully resolved and the remaining structure is treated as one homogenized material. For the bottom cell, all the jelly roll layers are treated as one homogenized material, as indicated in Fig. 68(b). Pouch layers separate the two cells. Since the bottom cell acts as a backup material that is softer compared to a rigid surface, the string of two cells requires a smaller load for the same displacement compared to the single cell, as shown in Fig. 68(c). When a critical failure strain of 0.8 is assumed for the separator, internal short occurs at a higher load and at a larger displacement for the two-cell string compared to the single cell case. This trend was also observed in the experimental data from the pinch tests, where internal short in the three-cell string occurs at higher load and displacement values (last plot in Fig. 47) compared to the single cell case (Fig. 48). The

simulations thus follow experimentally observed trend of the load-displacement behavior and the onset of internal short when multiple cells are stacked together.

Table 16. Dimensions and mechanical properties of Li-ion cell components

Material	Thickness Individual Layer (μm)	Volume Fraction	Young Modulus (GPa)	Poisson's Ratio	Tangent Modulus (GPa)	Yield Strength (MPa)	Failure Strain
Pouch	120	3.7	5.6	0.3	0.5	40	
Copper	11	3.0	117	0.3	2.0	70	
Anode	65	34	0.46	0.01			
Separator	24	12.5	0.5	0.3	0.05	60	0.1-0.8
Cathode	80	41.8	0.56	0.01			
Aluminum	19	5.0	70	0.3	1.0	10	

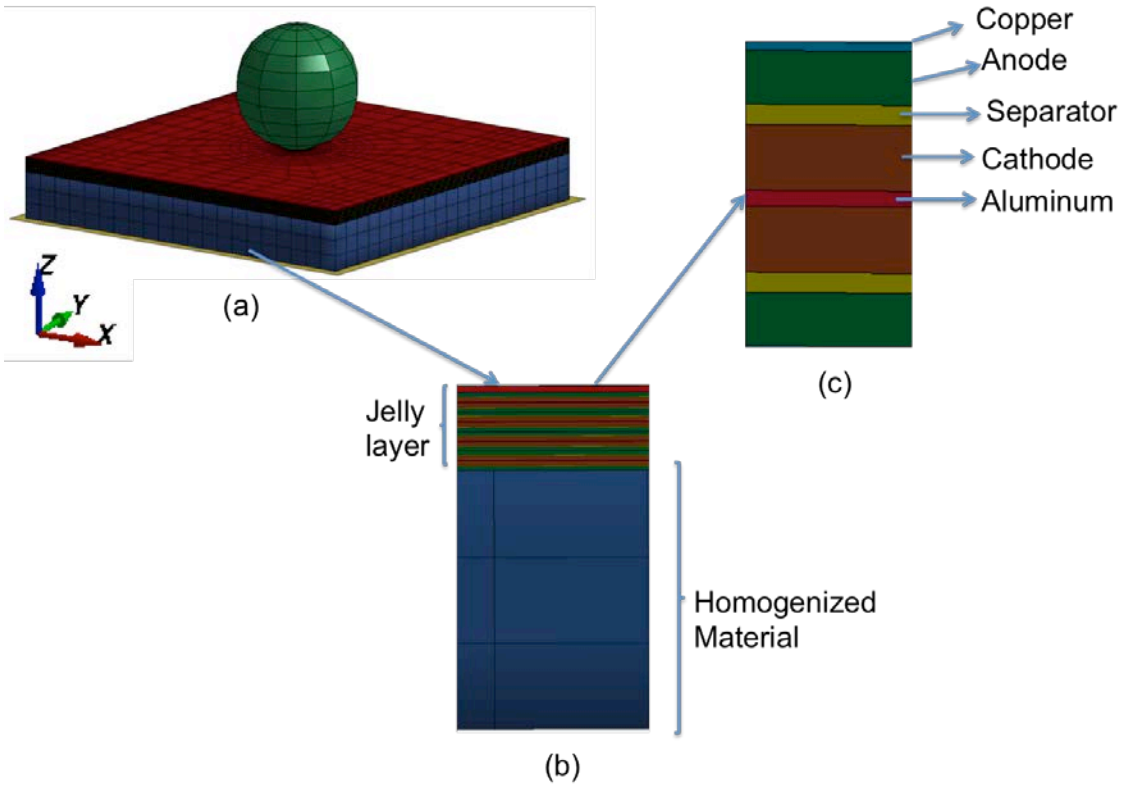

Fig. 61. Simulation of pinch test. (a) Mesh for Li-ion cell under spherical indenter, (b) Schematic along the thickness direction of the cell, and (c) Schematic of an individual jelly roll layer.

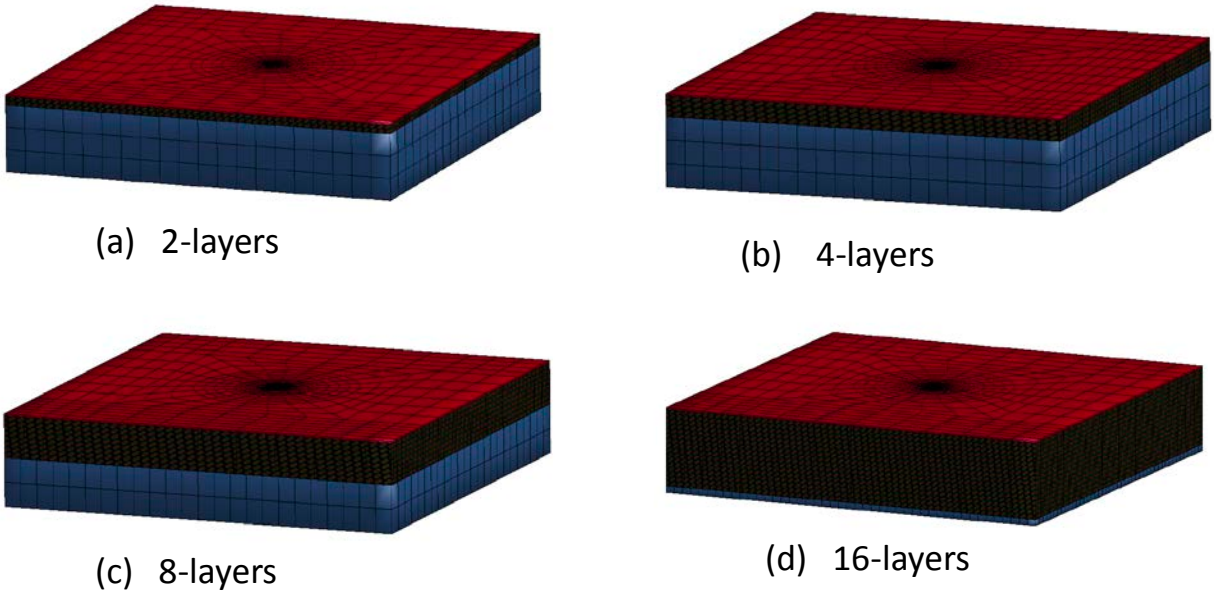

Fig. 62 Configurations showing different number of layers that are individually resolved for punch indentation simulations.

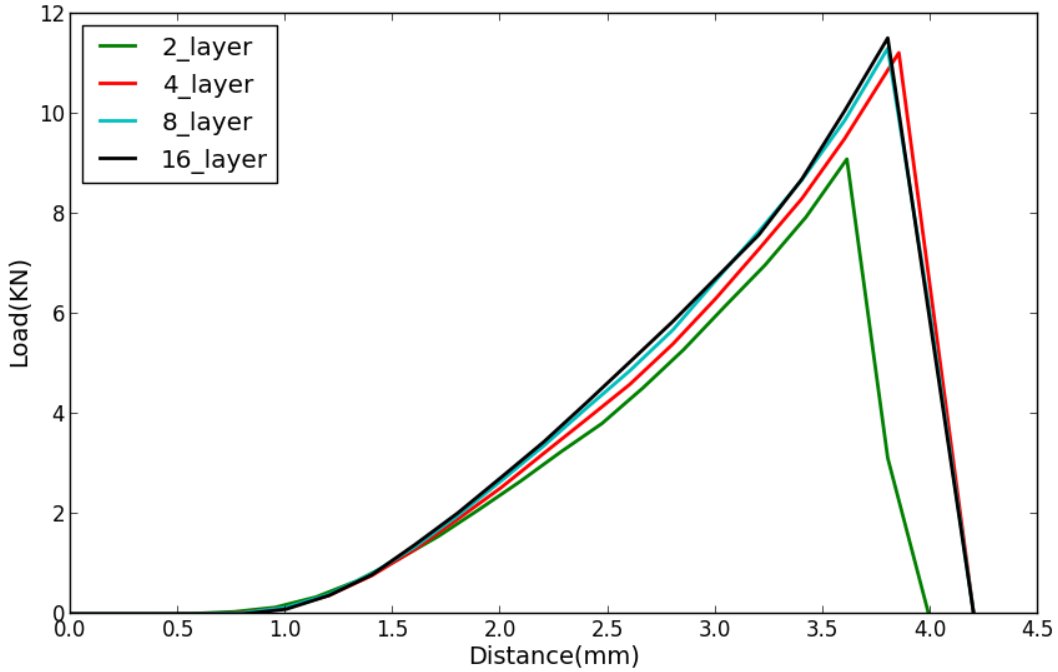

Fig. 63. Load-displacement plots for configurations shown in Fig. 62.

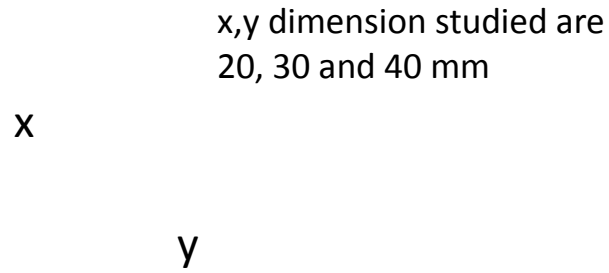

Fig. 64. Load-displacement curves for different sizes of the cell in the XY plane.

Fig. 65. Load-Displacement response for single cell and validation with experimental result.

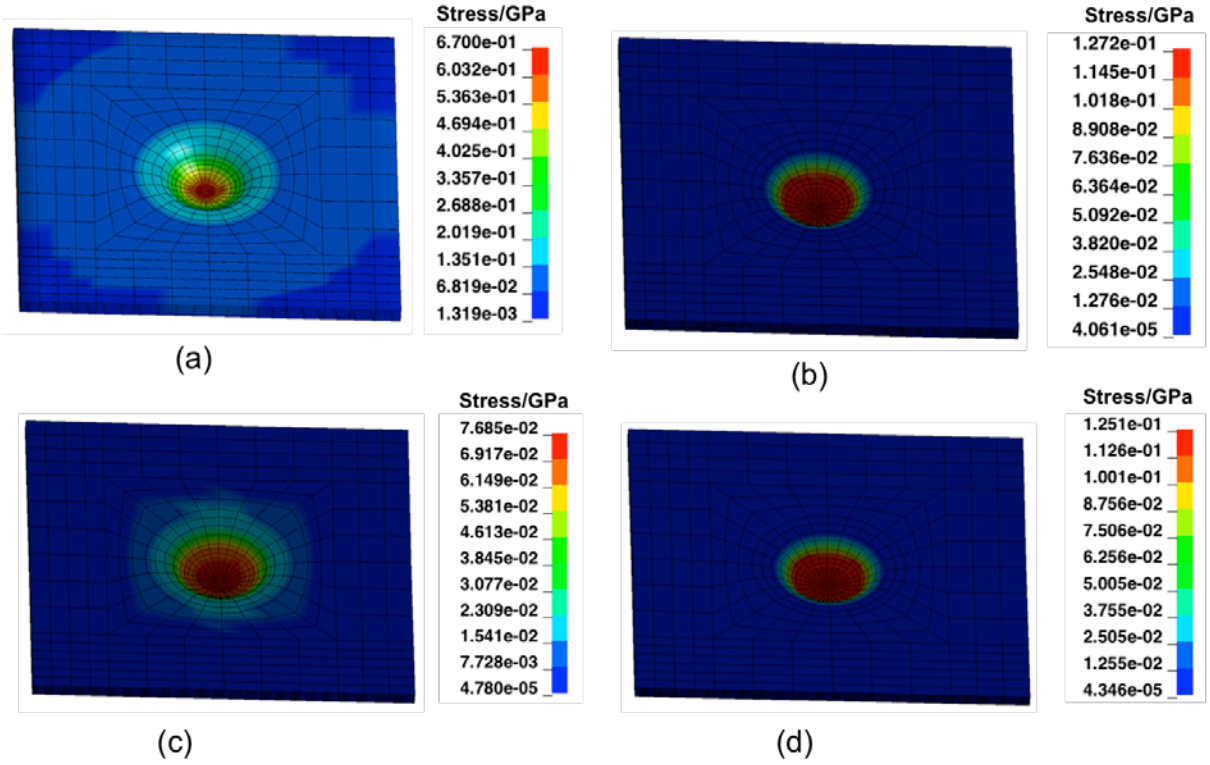

Fig. 66. Indentation-induced Von Mises stress in (a) copper current collector; (b) anode; (c) separator; (d) cathode.

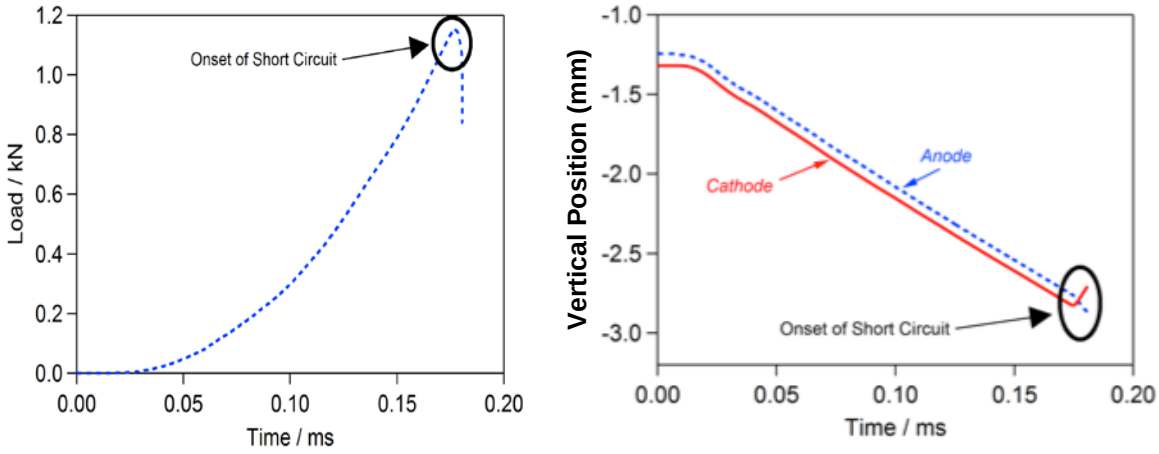

Fig. 67. Separator failure determines the onset of a short circuit as evidenced from (a) load drop, and (b) contact between the anode and the cathode.

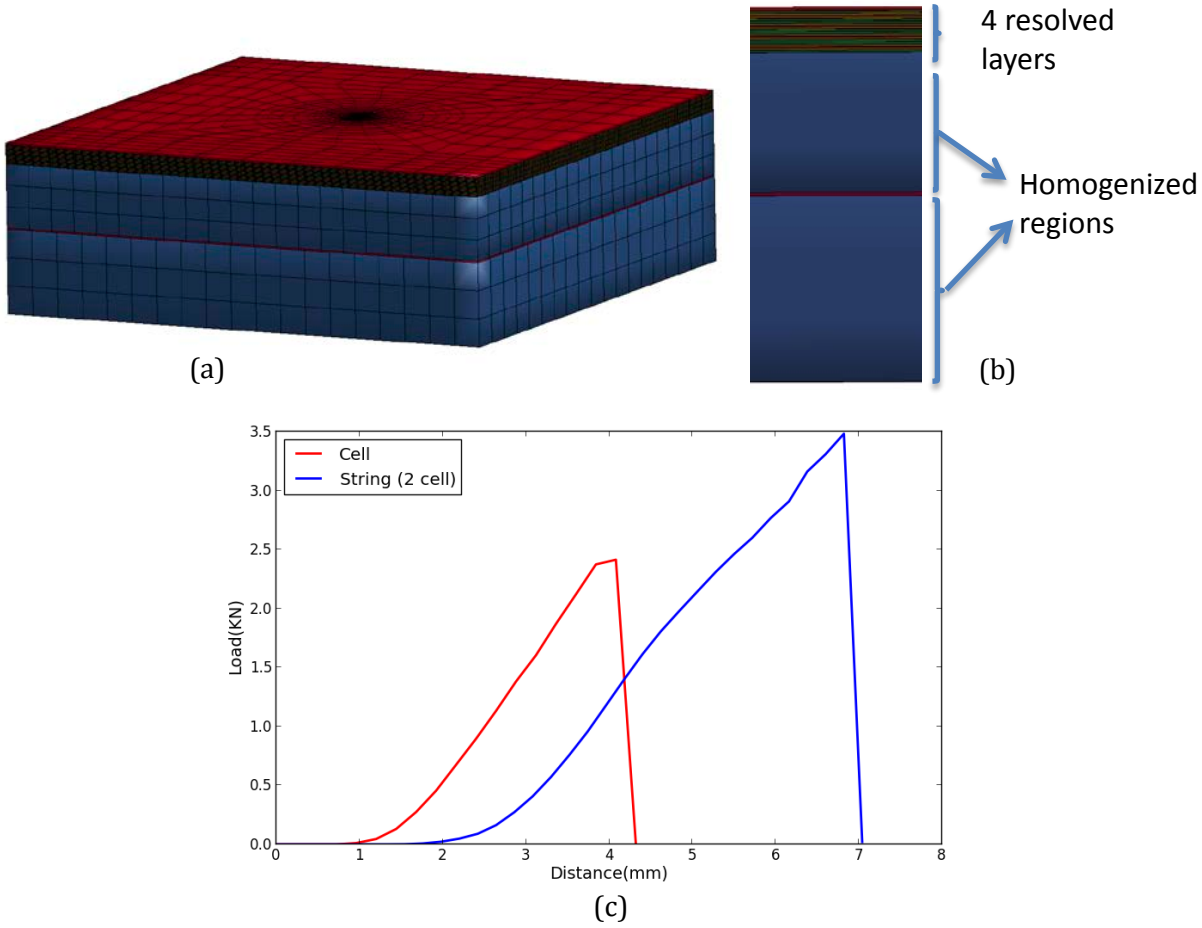

Fig. 68. Simulation of string with two cells showing (a) Mesh used, (b) Discretization through the thickness of cells, and (c) Load-displacement curve using separator failure criterion of 80 percent.

4.4 COUPLING OF EET AND MECHANICS

This section will discuss various aspects of coupling the mechanics and electro-chemical simulations. In the time period between load transfer across constituent materials to the onset of the short circuit, the primary influence is predominantly in one direction: from mechanical to electro-chemical solution states. Also, the mesh resolution requirements to capture solution gradients of the resolved electro-chemical simulation exceed the resolution of mechanics simulation. Under these considerations it is prudent to conduct the mechanics and electro-chemical simulations independently with solution transfer and mapping over different discretizations. OAS/VIBE framework has been used to efficiently orchestrate between the mechanics and electro-chemical software components for the short simulation. At every pre-determined time step the mechanical deformations are interpolated to the electro-chemical discretizations and the meshes are displaced. Once the failure of the separator is reached using maximum strain criterion in mechanics simulation, the corresponding elements in the electro-chemical meshes are identified and labeled with the new contact resistance model developed in Section 3.1.4. In Fig. 69 the electrode phase potentials are plotted at different instances with the displaced meshes using the solutions from mechanics simulations.

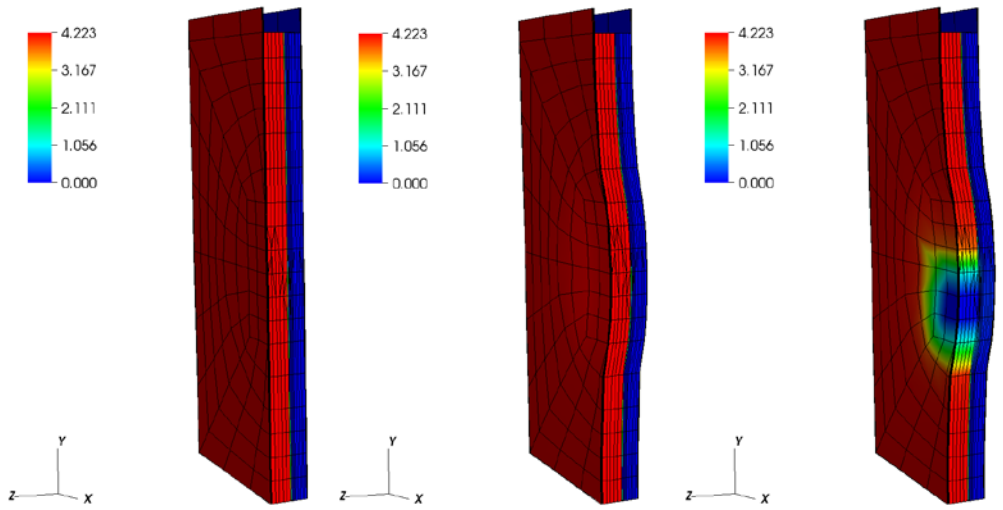

Fig. 69. Solid phase potential under mechanical induced deformations indicating onset of short

There are two critical aspects of solution transfer that need careful numerical treatment. Since the mesh resolution requirement is different for each physical component, the aspect ratios essentially lead to a different Jacobian of transformation for each discretization. Now to interpolate the solution from one discretization to another would lead to skewed elements and poorer mesh quality index. Also, in mechanics simulations, once the failure criterion is met in separator region the elements are eliminated from further computations. But the nodal connectivity and corresponding element are physically present. If these elements were used for computing transformations, this would lead to negative Jacobian or inverted elements. Both these circumstances would lead to degenerate solutions and failure of computational processes. Appropriate measures such as control of mesh quality and adaptive time stepping have to be employed to ensure that the stability and convergence of the numerical solution. These methods are currently under development and the presented result is for illustrative purposes only.

5. SUMMARY AND PATH FORWARD

Reviewing the available literature, we were unable to find any integrated tools that can predict the combined structural, electrical, electrochemical, and thermal response of batteries subjected to mechanical abuse that would be encountered in vehicle accident scenarios. In this project we have developed a preliminary software framework integrating electrochemical-electrical-thermal (EET) and mechanics simulations, and have developed and performed crush and fundamental experiments for determination of material properties and for validation.

We performed battery cell and string indentation tests at higher speeds than previously reported in the literature and found that observed quantities such as load, temperature and voltage, change drastically with change in speed. We are currently developing more advanced instrumentation for these dynamic indentation tests and are adding capability for higher loading speeds.

Most current models for mechanics simulation treat the cell as a single homogenized isotropic material. We have developed a model for cells in which there is an explicit representation of each individual component such as the active material, current collector, separator, etc., that predicts the onset of short-circuits based on failure in the separator layer. By resolving the electrode and separator layers and using constitutive and interface models that better represent the physics

during deformation, we can more accurately simulate deformation and the internal battery state (e.g. contact area and normal forces) at the onset of short circuits. Layer-resolved models also facilitate investigation of failure modes in materials leading to internal shorts and validation against experiments. These models will be used to determine the level of detail needed to evaluate short-circuit configuration, and to develop indicators and internal state variables for constitutive models and FEM formulations at larger length scales. We can also apply these models to other geometries (cylindrical) and chemistries.

Since a fully layer-resolved approach is impractical for vehicle-scale simulations due to computational expense, we have developed an adaptive approach in which regions near damage are resolved while remaining regions are homogenized. As we go from cells to modules and packs, we are exploring automating these adaptive techniques where cells are treated as homogenous regions wherever possible, and only when cells are subjected to strain rates leading to failure are more detailed models used. This approach will make the capability computationally feasible for routine module and pack simulations.

It is also important to note that electrode and electrolyte parameters that are known at the beginning of life vary with aging and degradation, and in the absence of data or models, these variations require estimation. There are also uncertainties in manufacturing, materials (e.g. impurities), battery management systems, and state-of-charge at impact.

Finally, for this project we used a plasticity-driven material model for the separator, which may not be the best approximation for such highly porous polymeric material. Viscoelastic and poroelastic material models may be more suitable for separators as they can also include rate effects. We also have not included the effect of friction between individual layers in the current study; however forces at interfaces may play a role in separator failure. This can be addressed by considering sliding between layers in the FEM model. We have not yet considered the loading rate in these simulations; we will incorporate this by considering strain-rate based material models. To develop more accurate constitutive models for active materials there is a need to characterize the compressive performance of these porous layers under different loading conditions. An effort is currently underway in other research projects to characterize individual components of cells, especially active materials and separators.

6. REFERENCES

[1] Huggins, R. (2008). “Advanced batteries: materials science aspects” Springer, 474 pp.

[2] Yoshio, M., Brodd, R. J,. et al. (2009). “Lithium-Ion Batteries: Science and Technologies” Springer, 452 pp.

[3] Takahashi, M., Takabayashi, M., et al. (2013). “Investigation of the Impact Phenomenon During Minor Collision.” SAE International Journal of Alternative Powertrains **2**(1): 187-193.

[4] Lim, J. M., Seo, S., et al. (2008). “Evaluation of Crash Protection for Hybrid Electrical Vehicle under Rear Impact”, SAE Technical Paper 2008-01-0189.

[5] Kai, X., Xueping, W., et al. (2014). “Comparative research on standards and regulations of electric vehicle post crash safety requirement Transportation Electrification Asia-Pacific” (ITEC Asia-Pacific), 2014 IEEE Conference and Expo.

[6] SAE International (2014). "Recommended Practice for Electric, Fuel Cell and Hybrid Electric Vehicle Crash Integrity Testing” SAE J1766.

[7] National Highway Traffic Safety Administration (2006). “Electric Powered Vehicles: Electrolyte Spillage and Electrical Shock Protection”, FMVSS No. 305. U.S. DOT.
[8] Sahraei, E., Wierzbicki, T., et al. (2010). “Crash safety of lithium-ion batteries towards development of a computational model.” SAE Technical Paper 2010-01-1078.
[9] Lai, W.-J., Ali, M. Y., et al. (2014). "Mechanical behavior of representative volume elements of lithium-ion battery cells under compressive loading conditions” Journal of Power Sources **245**: 609-623.
[10] Lai, W.-J., Ali, M. Y., et al. (2014). "Mechanical behavior of representative volume elements of lithium-ion battery modules under various loading conditions” Journal of Power Sources **248**: 789-808.
[11] Allu, S., Kalnaus, S., et al. (2014). "A new open computational framework for highly- resolved coupled three-dimensional multiphysics simulations of Li-ion cells" Journal of Power Sources **246**: 876-886.
[12] Kalnaus, S., Pannala, S., et. al.(2015). "CAEBAT OAS/VIBE – Production Release v1.1“ http://www.batterysim.org.
[13] Ren, F., Cox, T., et al. (2014). "Thermal runaway risk evaluation of Li-ion cells using a pinch–torsion test." Journal of Power Sources **249**: 156-162.
[14] Wang, C. Y., Gu, W. B., et al. (1998). "Micro-macroscopic coupled modeling of batteries and fuel cells - I. Model development." Journal of the Electrochemical Society **145** (10): 3407-3417.
[15] Gu, W. B., Wang, C. Y., (1999). "Modeling discharge and charge characteristics of nickel–metal hydride batteries." Electrochimica Acta **44** (25): 4525-4541.
[16] Gu, W. B., Wang, C. Y., (2000). "Thermal-Electrochemical Modeling of Battery Systems." Journal of the Electrochemical Society **147** (8): 2910-2922.
[17] Doyle, M., Newman, J., et al. (1996). "Comparison of Modeling Predictions with Experimental Data from Plastic Lithium Ion Cells." Journal of the Electrochemical Society **143**(6): 1890-1903.
[18] Doyle, M., Fuller, T. F., et al. (1993). "Modeling of Galvanostatic Charge and Discharge of the Lithium Polymer Insertion Cell." Journal of the Electrochemical Society **140** (6): 1526-1533.
[19] Newman, J., and Tiedemann, W. (1993). "Potential and Current Distribution in Electrochemical Cells." Journal of the Electrochemical Society **140** (7): 1961-1968.
[20] Gu, H. (1983). "Mathematical Analysis of a Zn / NiOOH Cell." Journal of the Electrochemical Society **130** (7): 1459-1464.
[21] Liaw, B. Y., Jungst, R. G., et al. (2005). "Modeling capacity fade in lithium-ion cells." Journal of Power Sources **140** (1): 157-161.
[22] Kim, G.-H., Smith, K., et al. (2012). "Fail-safe design for large capacity lithium-ion battery systems." Journal of Power Sources **210**: 243-253.
[23] Plett, G. L. (2004). "Extended Kalman filtering for battery management systems of LiPB-based HEV battery packs: Part 1. Background." Journal of Power Sources **134** (2): 252-261.
[24] Plett, G. L. (2004). "Extended Kalman filtering for battery management systems of LiPB based HEV battery packs: Part 2. Modeling and identification." Journal of Power Sources **134** (2): 262-276.

[25] Plett, G. L. (2004). "Extended Kalman filtering for battery management systems of LiPB-based HEV battery packs: Part 3. State and parameter estimation." Journal of Power Sources **134**(2): 277-292.

[26] Yang, G. (2014). "Battery parameterisation based on differential evolution via a boundary evolution strategy." Journal of Power Sources **245**: 583-593.

[27] Verbrugge, M. W., and Conell, R. S. (2002). "Electrochemical and Thermal Characterization of Battery Modules Commensurate with Electric Vehicle Integration" Journal of the Electrochemical Society **149**(1): A45-A53.

[28] Awarke, A., Jaeger, M., et al. (2013). "Thermal analysis of a Li-ion battery module under realistic EV operating conditions." International Journal of Energy Research **37**(6): 617-630.

[29] Smith, K., Kim, G. H., et al. (2010). "Thermal/electrical modeling for abuse-tolerant design of lithium ion modules." International Journal of Energy Research **34**(2): 204-215.

[30] Offer, G. J., Yufit, V., et al. (2012). "Module design and fault diagnosis in electric vehicle batteries." Journal of Power Sources **206**: 383-392.

[31] Bernardi, D., Pawlikowski, E., et al. (1985). "A General Energy Balance for Battery Systems." Journal of the Electrochemical Society **132**(1): 5-12.

[32] Fan, L., Khodadadi, J. M., et al. (2013). "A parametric study on thermal management of an air-cooled lithium-ion battery module for plug-in hybrid electric vehicles." Journal of Power Sources **238**: 301-312.

[33] Smyshlyaev, A., Krstic, M., et al. (2011). "PDE model for thermal dynamics of a large Li-ion battery pack." American Control Conference (ACC), 2011.

[34] Saw, L. H., Somasundaram, K., et al. (2014). "Electro-thermal analysis of Lithium Iron Phosphate battery for electric vehicles." Journal of Power Sources **249**: 231-238.

[35] Sun, H., Wang, X., et al. (2012). "Three-dimensional thermal modeling of a lithium- ion battery pack." Journal of Power Sources **206**: 349-356.

[36] Fuller, T. F., Doyle, M., et al. (1994). "Simulation and Optimization of the Dual Lithium Ion Insertion Cell." Journal of the Electrochemical Society **141**(1): 1-10.

[37] Srinivasan, V. and Wang, C. Y. (2003). "Analysis of Electrochemical and Thermal Behavior of Li-Ion Cells." Journal of the Electrochemical Society **150**(1): A98-A106.

[38] Haran, B. S., Popov, B. N., et al. (1998). "Determination of the hydrogen diffusion coefficient in metal hydrides by impedance spectroscopy." Journal of Power Sources **75**(1): 56-63.

[39] Ning, G. and Popov, B. N. (2004). "Cycle Life Modeling of Lithium-Ion Batteries." Journal of the Electrochemical Society **151**(10): A1584-A1591.

[40] Santhanagopalan, S., Guo, Q., et al. (2006). "Review of models for predicting the cycling performance of lithium ion batteries." Journal of Power Sources **156**(2): 620-628

[41] Guo, M., Sikha, G., et al. (2011). "Single-Particle Model for a Lithium-Ion Cell: Thermal Behavior." Journal of the Electrochemical Society **158**(2): A122-A132.

[42] Li, X., He, F., et al. (2013). "Thermal management of cylindrical batteries investigated using wind tunnel testing and computational fluid dynamics simulation." Journal of Power Sources **238**(0): 395-402.

[43] Xun, J., Liu, R., et al. (2013). "Numerical and analytical modeling of lithium ion battery thermal behaviors with different cooling designs." Journal of Power Sources **233**(0): 47-61.
[44] Smith, K., and Wang, C.-Y. (2006). "Power and thermal characterization of a lithium ion battery pack for hybrid-electric vehicles." Journal of Power Sources **160**(1): 662-673.
[45] Guo, M., Kim, G.-H., et al. (2013). "A three-dimensional multi-physics model for a Li- ion battery." Journal of Power Sources **240**(0): 80-94.
[46] Santhanagopalan, S., Ramadass, P., et al. (2009). "Analysis of internal short-circuit in a lithium ion cell." Journal of Power Sources **194**(1): 550-557.
[47] Dahn, J. R. (2001). Lithium-Ion Battery Tutorial and Update. Power 2001. Oct. 2001, Anaheim, CA
[48] Fouchard, D., Xie, L., et al. (1995). *Rechargeable Lithium and Lithium-Ion Batteries*, Megahed, S., Barnett, B.M., Xie, L. Editors, PV 94-28: 348; The Electrochemical Society Proceedings Series, Pennington, NJ, USA
[49] Saito, Y., Takano, K., et al. (2001). "Thermal behaviors of lithium-ion cells during overcharge." Journal of Power Sources **97–98**(0): 693-696
[50] Winter, M. and Brodd, R. J. (2004). "What Are Batteries, Fuel Cells, and Supercapacitors?" Chemical Reviews **104**(10): 4245-4270.
[51] Zemansky, M. W. (1968). Heat and Thermodynamics, Wiley, Inc.
[52] Spotnitz, R. and Franklin, J. (2003). "Abuse behavior of high-power, lithium-ion cells." Journal of Power Sources **113**(1): 81-100.
[53] "1625-2008 - IEEE Standard for Rechargeable Batteries for Multi-Cell Mobile Computing Devices." IEEE SA -. Web. 20 Jan. 2015. <http://standards.ieee.org/findstds/standard/1625-2008.html>.
[54] Ramadass, P., Fang, W., et al. (2014). "Study of internal short in a Li-ion cell I. Test method development using infra-red imaging technique." Journal of Power Sources **248**(0): 769-776.
[55] Lamb, J., and Orendorff, C., (2014). "Evaluation of mechanical abuse techniques in lithium ion batteries." Journal of Power Sources **247**: 189-196.
[56] Kitoh, K., and Nemoto, H., (1999). "100 Wh large size Li-ion batteries and safety tests." Journal of Power Sources **81-82**: 887-890.
[57] SAND 2005-3123 Technical Report (2005). "Freedom CAR Electrical Energy Storage System Abuse Test Manual for Electric and Hybrid Electric Vehicle Applications." By Doughty, D., and Crafts, C., Sandia National Laboratories http://prod.sandia.gov/techlib/access-control.cgi/2005/053123.pdf
[58] SAE J2464-200911 (2009). "Electric and Hybrid Electric Vehicle Rechargeable Energy Storage System (RESS) Safety and Abuse Testing." SAE International, Revision 11/06/2009.
[59] Hatchard, T.D., Trussler, S., Dahn, J.R., (2014). "Building a 'smart nail' for penetration tests on Li-ion cells." Journal of Power Sources **247**: 821-823.
[60] "Recommendations on the Transport of Dangerous Goods – Manual of Tests and Criteria" (2009). United Nations Publication, ISSN 1014-7160, 5th Revised Edition, Amendment 1: 43-51.
[61] Maleki, H., Howard, J., (2009). "Internal short circuit in Li-ion cells." Journal of Power Sources **191**: 568-574.

[62] Fang, W., Ramadass, P., et al. (2014). "Study of internal short in a Li-ion cell-II. Numerical investigation using a 3D electrochemical-thermal model." Journal of Power Sources **248**(0): 1090-1098.

[63] Richard, M. N. and Dahn, J. R. (1999). "Accelerating Rate Calorimetry Study on the Thermal Stability of Lithium Intercalated Graphite in Electrolyte. I. Experimental." Journal of the Electrochemical Society **146**(6): 2068-2077.

[64] Richard, M. N. and Dahn, J. R. (1999). "Accelerating Rate Calorimetry Study on the Thermal Stability of Lithium Intercalated Graphite in Electrolyte. II. Modeling the Results and Predicting Differential Scanning Calorimeter Curves." Journal of the Electrochemical Society **146**(6): 2078-2084.

[65] MacNeil, D. D. and Dahn, J. R. (2001). "Test of Reaction Kinetics Using Both Differential Scanning and Accelerating Rate Calorimetries As Applied to the Reaction of LixCoO2 in Non-aqueous Electrolyte." The Journal of Physical Chemistry A **105**(18): 4430-4439.

[66] MacNeil, D. D. and Dahn, J. R. (2001). "The Reaction of Charged Cathodes with Nonaqueous Solvents and Electrolytes: I. Li0.5CoO2." Journal of the Electrochemical Society **148**(11): A1205-A1210.

[67] MacNeil, D. D. and Dahn, J. R. (2001). "The Reaction of Charged Cathodes with Nonaqueous Solvents and Electrolytes: II. LiMn2 O 4 charged to 4.2 V." Journal of the Electrochemical Society **148**(11): A1211-A1215.

[68] MacNeil, D. D., Hatchard, T. D., et al. (2001). "A Comparison Between the High Temperature Electrode /Electrolyte Reactions of Li x CoO2 and Li x Mn2 O 4." Journal of the Electrochemical Society **148**(7): A663-A667.

[69] Hatchard, T. D., MacNeil, D. D., et al. (2001). "Thermal Model of Cylindrical and Prismatic Lithium-Ion Cells." Journal of the Electrochemical Society **148**(7): A755-A761.

[70] Arai, H., Tsuda, M., et al. (2002). "Thermal Reactions Between Delithiated Lithium Nickelate and Electrolyte Solutions." Journal of the Electrochemical Society **149**(4): A401-A406.

[71] Kim, G. H., Pesaran, A., et al. (2007). "A three-dimensional thermal abuse model for lithium-ion cells." Journal of Power Sources **170**(2): 476-489.

[72] Lai, W.J., Ali, M., Pan, J. (2014). "Mechanical behavior of representative volume elements of lithium-ion battery modules under various loading conditions." Journal of Power Sources **248**: 789-808.

[73] Sahraei, E., R. Hill, and Wierzbicki, T. (2012). "Calibration and finite element simulation of pouch lithium-ion batteries for mechanical integrity." Journal of Power Sources,. **201**: 307-321.

[74] Lai, W.J., Ali, M., Pan, J., (2014). "Mechanical behavior of representative volume elements of lithium ion battery cells under compressive loading conditions." Journal of Power Sources **245**: 609-623.

[75] Zheng, H., Tan, L., Liu, G., Song, X., Battaglia, V.S. (2012). "Calendering effects on the physical and electrochemical properties of $Li[Ni_{1/3}Mn_{1/3}Co_{1/3}]O_2$ cathode." Journal of Power Sources **208**: 52-57.

[76] Zheng, H., Tan, L., Liu, G., Song, X., Battaglia, V.S. (2012). "Correlationship between electrode mechanics and long term cycling performance for graphite anode in lithium ion cells." Journal of Power Sources **217**: 530-537.
[77] Sheidaei, A., Xiaoa, X., et al. (2014). "Mechanical behavior of a battery separator in electrolyte solutions." Journal of Power Sources **248**: 789-808.
[78] Venugopal, G., et al. (1999). "Characterization of microporous separators for lithium-ion batteries." Journal of Power Sources **77**(1): 34-41.
[79] Love, C.T. (2011). "Thermomechanical analysis and durability of commercial microporous polymer Li-ion battery separators." Journal of Power Sources **196**: 2905-2912.
[80] Avdeev, I., Martinsen, M., and Francis, A. (2014). "Rate- and Temperature-Dependent Material Behavior of a Multilayer Polymer Battery Separator." Journal of Materials Engineering and Performance **23**: 315.
[81] Chen, J., Yan Y.T., et al. (2014). "Deformation and fracture behaviors of microporous polymer separators for lithium ion batteries." RSC Advances **4**: 14904.
[82] Gor, G.Y., Cannarella, J., Prevost, J.H., Arnold, C.B. (2014). "A model for the behavior of battery separators in compression at different strain/charge rates." Journal of the Electrochemical Society **161**(11): F3065-F3071.
[83] Wierzbicki, T., Sahraei, E., (2013). "Homogenized mechanical properties for the jelly roll of cylindrical lithium-ion cells." Journal of Power Sources **241:** 467-476.
[84] Sahraei, E., J. Meier, and T. Wierzbicki (2014). Characterizing and modeling mechanical properties and onset of short circuit for three types of lithium-ion pouch cells. Journal of Power Sources. 247: p. 503-516.
[85] Ali, M., Lai, W., Pan, J. (2015). "Computational models for simulation of a lithium-ion battery module specimen under punch indentation." Journal of Power Sources **273**: 448-459.
[86] Greve, L. and C. Fehrenbach (2012). Mechanical testing and macro-mechanical finite element simulation of the deformation, fracture, and short circuit initiation of cylindrical Lithium ion battery cells. Journal of Power Sources. 214: p. 377-385.
[87] Avdeev, I. and M. Gilaki (2014). Structural analysis and experimental characterization of cylindrical lithium-ion battery cells subject to lateral impact. Journal of Power Sources. 271: p. 382-391.
[88] Ali, M., W. Lai, and J. Pan (2013). Computational models for simulations of lithium-ion battery cells under constrained compression tests. Journal of Power Sources. 242: p. 325-340.
[89] Tvergaard, V. (1981). "Influence of voids on shear band instabilities under plane strain conditions." International Journal of Fracture **17**(4): 389-407.
[90] Zhang, C., Santhanagopalan, S., Sprague, M. A., and Pesaran, A. (2015). Coupled mechanical-electrical-thermal modeling for short-circuit prediction in a lithium-ion cell under mechanical abuse. Journal of Power Sources. 219: p. 102-113.
[91] Gurson, A. L (1977) Continuum Theory of Ductile Rupture by Void Nucleation and GrowthPart I—Yield Criteria and Flow Rules for Porous Ductile Media. J. Eng. Mater. Technol. 99(1), 2-15.

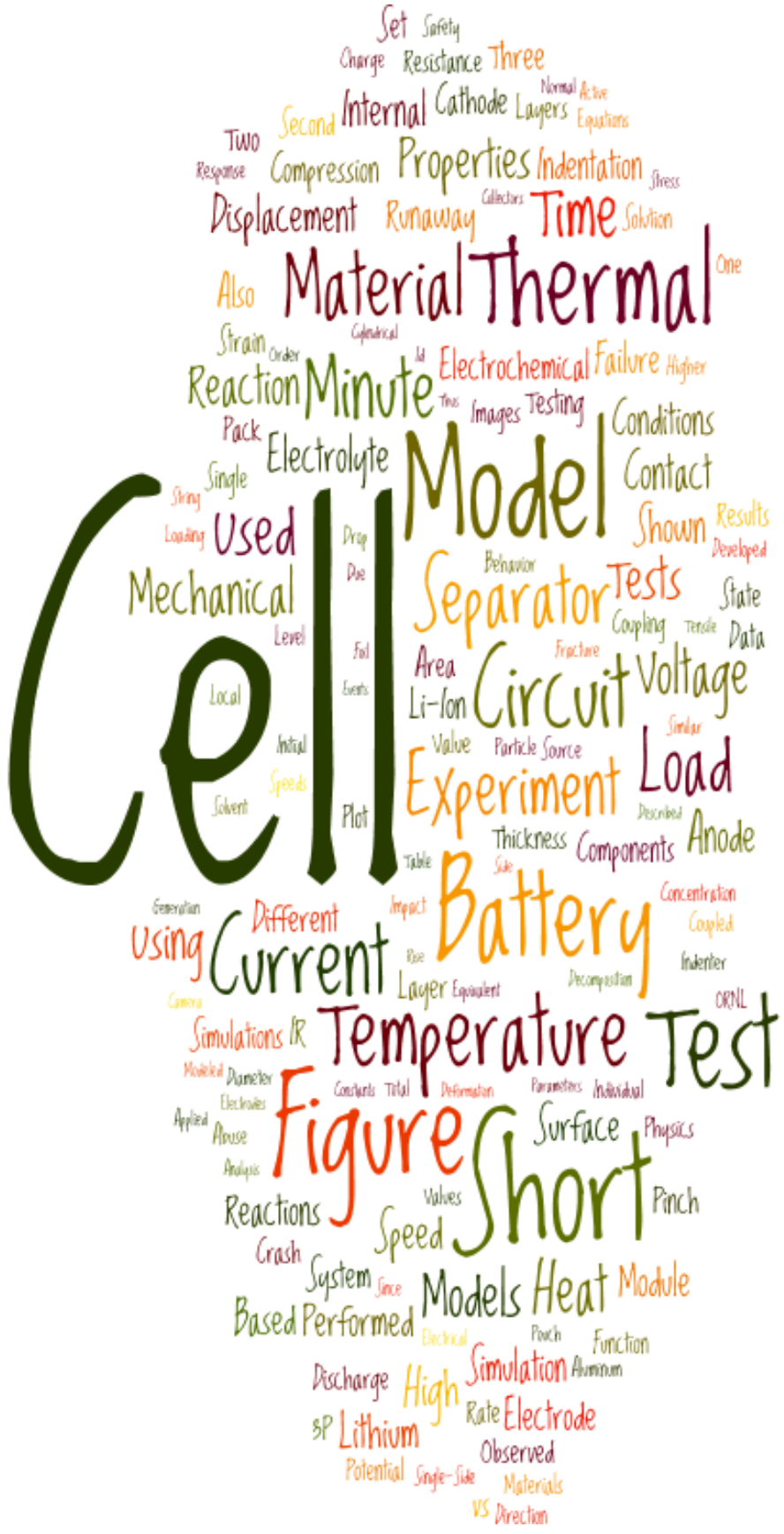
Set
Safety
Charge
Resistance
Three
Internal
Cathode
Layers
Normal
Active
Equations
Second
Two
Response
Compression
Properties
Indentation
Stress
Displacement
Runaway
Collectors
Time
Solution
Also
Material
Thermal
One
Cylindrical
Strain
Order
Reaction
Minute
Id
Electrochemical
Failure
Higher
Thus
Images
Testing
Conditions
Pack
Electrolyte
Model
Contact
Single
String
Loading
Used
Drop
Due
Shown
Results
Developed
Behavior
Mechanical
Separator
Tests
State
Level
Coupling
Tensile
Data
Cell
Fracture
Area
Fail
Events
Li-Ion
Circuit
Voltage
Local
Similar
Initial
Value
Particle
Source
Experiment
Load
Speeds
Solvent
Plot
Described
Thickness
Components
Anode
Table
Side
Concentration
Generation
Different
Impact
Battery
Coupled
Using
Current
Rise
Indenter
Layer
Equivalent
Decomposition
Camera
ORNL
Simulations
IR
Temperature
Test
Modeled
Diameter
Constants
Total
Deformation
Parameters
Individual
Electrodes
Figure
Surface
Physics
Applied
Abuse
Analysis
Short
Reactions
Values
Pinch
Speed
Crash
System
Since
Models
Heat
Module
Based
Performed
Electrical
Pouch
Function
Discharge
High
Simulation
Aluminum
SP
Lithium
Rate
Electrode
Observed
Potential
Single-Side
Materials
VS
Direction